ABSTRACT

In situ analysis of the high temperature deformation and fracture mechanisms of a γ-TiAl alloy

Gamma titanium aluminides are intermetallic alloys with great potential for aerospace applications in low pressure turbines (LPT) because they can provide increased thrust-to-weight ratios and improved efficiency under aggressive environments at temperatures up to 750 °C. Due to that, γ-TiAl alloys are projected to replace the heavier Ni-base superalloys currently used for LPT blades manufacturing.

The objective of this research work is to study the deformation and fracture mechanisms of a γ-TiAl alloy, Ti-45Al-2Nb-2Mn(at.%)+0.8(vol.%)TiB_2 (Ti4522XD), at service temperatures, and to relate them to specific microstructural features. An array of microstructures was first generated by processing the investigated alloy by centrifugal casting (CC) and by powder metallurgy (PM) techniques. *In situ* mechanical tests were then carried out in selected samples in a scanning electron microscope (SEM) aided by electron backscatter diffraction (EBSD) at 700 °C. In particular, constant strain rate (10^{-3} s^{-1}) and constant stress (creep) (250-450 MPa) tensile tests were performed and the microstructural evolution of selected areas was periodically imaged by SEM. The main findings of this research are summarized below.

First, in lamellar CC microstructures deformed under creep conditions colony boundary cracking was observed to be the main fracture mechanism. It occurred at low and high stresses, during the secondary and the tertiary creep stages, respectively. The same phenomenon has been observed to predominate along the γ grain boundaries in finer duplex PM microstructures under creep conditions. The occurrence of grain/colony boundary cracking reveals the activation of grain/colony boundary sliding (G/CBS) during creep deformation of lamellar and duplex microstructures, which leads to the nucleation of cracks at triple points. Moreover, in lamellar microstructures creep tested at high stresses (σ>400 MPa) and tensile tested at constant strain rate, the appearance of interlamellar ledges was observed, revealing that interlamellar areas become weaker as the stress increases.

Furthermore, the results obtained suggest that, in lamellar microstructures tested at high temperature and constant strain rate, true twin lamella boundaries constitute the weakest obstacles to dislocation motion. Thus, the relevant length scale might be influenced by the distance between non-true twin boundaries. Crystallographic slip is also observed to contribute to deformation under creep conditions. The slip activity during creep deformation was evaluated by trace analysis and a methodology to estimate the relative activity of ordinary and superdislocations, as well as the corresponding critical resolved shear stresses (CRSS), is proposed. This work showed the presence in both lamellar and duplex microstructures of a significant dislocation activity that does not comply with the Schmid law with respect to the applied stress and which thus seems to be a response to local stresses. Intragranular slip is suggested to be an active accommodation mechanism for GBS during creep of duplex microstructures.

2014

R. Muñoz Moreno

In situ analysis of the high temperature deformation and fracture mechanisms of a γ-TiAl alloy

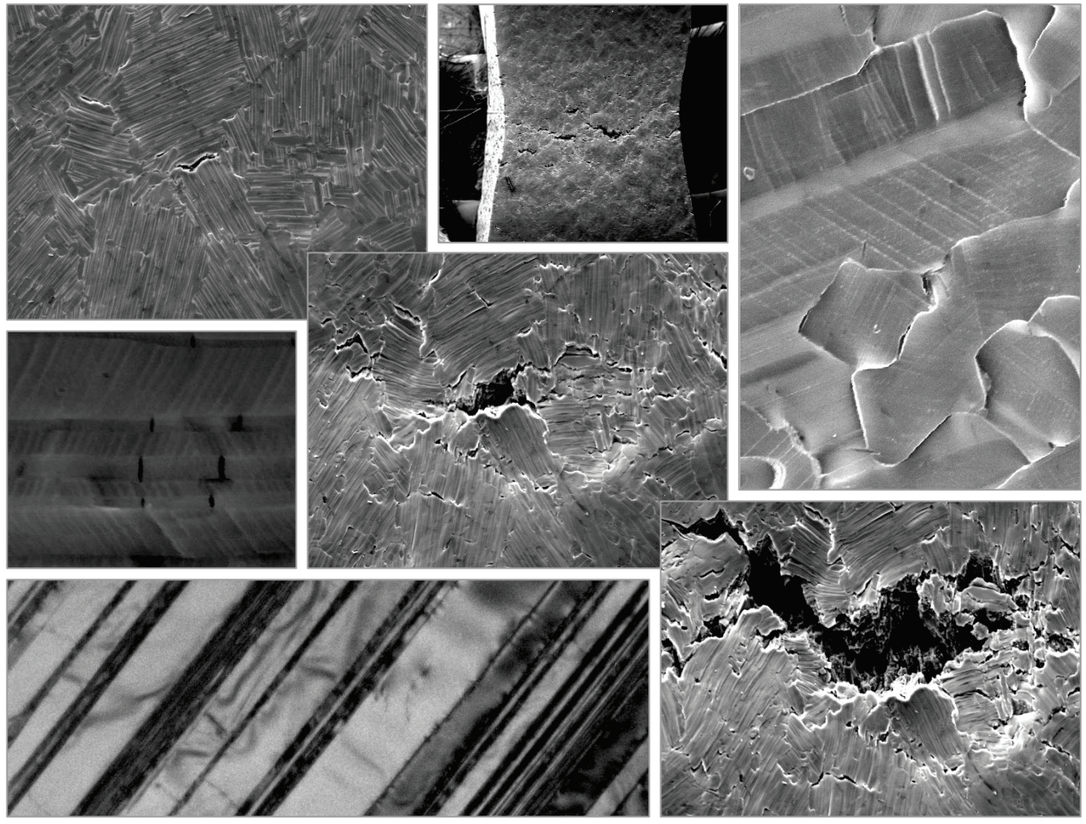

In situ analysis of the high temperature deformation and fracture mechanisms of a γ-TiAl alloy

Rocío Muñoz Moreno

May 2014

Universidad Carlos III de Madrid

institute IMdea materials

Universidad
Carlos III de Madrid

Ph.D Thesis

In situ analysis of the high temperature deformation and fracture mechanisms of a γ-TiAl alloy

Author:

Rocío Muñoz Moreno

Supervisors:

Dra. M. Teresa Pérez Prado

Dra. Elisa M. Ruiz Navas

Department of Materials Science and Engineering and Chemical Engineering

Leganés, May 5th 2014

TESIS DOCTORAL

IN SITU ANALYSIS OF THE HIGH TEMPERATURE DEFORMATION AND FRACTURE MECHANISMS OF A γ-TiAl ALLOY

Autora: Rocío Muñoz Moreno

Directoras: Dra. M. Teresa Pérez Prado
Dra. Elisa M. Ruiz Navas

Firma del Tribunal Calificador:

Firma

Presidente: Prof. Sophia Alexandra Tsipas

Vocal: Dr. Koldo Mirena Ostolaza Zamora

Secretario: Dr. Claudio Zambaldi

Calificación:

Leganés, 5 de Mayo de 2014

A Carlos,

a mis padres y a Ale.

Acknowledgements

Terminando ya los últimos apuntes, miro hacia atrás y me inunda una enorme sonrisa, ¡qué gran etapa! Sin duda han sido unos años maravillosos, llenos de aprendizaje científico y técnico, que me han ayudado a crecer como aprendiz de una profesión altamente enriquecedora y satisfactoria. A todo ello han contribuido muchísimas personas, a las que ahora deseo agradecer su compañía y amistad. Son mi gran tesoro.

En primer lugar, me gustaría agradecer especialmente a mis directoras de tesis, la Dra. M. Teresa Pérez Prado y la Dra. Elisa M. Ruiz Navas, su dedicación y su apoyo incondicional. Les agradezco sus enseñanzas en el campo de la Ciencia e Ingeniería de Materiales y su modo de transmitirme la metodología científica. Su ejemplo ha sido mi motor durante estos años. Gracias por las discusiones científicas, por vuestros acertados consejos y por una excelente orientación en el desarrollo de esta tesis. Habéis sido mis mejores maestras y unas mentoras inigualables. Ha sido maravilloso compartir con vosotras estos años tan especiales.

Agradezco enormemente al Instituto IMDEA Materiales y al Grupo de Tecnología de Polvos de la Universidad Carlos III de Madrid (UC3M). Gracias al Prof. Javier Llorca y al Prof. José Manuel Torralba por confiar en mí y abrirme las puertas de una magnífica institución y de un excelente grupo de investigación. Gracias por el gran apoyo que ofrecen a la investigación puntera en Ciencia e Ingeniería de Materiales. Gracias Javier y José Manuel, por tener vuestras puertas siempre abiertas para ayudarme.

Muy especialmente quiero agradecer al Prof. Carl Boehlert por sus enseñanzas en la técnica de ensayos mecánicos *in situ*, así como su colaboración en el análisis de los resultados de esta tesis. Gracias Carl, por tú cálida acogida en EE.UU. y tus sabios consejos.

Gracias a la empresa ITP (Industria de Turbopropulsores S.A.) por el suministro de los álabes y por su inmediata disposición a contestar nuestras dudas. Vuestro interés por hacer de nuestro trabajo una aplicación real ha sido una gran motivación.

Agradezco también al Departamento de Ciencia e Ingeniería de Materiales e Ingeniería Química de la UC3M y al de la Michigan State University por todas las facilidades para llevar a cabo mis investigaciones.

Gracias al gran número de investigadores que me han ayudado en el análisis y en la discusión de los resultados de esta tesis. Gracias a todos ellos que amablemente me ayudaron y me sugirieron ideas durante coloquios, reuniones o ponencias. Mi más sincero agradecimiento al Dr. J. Molina, al Dr. S. Milenkovic, Dr. I. Sabirov, a la Prof. E. Gordo, a la Prof. M. Campos, a la Prof. S. Tsipas, al Prof. M. Crimp, al Prof. T. Bieler, al Dr. C. Zambaldi, al Prof. B. Srinivasarao, a la Dra. C. Cepeda, a la Dra. P. Hidalgo, al Dr. L. Bolzoni, a Ajith Chakkedath, a Ana Fernández, a Saeid Loftian y a Alberto Palomares. También querría agradecer a todas las personas que me han ayudado en la lucha experimental, en especial a Juan Carlos Rubalcaba, a Vanesa Fernández y al Dr. P. Askeland. Gracias a los compañeros de otros centros que me ayudaron a llevar a cabo medidas para mis investigaciones, entre ellos al Centro Nacional de Investigaciones Metalúrgicas, al Instituto de Nanociencia de Aragón, al CAI de difracción de rayos X de la Universidad Complutense de Madrid (UCM) y al Centro Nacional de Microscopia. Gracias a mis compañeros de la Facultad de Ciencias Físicas de la UCM Madrid, siempre atentos para ayudarme. A todos ellos, y a los que por falta de espacio no puedo nombrar, ¡muchas gracias!

Y un gran, ¡gracias! a cada uno de los que me acompañáis día a día. Gracias a los compañeros del Grupo de Tecnología de Polvos y del Instituto IMDEA Materiales. Cada uno de vuestros cálidos consejos, charlas y ánimos me han ayudado enormemente. Muchas gracias por hacerme sentir en el trabajo, como en casa.

A mis amigos. Gracias a los que aparecieron en esta nueva etapa, a mis talismanes desde que llegué a Madrid y a los de siempre, por ayudarme a ver con claridad el horizonte sobre el mar.

Muchísimas gracias a mi familia, por apoyarme siempre en este proyecto. Gracias a Rosa y Andrés, por vuestro cariño y vuestra fuerza. Gracias a mis padres y a mi hermano por su motivación y sus inmejorables consejos. Muchas gracias por quererme tanto. ¡Gracias Ale, por tu fuerza investigadora! Y muy especialmente, quisiera agradecer a Carlos por su paciencia, comprensión, motivación y amor que me transmite minuto a minuto. Gracias Carlos por hacerme tan feliz.

Table of contents

Abstract

Gamma titanium aluminides are intermetallic alloys with great potential for aerospace applications in low pressure turbines (LPT) because they can provide increased thrust-to-weight ratios and improved efficiency under aggressive environments at temperatures up to 750 °C. Due to that, γ-TiAl alloys are projected to replace the heavier Ni-base superalloys currently used for LPT blades manufacturing.

The objective of this research work is to study the deformation and fracture mechanisms of a γ-TiAl alloy, Ti-45Al-2Nb-2Mn(at.%)+0.8(vol.%)TiB_2 (Ti4522XD), at service temperatures, and to relate them to specific microstructural features.

An array of microstructures was first generated by processing the investigated alloy by centrifugal casting (CC), in the form of LPT blades and rectangular specimens, and by powder metallurgy (PM) techniques, including hot isostatic pressing (HIP) and field assisted hot pressing (FAHP). Several post-processing heat treatments were carried out in both CC and PM samples. A thorough characterization of the microstructures thus generated was performed by scanning and transmission electron microscopy. *In situ* mechanical tests were then carried out in selected samples according to specific microstructures in a scanning electron microscope (SEM) aided by electron backscatter diffraction (EBSD) at 700 °C. In particular, constant strain rate ($\dot{\varepsilon}$=10^{-3} s^{-1}) and constant stress (creep) (σ=250-450 MPa) tensile tests were performed and the microstructural evolution of selected areas was periodically imaged by SEM. The main findings of this research are summarized below.

First, in lamellar centrifugally cast microstructures deformed under creep conditions colony boundary cracking was observed to be the main fracture mechanism. It occurred at low and high stresses, during the secondary and the tertiary creep stages, respectively. The same phenomenon has been observed to predominate along the γ grain boundaries in finer duplex powder metallurgy microstructures under creep

conditions. The occurrence of grain/colony boundary cracking reveals the activation of grain/colony boundary sliding (G/CBS) during creep deformation of lamellar and duplex microstructures, which leads to the nucleation of cracks at triple points. Moreover, in lamellar microstructures creep tested at high stresses (σ>400 MPa) and tensile tested at constant strain rate, the appearance of interlamellar ledges was observed, revealing that interlamellar areas become weaker as the stress increases.

Furthermore, the results obtained suggest that, in lamellar microstructures tested at high temperature and constant strain rate, true twin lamella boundaries constitute the weakest obstacles to dislocation motion. Thus, the relevant length scale might be influenced by the distance between non-true twin boundaries. Crystallographic slip is also observed to contribute to deformation under creep conditions. The slip activity during creep deformation was evaluated by trace analysis and a methodology to estimate the relative activity of ordinary and superdislocations, as well as the corresponding critical resolved shear stresses (CRSS), is proposed. This work showed the presence in both lamellar and duplex microstructures of a significant dislocation activity that does not comply with the Schmid law with respect to the applied stress and which thus seems to be a response to local stresses. Intragranular slip is suggested to be an active accommodation mechanism for GBS during creep of duplex microstructures.

Resumen

Los aluminuros de titanio gamma son intermetálicos de gran potencial para aplicaciones aeronáuticas en turbinas de baja presión al proporcionar una elevada resistencia específica en condiciones de servicio agresivas, con temperaturas próximas a los 750 °C. Debido a ello, se espera que las aleaciones γ-TiAl reemplacen a las superaleaciones de base níquel, de mayor peso, que componen actualmente los álabes de estas turbinas.

El objetivo de este trabajo de investigación es estudiar los mecanismos de deformación y fractura de una aleación γ-TiAl, la Ti-45Al-2Nb-2Mn(at.%)+0.8(vol.%)TiB_2 (Ti4522XD), en condiciones equivalentes a las de servicio, y establecer relaciones con características microestructurales específicas.

Se generaron distintas microestructuras mediante colada centrifuga y mediante técnicas pulvimetalúrgicas tales como compactación isostática en caliente y compactación asistida por campo. Posteriormente se llevaron a cabo tratamientos térmicos de las muestras así procesadas. Estas microestructuras se caracterizaron de forma exhaustiva mediante microscopia electrónica de barrido y de transmisión. Se realizaron ensayos mecánicos *in situ* en el interior de un microscopio electrónico de barrido, provisto de un detector de electrones retrodispersados, en muestras seleccionadas según su microestructura. En concreto, se realizaron ensayos a 700 °C a velocidad de deformación constante ($\dot{\varepsilon}=10^{-3}$ s^{-1}) y a tensión constante (σ=250-450 MPa) (fluencia), y durante los mismos se tomaron periódicamente imágenes de la evolución de la microestructura en áreas seleccionadas de las muestras. Las principales aportaciones de esta investigación se resumen a continuación.

En primer lugar, se ha observado que en microestructuras laminares procesadas mediante colada centrifuga y ensayadas a fluencia el mecanismo principal de fractura es la nucleación de grietas en las fronteras de las colonias. Este fenómeno se observó en

los ensayos de fluencia llevados a cabo tanto a bajas como a altas cargas, durante los regímenes secundario y terciario, respectivamente. En microestructuras dúplex obtenidas mediante ruta pulvimetalúrgica y ensayadas a fluencia se observó una intensificación de la nucleación de grietas a lo largo de las fronteras de los granos γ. Esto es consistente con la activación del mecanismo de deslizamiento de fronteras de grano/colonia que da lugar a la concentración de tensiones en los puntos triples. Además, las microestructuras laminares ensayadas a fluencia con cargas más elevadas (σ>400 MPa) y las deformadas a velocidad de deformación constante mostraron relieves interlaminares. Esto sugiere que las regiones entre láminas se debilitan al aumentar la tensión.

Finalmente, los resultados obtenidos sugieren que, en microestructuras laminares ensayadas a alta temperatura y velocidad de deformación constante, las intercaras γ/γ de tipo *true twin* constituyen obstáculos débiles para el avance de las dislocaciones. Por ello, la longitud crítica más relevante de estos materiales debe estar influenciada por la distancia entre fronteras distintas a las *true twin*. También se ha observado la contribución del deslizamiento cristalográfico a la deformación en condiciones de fluencia. Se ha estudiado por ello el deslizamiento de dislocaciones mediante un análisis de trazas y se ha propuesto una metodología para estimar la actividad relativa de dislocaciones ordinarias y superdislocaciones, así como su correspondiente tensión crítica de cizalla resuelta. Se ha observado que en microestructuras dúplex y laminares un número relativamente elevado de trazas de deslizamiento corresponden a sistemas que no obedecen la ley de Schmid con respecto a la carga aplicada y que, por tanto, deben ser activados por tensiones locales. Finalmente se propone que el deslizamiento intragranular de dislocaciones contribuye a la acomodación del deslizamiento de fronteras de grano de microestructuras dúplex ensayadas en fluencia.

Preface

The PhD thesis here presented has been carried out at the Department of Materials Science and Engineering and Chemical Engineering of the Carlos III University of Madrid and at the Madrid Institute for Advanced Studies in Materials (IMDEA Materials Institute). In addition, this research work has been developed in close collaboration with the company ITP (Industria de Turbopropulsores S. A.), a subsidiary of Rolls-Royce, which has interest in using gamma titanium aluminides to build the next generation of low pressure turbine blades.

This work have been developed in the frame of a project awarded by the Spanish Ministry of Science and Innovation ("Development of advanced Gamma TiAl alloys for components with high reliability: Microstructure, design and modeling of the mechanical behavior", ALTIVA MAT2009-14547-C02-01 and MAT2009-14547-C02-02).

This doctoral thesis has been recognized with the mention of *International PhD*. Part of the *in situ* mechanical testing research work has been carried out at the Michigan State University (USA) during 4 months in order to utilize the best available equipment and to get in touch with the world´s experts in the area. Moreover, 2 international experts in high temperature structural materials, Dr. Jonathan D. H. Paul (Zentrum für Material- und Küstenforschung GmbH, Helmholtz-Zentrum Geesthacht) and Prof. M. Cecila Poletti (Institute for Materials Science and Welding, TU Gratz), have reviewed the present manuscript.

The results obtained during the course of this thesis have been published in top international journals in the field of Metallurgy, such as Metallurgical and Materials Transactions A and Materials Science and Engineering A, and are currently submitted to Journal of Materials Science and Technology. Moreover, this work has been well received at international conferences and workshops on the field of intermetallics.

1 Introduction

1. Introduction

1.1 Gamma titanium aluminides

Gamma titanium aluminides are structural intermetallics with a singular combination of low densities (3.9-4.2 g/cm^3) and excellent mechanical properties at high temperature [1-3]. Therefore, they are being targeted by aerospace industries aiming to build lighter and stronger engine components such as, for example, low pressure turbine (LPT) blades [4, 5]. An example illustrating these higher specific properties of γ-TiAl alloys in comparison with other metals is shown in Figure 1.1, which explains how such alloys have the potential to replace the heavier Ni-base superalloys currently used. Extensive research efforts during the past two decades [6-13] have resulted in the development of a wide variety of γ-TiAl alloys with balanced properties as room temperature elongation-to-failure, fracture toughness, high-temperature strength, creep resistance and oxidation behavior. Moreover, some of these alloys have already found commercial uses [14, 15]. In the following, the state of the art on the physical metallurgy of these materials is reviewed.

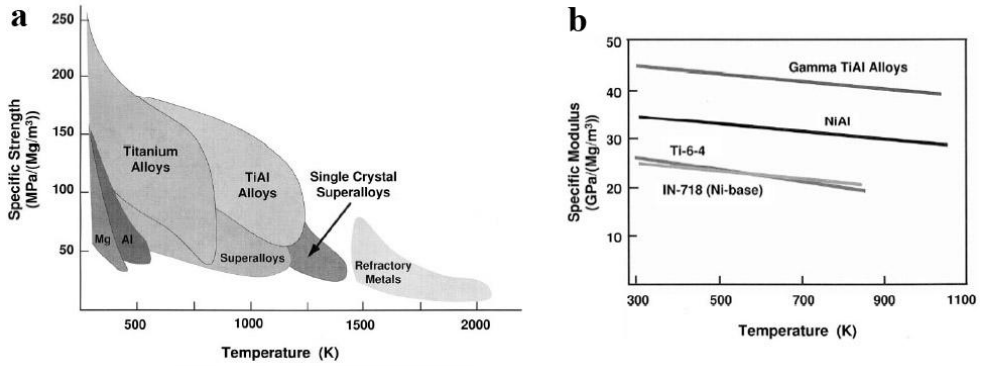

Fig. 1.1 High temperature (a) specific strength and (b) specific modulus of different structural metals and intermetallics [3].

1.1.1 Phase transformations

The Ti-Al binary phase diagram was first published in the 1950s [16, 17] and this work has been a reference for posterior research [18-22]. The γ-TiAl phase diagram is still under research due to its high complexity. The current state of the art on this issue has been summarized by Schuster *et al*. [20] and Hecht *et al*. [21]. In the proposed phase diagrams (Figure 1.2) the two main intermetallic phases (γ-TiAl and α_2-Ti_3Al) are stable at room temperature in thermodynamic equilibrium for intermediate Al concentrations (35-49%). The γ-TiAl phase has a face centered tetragonal (fct) $L1_0$ structure and the α_2-Ti_3Al phase has a hexagonal close packed (hcp) DO_{19} structure (Figure 1.3). Their corresponding lattice parameters are: γ-TiAl: a=0.4005 nm, c=0.4070 nm; α_2-Ti_3Al: a=0.5782 nm, c=0.4629 nm. The volume fraction of these two phases is controlled by the concentrations of Al. In general, γ-TiAl based alloys are composed by a 0.80-0.95 volume fraction of the γ phase, with the remainder being α_2 phase [6, 7]. Considering possible alloying in order to improve the binary alloy properties, ternary phase diagrams have also been deeply studied under an extensive thermodynamic analysis [23-25].

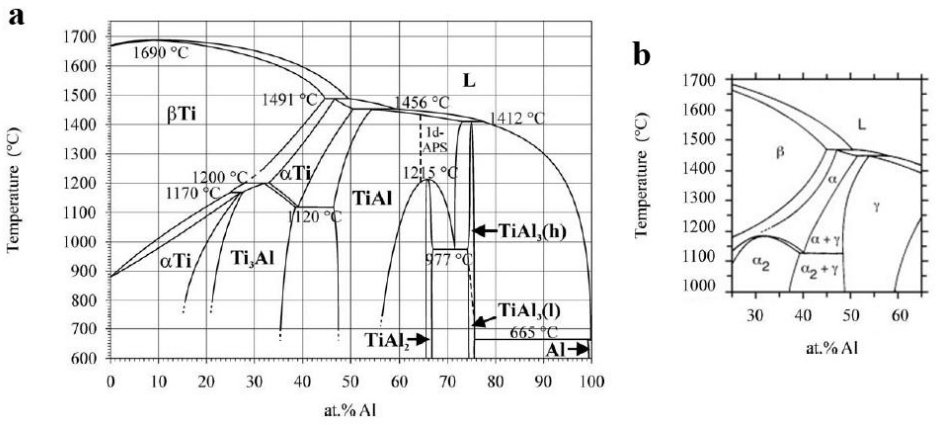

Fig. 1.2 (a) Complete binary Ti-Al phase diagram [20] and (b) section of the full diagram corresponding to intermediate Al concentrations [22].

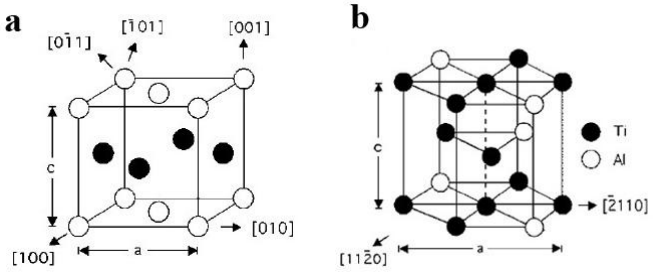

Fig. 1.3 Crystal structures of (a) γ-TiAl ($L1_0$) and (b) α_2-Ti_3Al (DO_{19})[7].

Extensive research on the TiAl binary phase diagrams has led to the proposition of several phase transformation sequences as a function of the Al content. The microstructure formation during solidification is, thus, also strongly dependent on the Al concentration [7, 20]. In alloys with Al concentrations below 45 at.%, the solidification path goes through the β phase (body centered cube structure, bcc, A2 structure and its ordered B2 variant) ($L \rightarrow L + \beta \rightarrow \beta \rightarrow \alpha \cdots$). β-solidifying alloys exhibit a refined and homogeneous microstructure without microsegregations, which indicates backdiffusion in the β phase and solidification relatively close to the equilibrium. In alloys with Al concentrations between 45 and 49 at.%, the solidification path goes through the α phase ($L \rightarrow L + \beta \rightarrow \alpha + (\beta) \rightarrow \cdots$). Inhomogeneities and segregation can be derived from the peritectic reaction by which β dendrites transform into the α phase. An increase of the Al content until 55 at.% results in an increasingly lower driving force for the formation of α and β in favor of the formation of the γ phase.

Following solidification and upon further cooling, γ-TiAl intermetallics with intermediate Al concentrations (38-50 at.%) pass through the α solid solution region. Denquin and Naka [26] proposed three main solid-state transformation mechanisms: lamellar transformation, discontinuous coarsening and massive-type transformation. Particularly, they explained that lamellar transformations mechanism consisted on the $\alpha \rightarrow \alpha_2$ ordering reaction combined with a massive transformation, which is based on the precipitation of γ lamellae in the α or α_2 matrix via the following sequence: $\alpha \rightarrow \alpha + \gamma \rightarrow \alpha_2 + \gamma$. They also explained that these reactions occur through a pre-nucleation stage, which changes the ABAB hcp stacking sequence to the ABC or ACB fct stacking sequences. Then, a nucleation stage occurs by promoting ordering reactions and lamellae grow. In this last stage, γ phase grow following defined orientation restrictions which limit their c-axis alignment with respect to the hcp structure [27, 28]. More recent studies by Zghal *et al*. [29] also confirm that γ phase orientation depends on the transformation temperature stage. Additional information about specific aspects of these transformations can be found in [30-34].

1.1.2 Microstructures

γ-TiAl alloys with Al concentrations between 35 and 49 at.% exhibit a wide range of two phase (γ-TiAl and α_2-Ti_3Al) microstructures, which are commonly classified as a function of the volume fraction of equiaxed grains and lamellar colonies (grains containing stacked, parallel lamellae) [7]. The most representative γ-TiAl microstructures are shown in Figure 1.4. They are termed, respectively, fully lamellar (FL, composed exclusively by lamellar colonies), nearly

lamellar (NL, containing a small fraction of equiaxed grains), duplex (D, comprising similar volume fractions of equiaxed grains and lamellar colonies) and near gamma (NG, composed solely by equiaxed grains). Other particular lamellar microstructures are the so called Widmanstätten colonies and feathery structures. The former are packets of parallel ($\alpha_2+\gamma$) lamellae inside existing lamellar colonies [35, 36]. The latter are groups of lamellae within a colony that are slightly misoriented (typically less than 15 °) with respect to the surrounding colony [37] and are not exactly parallel to one another.

The above described microstructures may be generated in a given γ-TiAl alloy by thermal treatments involving different temperatures and cooling rates [8, 12, 26, 27, 38, 39], as illustrated schematically in Figure 1.5. Heat treating at temperatures slightly above the eutectoid point results in the development of near gamma microstructures. Higher annealing temperatures favor the stabilization of α regions, and, in turn, lead to the formation of lamellar microstructures as $\alpha+\gamma$ lamellae grow from the α domains. Thus, duplex and nearly lamellar structures will result from annealing at increasingly high temperatures within the $\alpha+\gamma$ phase field. The development of fully lamellar microstructures requires treating at temperatures above the α-transus. Moreover, low cooling rates (≤10 °C/s) promote the formation of lamellar microstructures. The lamellar spacing and the colony size will depend on the specific rate. In contrast, higher cooling rates (>100 °C/s) promote the stabilization at room temperature of the α or the α_2 phases or the massive γ phase transformation, i.e., the formation of bulk gamma grains.

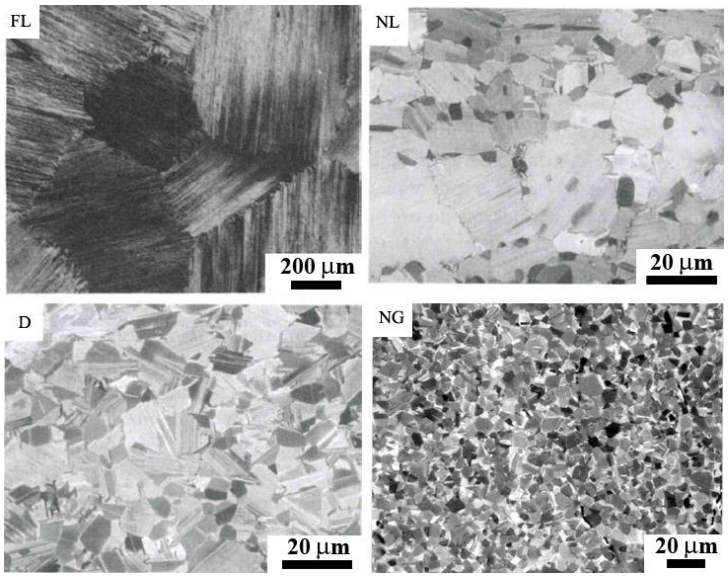

Fig. 1.4 γ-TiAl microstructures: Fully lamellar (FL), nearly lamellar (NL), duplex (D) and near gamma (NG) [8, 12].

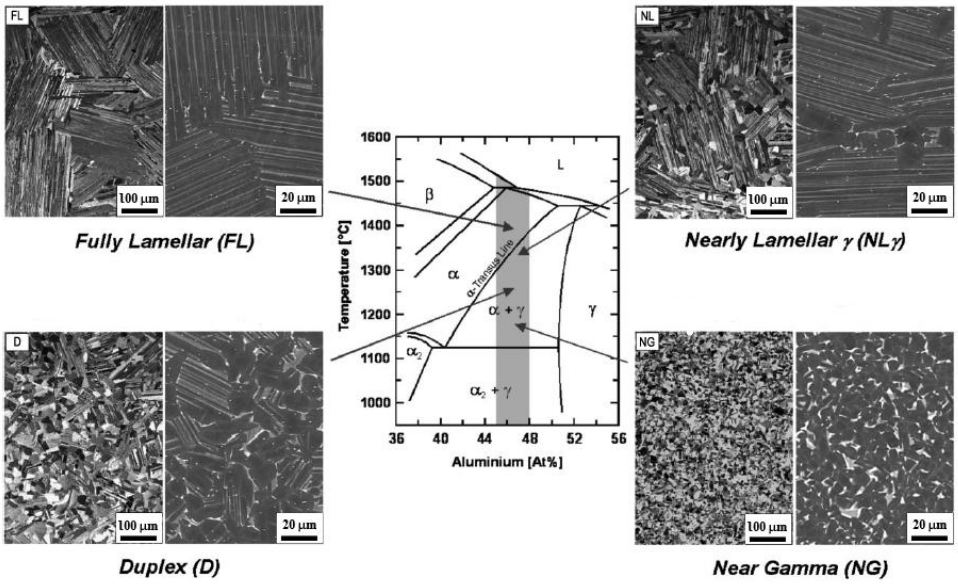

Fig. 1.5 Microstructure generation in γ-TiAl alloys by thermal treatments [6].

1.1.3 Lamellar domain structures

Each α grain gives rise, upon cooling, to an unique (α_2+γ) lamellar colony, where the α_2 basal planes are parallel to the former α basal plane. Lamellar interfaces may be of either the α_2/γ or the γ/γ type. The most densely packed planes of both phases are always parallel to the interphase boundaries. γ-TiAl and α_2-Ti_3Al phases are always oriented according the Blackburn relationship [40]:

$$(0001)_{\alpha_2} || \{111\}_{\gamma} \text{ and } \langle 11\bar{2}0\rangle_{\alpha_2} || \langle 1\bar{1}0|_{\gamma}$$

Because of the symmetry of the γ phase, there are six variants of this orientation relationship, which can formally be described by rotations of the two phases relative to each other by a multiple of 60 ° around $[0001]_{\alpha 2}$ and < 111 >$_{\gamma}$, respectively (Figure 1.6(a)). Considering the two different γ phase stacking sequences (ABC or ACB) [29], the six γ variants presented above could be divided into two groups of three. Each of the three γ variants corresponds to a different orientation of the $\langle 1\bar{1}0]$ direction in the habit plane. Therefore, there are three γ/γ interfaces. The latter receive different names according to the rotation angle around the <111>γ direction that would bring both neighboring variants into coincidence. As such, γ/γ interfaces are termed pseudotwins (PT, 60 °), order variants (OV,

120 °) and true twins (TT, 180 °). At PT γ interfaces the $\langle 1\bar{1}0]$ direction of one of the lamellae is perpendicular to the $\langle 10\bar{1}]$ direction of the neighboring lamellae. In this case, the atomic stacking of the parent fct lattice is reversed and the order is rotated. Then, PT interfaces exhibit a quasi mirror configuration of the atoms arrangement on $\{110\}$ planes. At the TT γ interfaces the $[1\bar{1}0]$ direction of one of the lamellae is antiparalell to the $[\bar{1}10]$ direction of the neighboring lamellae. At this interface only the stacking sequence of the parent L10 structure is changed. Therefore, they are characterized by a mirror arrangement across the interface. Finally, in OV γ interfaces the $[1\bar{1}0]$ direction of one lamellae is antiparalell to the $[\bar{1}10]$ direction of the adjacent lamellae. Moreover, these interfaces retain the ABC stacking of the fcc lattice, disregarding tetragonal configuration. The orientation relationships explained previously are schematically illustrated in Figure 1.6(b) [41, 42]. Within one lamellar colony, TT, OV and PT variant orientation relationships occur across γ/γ interfaces and define the lamellar variant structure, while OV domains exist in the interior of individual lamellae [43]. This characteristic lamellar domain structure can be recognized in the high resolution TEM micrograph and the schematic drawing illustrated in Figure 1.7.

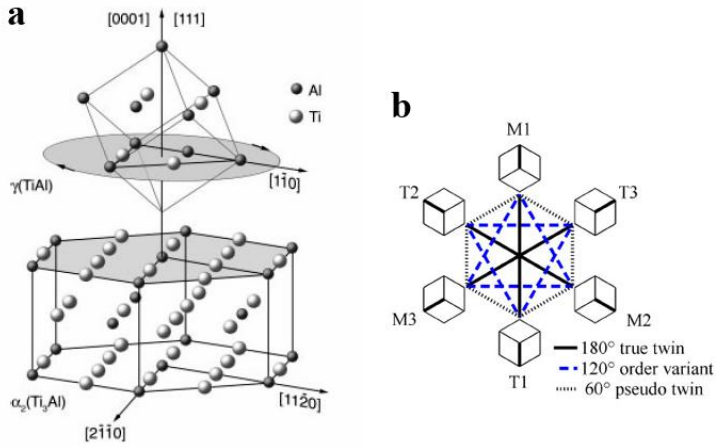

Fig. 1.6 (a) Orientation relationship between the α_2 and γ phases [7]; (b) schematic drawing of the possible orientation relationships between different γ/γ variants [41].

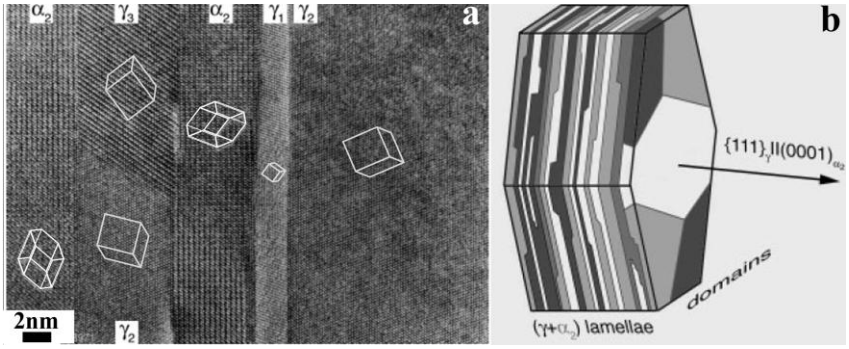

Fig 1.7 The γ-TiAl lamellar domain microstructure [7]: (a) High resolution TEM micrograph; (b) schematic drawing.

Previous research work has shown that the frequency of γ/γ TT interfaces is higher than those of PT and OV boundaries [44-46], as illustrated in Figure 1.8(a). Moreover, Figure 1.8(b) illustrates the calculations of the interface energies by atomistic modeling carried out by Mansour *et al*. [47], which attest to the low interface energy values of TT boundaries. This frequency distribution might be influenced by the thermal history of the material.

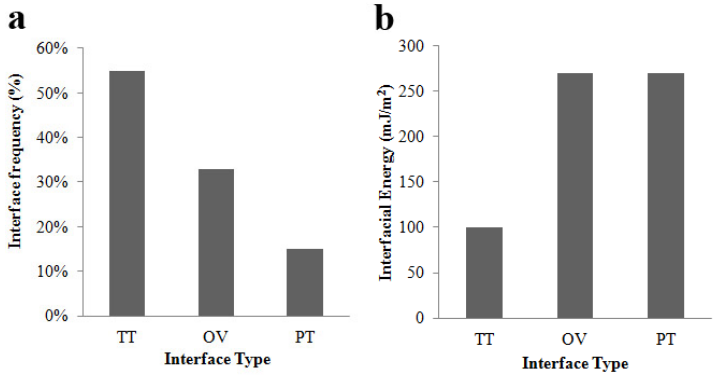

Fig. 1.8 (a) Frequency of TT, OV and PT γ/γ interfaces in a Ti-48Al-2Cr-2Nb polycrystalline alloy [45]; (b) interfacial energy values of TT, OV and PT γ/γ interfaces in a binary TiAl alloy [47].

1.1.4 Alloy design

The composition of γ-TiAl alloys has evolved since their identification as potential aerospace materials. Studies started from the analysis of binary alloys and their well balanced properties, and posterior research has focused on ternary and quaternary alloying as a key design tool [6, 7, 12].

First generation of γ-TiAl alloys

In the early 90s, the first generation of TiAl alloys was based on the Ti-48Al system, which exhibited the highest elongation to failure at room temperature among other binary Ti-Al alloys [48]. Alloying additions of 2% Nb and 2% Cr or 2% Mn were considered in order to increase high-temperature strength and creep resistance as well as elongation-to-failure at room temperature, respectively [7, 49, 50]. Nb additions benefited oxidation resistance by decreasing the final α_2 volume fraction, as the α_2 phase has higher O_2 solubility than the γ phase, and by promoting Al_2O_3 formation. In addition, Nb alloying displaces phase transformation temperatures and promotes the development of the softer β phase. On the other hand, Cr or Mn additions result in a reduction of the α transus temperature and lead to more ductile alloys. The origin of this effect is, however, still not clearly understood due to the large amount of parameters involved in the process. Therefore, at these earlier stages, the most important alloy was Ti–48Al–2Cr–2Nb. It was patented by Huang et al. [51] and commercialized by General Electric. It is the most investigated alloy to date.

Second generation of γ-TiAl alloys

During the late 90s an important effort was made in order to develop a second generation of γ-TiAl alloys with improved creep resistance and room temperature ductility. The base composition range investigated was: Ti-(45-48)Al-(1-3)X-(2-5)Y-(<1)Z where X=Cr, Mn, V; Y=Nb, Ta, W, Mo; Z=Si, B, C. Table 1.1 summarizes the effect of each element on the alloy properties [12]. The addition of β-stabilizer elements (Y) [52-55], such as Nb, that go into solid solution, was considered in order to further enhance high temperature capabilities. Additionally, incorporating not soluble elements (Z) [7], which lead to silicides, borides and carbides precipitation, helped in achieving a final microstructure refinement that improved elongation-to-failure values. The latter alloying strategy is commonly carried out by the XD™ process, which was devised at the Martin Marietta Laboratories [56-58] for the fabrication of discontinuously reinforced composites through an *in situ* method that allows controlling reinforcement shape, size and volume fraction. This method is commercialized by the Howmet

Corporation and has been used for the processing of Al and Cu-based metal matrix composites (MMC), titanium, nickel and iron aluminides as well as refractory metal aluminides. TiAl-XD™ alloys exhibit homogeneous microstructures with refined lamellar colonies due to the addition of TiB_2 particles as reinforcements [59]. Borides are present along the grain boundaries or inside the grains and exhibit particulate, needle or lacey shapes [60]. This type of reinforced alloys exhibit superior strength at high temperature and borides are particularly useful to assist fatigue behavior [61, 62]. The most studied 2nd generation alloy is the Ti–45Al–2Mn–2Nb–0.8vol.%TiB_2, which was deeply studied by the Rolls-Royce company for their specific applications.

Table 1.1 Effect of alloying elements on the mechanical properties of γ-TiAl alloys [12]

Element	Effect
Nb	Increases oxidation and creep resistance in small amounts (2%); increases high temperature strength if added between 5% and 10%
Ta	Increases oxidation and creep resistance and limits hot cracking
W	Improves oxidation and creep resistance
Cr	Increases ductility if added in small amounts (2%); increases oxidation resistance if added in the range of 8%
Mn	Increases ductility
V	Increases ductility
Mo	Increases strength and creep and oxidation resistance
B	Refines grain size
C	Increases creep and oxidation resistance

Third generation of γ-TiAl alloys

Finally, during the last decade, a 3rd generation of TiAl alloys has been developed with the aim of increasing high-temperature capabilities beyond the limits of the previously developed alloys. For that purpose, higher β-stabilizer concentrations were considered in order to promote β-solidifying mechanisms and then obtain more homogeneous and refined microstructures [6, 7, 63]. Moreover, β phase is soft and ductile at high temperatures, although an explanation for that effect is nowadays a matter of study. Therefore, TNB alloys were developed by adding high contents of Nb (5-10%) and small additions of B and C (<1%) and TNM™ alloy families were created by adding Nb and Mo in balanced proportions. These 3rd generation alloys benefit from enhanced creep resistance, although undesired recrystallization processes may lead to softening under certain processing conditions.

1.1.5 Processing of γ-TiAl alloys

γ-TiAl intermetallics have been conventionally processed by ingot metallurgy, casting and powder metallurgy (PM) [7, 12, 64-66], usually followed by post-processing steps in order to reach homogeneous microstructures and avoid remnant porosity. However, there is still an important challenge associated to γ-TiAl processing due to its inherent elevated costs and its machining limitations, derived from the material's low ductility at room temperature. Therefore, γ-TiAl alloys processing requirements are very complex and new advanced routes are currently being developed.

In particular, more processing routes at high temperature through near net shape techniques are being considered in order to reduce costs by avoiding material losses and final machining. Examples of these techniques are centrifugal casting, hot isostatic pressing (HIP) or field activated sintering, such as spark plasma sintering (SPS) [67-70].

Future advances on γ-TiAl processing point towards additive manufacturing techniques [71], which are based on a selective densification of metal powder by melting in a layerwise manner following a computer-aided design (CAD). These techniques include electron beam melting (EBM) or selective laser melting (SLM) [72-74]. Comparable microstructures and mechanical properties to those achieved by other techniques have been obtained, although improved porosity levels would be desirable.

1.1.5.1 Centrifugal casting

Centrifugal casting consists on the solidification of the molten metal in rotating moulds, where the rotation speed and the metal pouring rate vary with the alloy, size and shape being cast [75]. γ-TiAl alloys manufactured by centrifugal casting exhibit lower defect concentration than conventional ingot ones and their processing involves lower material loss. Computational analyses of mould filling and solidification during centrifugal casting have revealed that the small pores present are associated with existing temperature gradients [76, 77]. γ-TiAl LPT blades [78] and automotive valves [79, 80] are commonly processed by centrifugal casting via longer and complex routes such as that described by J. Aguilar *et al*.[78].

1.1.5.2 Powder metallurgy

In order to solve segregation issues as well as reproducibility difficulties, PM techniques are presented as a cheaper and more efficient alternative to conventional casting routes. A wide variety of PM consolidation routes have been considered, from conventional methods using elemental powders [59, 81-83], until the more recent innovative techniques [66, 70, 73, 84] in which prealloyed powders are used, resulting in improved microstructural homogenization and mechanical properties.

Prealloyed powders are usually obtained by gas atomization techniques, where the quality of the powder is measured by its contamination, particle size, particle size distribution and shape. Gas atomization techniques consist of breaking up a melt stream into metallic powder particles by applying a flow of inert gas. γ-TiAl prealloyed powders are usually atomized by crucible-free techniques or cold crucible techniques due to its reactive nature. Among them, plasma inert-gas atomization (PIGA), electrode induction gas atomization (EIGA) or titanium gas-atomizer process (TGA) are the most common [66]. In the PIGA process [85] a plasma torch is utilized in order to melt prealloyed material under a protective atmosphere (He or Ar) in a water-cooled copper crucible. In the EIGA process [86] the tip of the prealloyed rod is dipped into a conical induction coil and it is heated up (Figure 1.9(a)). Then, the melt drops into the center of a gas nozzle, where it is atomized by Ar gas. TGA is a similar processing technique to PIGA or EIGA, although in this case an induction skull melting unit is used to melt the prealloyed or elemental or master alloy ingot. In general, wide powder particles size distributions are obtained by the atomization techniques described above. Registering the cooling rates for different particles is experimentally very challenging. Gerling *et al*. [66] proposed the relationship between the cooling rate and the powder particle diameter that is illustrated in Figure 1.9(b). Powder particles with different sizes have usually widely varying microstructures according to the different cooling rates [87] (Figure 1.9(c, d)).

High energy milling (HEM) is usually utilized to break down TiAl powder particles, to achieve more homogeneous and refined final microstructures, as well as to facilitate mechanical alloying and lattice amorphizations [88-90]. Current laboratory research has largely advanced in this area and very recent publications show attractive results [91-93].

Since the prealloyed TiAl powder particles are rather hard, conventional pressing and sintering methods are usually substituted with more advanced hot compaction techniques, such as HIP [94-98] or SPS [68-70, 99-107]. The first PM processing trials in γ-TiAl included conventional hot consolidation techniques [81-83]. Hot consolidation techniques, consisting of the simultaneous pressing and sintering of the powders, have proven effective to enhance

compaction owing to the temperature activation of diffusion and straining mechanisms. Hot consolidation is commonly utilized for the manufacturing of conventional Ti alloys [108, 109] as it leads to a good microstructural homogenization and high density values. One of the most established hot consolidation techniques is HIP [67, 94-98]. HIP can be used directly to consolidate powders or to reduce the remnant porosity present in previously cold consolidated samples. HIPing at different temperatures followed by heat treatments constitutes an excellent tool for microstructural development in γ-TiAl alloys.

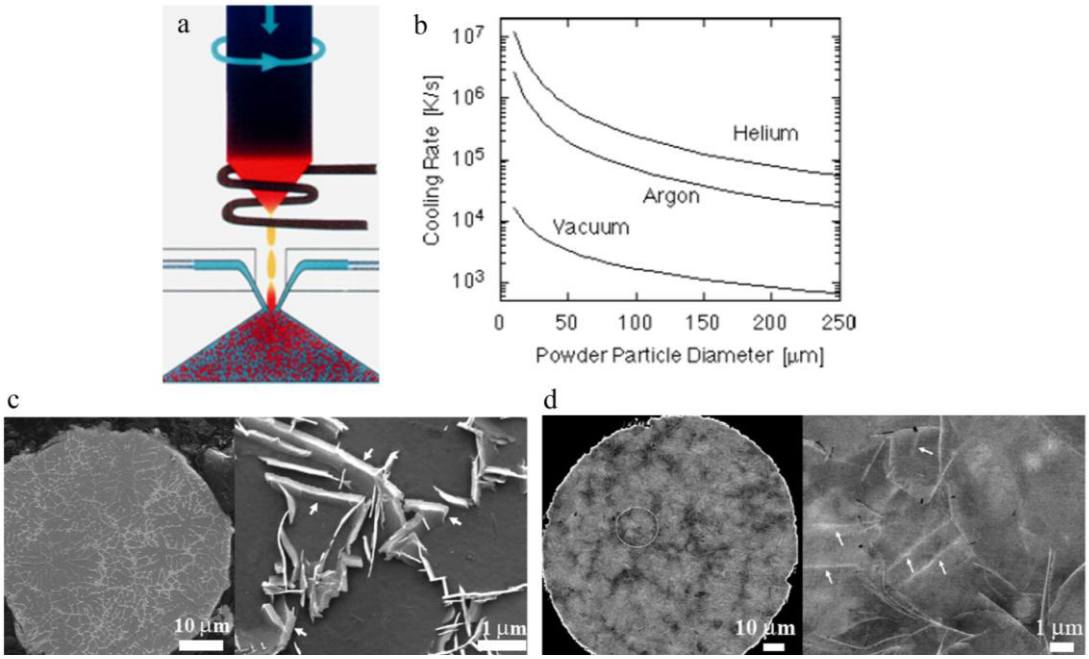

Fig. 1.9 (a) Schematic illustration of the EIGA technique; (b) relationship between the powder particle size and the cooling rate [66]; SEM micrograph of a polycrystalline Ti-45Al-2Nb-2Mn-1B powder showing microstructural differences in between (c) small (<100 μm) and (d) large (200 μm) powder particles [87].

Field activated sintering techniques use electric currents to improve consolidation under lower temperatures, pressures and holding times. These techniques facilitate rapid powder densification, thus resulting on minimal grain growth and limited pore formation [110]. The most popular field activated sintering technique for γ-TiAl processing is spark plasma sintering (SPS) [68-70, 99-107] which consists on passing high intensity current pulses through the powder under uniaxial pressure. A schematic drawing of the SPS process is shown in Figure 1.10(a). This processing route was first patented [111] in 1933 and subsequently applied by Munir *et al*. [110] for the processing of a wide variety of metallic materials. SPS has been recently utilized for the fabrication of advanced selected γ-TiAl alloys mainly by Couret *et al*. [69, 70, 101-107]. Important efforts are been devoted to improve the experimental

temperature control in order to better assess the large temperature gradients involved (Figure 1.10(b)). In fact, since large parts of intricated shapes such as turbine blades and other industrial components will undoubtedly suffer from large temperature gradients (Figure 1.11(a,b)), it is key to analyze the temperature distribution along the sample geometry in order to control the associated microstructural heterogeneities (Fig. Fig. 1.11(c)). Additional investigations have focused on the study of microstructural development and densification, on the analysis of the deformation mechanisms and on the effect of different alloying elements, such as B or Nb, in the resulting microstructures.

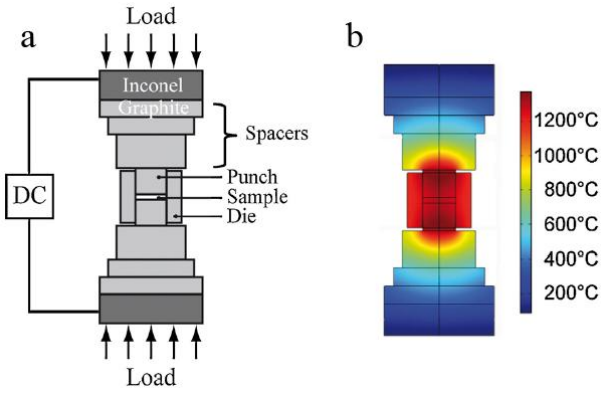

Fig. 1.10 (a) Schematic drawing of the SPS process; (b) temperature field distribution in the SPS system and in the processed material simulated by finite elements [69].

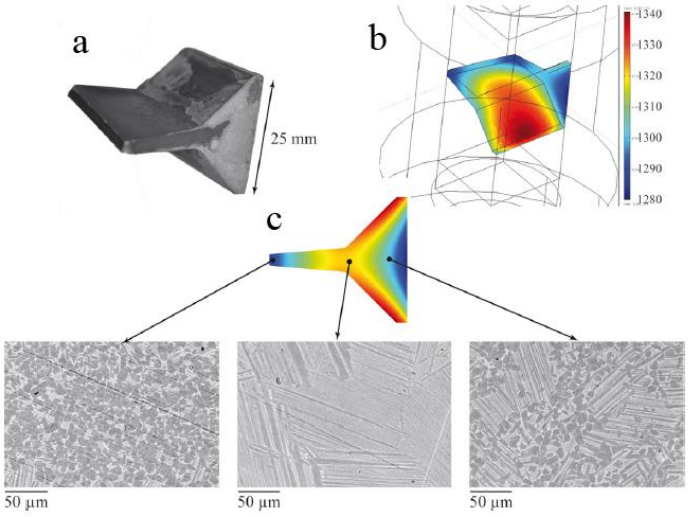

Fig. 1.11 Schematic drawing of (a) a component fabricated by SPS, (b) the temperature gradient and (c) the microstructures developed at different locations [70].

1.1.6 Mechanical behavior of γ-TiAl alloys

The mechanical behavior of γ-TiAl alloys is highly dependent on their microstructures. In general, fully lamellar microstructures are endowed with high strength as well as excellent creep resistance, whereas duplex structures are softer and usually possess higher room temperature elongation-to-failure. The properties are, furthermore, highly dependent of the volume fraction of both phases, as the α_2-phase is more brittle and γ-phase is softer, as well as of the complex multilayered configurations defined by γ/γ and α_2/γ interfaces in polysynthetically twinned (PST) crystals or in polycrystalline lamellar materials. Depending on the interface type distribution, as well as on the lamellae orientation with respect to the loading axis, different mechanical behavior might be expected.

Monocrystalline lamellar structures exhibit high plastic anisotropy as their yield stress and elongation-to-fracture strongly depend of the lamellar orientation with respect to the loading axis (ϕ) (Figure 1.12). Many authors have worked on this issue through the study of PST crystals [112-115]. When lamellae are parallel or perpendicular to the loading axis, higher yield stresses with lower elongation values are registered. In this hard mode, shear is mostly transverse to different lamellae and dislocation pile-ups occur at the lamellae interfaces. When ϕ is comprised between 30 ° and 60 °, higher elongations with lower yield stress values are registered. In this softer mode, shear occurs parallel to the lamellae interfaces and pile-ups form preferentially at the γ domain boundaries, dislocation slip paths are larger and higher ductilities are achieved. Figure 1.12 shows the stress-strain curves associated to the defined modes and illustrates the corresponding mechanisms. Polycrystals composed by soft and hard lamellar colonies, suffer from large strain incompatibilities derived from the different mechanical response of individual lamellar colonies. This is known as a pre-yielding phenomenon and seems to be an important reason to explain the lamellar low ductility against equiaxed grains microstructures behavior [116].

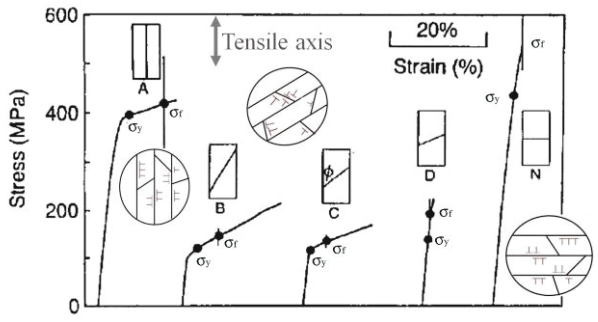

Fig. 1.12 Stress-strain curves illustrating the mechanical response of PST γ-TiAl lamellar structures as a function of the relative orientation of the loading axis with respect to the lamellae interface [114]. Yield (σ_γ) and fracture (σ_f) stresses were calculated for these curves by Hazzledine *et al*. [115].

1.1.6.1 Deformation mechanisms

Plastic strain accommodation of γ-TiAl based alloys at a wide range of temperatures and quasi-static strain rates has been reported to be mainly carried out by the softer γ phase through dislocation motion and mechanical twinning [7]. Activation of the latter has been found to be important to attain a sufficient number of deformation modes for strain compatibility [117]. Moreover, thermal activation promotes dislocation cross-slip and climb enhancing plastic deformation and reducing the plastic anisotropy.

Dislocation slip in fct γ-TiAl occurs preferentially on {111} planes along <110> directions in lamellar and equiaxed microstructures. Since the <110> slip directions are crystallographically not equivalent, two types of dislocations can be distinguished (Figure 1.13): ordinary dislocations (OD), with Burgers vector $\bar{b}_o = 1/2\langle 110]$ and superdislocations (SD), for which $\bar{b}_s = \langle 101]$ and $\bar{b}_s = 1/2\langle 11\bar{2}]$. Table 1.2 summarizes the twelve slip systems available as well as the type of dislocation corresponding to each one [41]. In lamellar structures dislocations may be further classified according to the orientation between their slip plane and direction and the corresponding lamella interface. As such, the so called dislocation morphology may be longitudinal (l), when both are parallel to the lamella boundary, mixed (m), when the plane makes an angle with the interface but the direction is parallel to it, and transverse (t), when both make an angle with the lamella boundary [118]. Table 1.2 summarizes the dislocation morphology associated to each slip system.

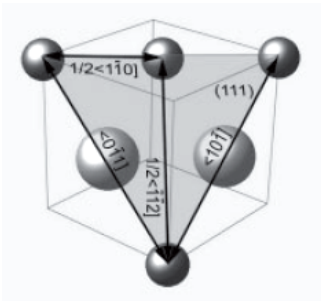

Fig. 1.13 Representation of γ-TiAl slip systems. The drawing shows a {111} plane and the orientation of the Burgers vectors corresponding to ordinary dislocations and superdislocations [7]

In terms of dislocation activity, slip of OD has been found to prevail always over SD slip in two phase γ-TiAl alloys [7], particularly at room temperature, where SDs are rarely observed and only constraint stresses can promote their glide. The activation of SDs is a complex function of temperature and alloy composition. An increase on the aluminum content [119] as

well as high levels of interstitial impurities in the γ-phase [120, 121] appear to promote SD movement. Further research is required in order to assess OD and SD activation and, thus, to improve the current understanding of the deformation mechanisms of γ-TiAl alloys.

Table 1.2 Classification of γ-TiAl slip systems depending on the dislocation type (OD: ordinary dislocation; SD: superdislocation) and the dislocation morphology [41, 118]

Slip Plane	Slip Direction	Dislocation Type	Dislocation Morphology
$\{\mathbf{111}\}$	$[1\bar{1}0]$	OD	Longitudinal
$\{\mathbf{111}\}$	$[10\bar{1}]$	SD	Longitudinal
$\{\mathbf{111}\}$	$[01\bar{1}]$	SD	Longitudinal
$\{\bar{\mathbf{1}}\mathbf{11}\}$	$[\bar{1}\bar{1}0]$	OD	Transversal
$\{\bar{\mathbf{1}}\mathbf{11}\}$	$[\bar{1}0\bar{1}]$	SD	Transversal
$\{\bar{\mathbf{1}}\mathbf{11}\}$	$[0\bar{1}1]$	SD	Mixed
$\{\mathbf{11}\bar{\mathbf{1}}\}$	$[1\bar{1}0]$	OD	Mixed
$\{\mathbf{11}\bar{\mathbf{1}}\}$	$[101]$	SD	Transversal
$\{\mathbf{11}\bar{\mathbf{1}}\}$	$[011]$	SD	Transversal
$\{\mathbf{1}\bar{\mathbf{1}}\mathbf{1}\}$	$[110]$	OD	Transversal
$\{\mathbf{1}\bar{\mathbf{1}}\mathbf{1}\}$	$[10\bar{1}]$	SD	Mixed
$\{\mathbf{1}\bar{\mathbf{1}}\mathbf{1}\}$	$[011]$	SD	Transversal

The Schmid law establishes that dislocation glide on a specific slip system is activated when the resolved shear stress on the slip plane along the slip direction (τ) at an applied stress (σ) is superior to the critical resolved shear stress (CRSS) for that specific slip system [122]. The resolved shear stress is calculated by:

$$\tau = \sigma \cos\phi \cos\psi \tag{1.1}$$

where ϕ is the angle between the applied stress and the slip plane normal and ψ is the angle between the applied stress and the slip direction. The product $\cos\phi\cos\psi$ is the so called Schmid factor (SF). Due to the complexity of the microstructures typical of γ-TiAl alloys, the CRSS values corresponding to the different slip systems have been little investigated and the few existing studies were carried out in single phase γ single crystals. The CRSS values have been found to depend mainly on the alloy composition, the temperature and the strain rate. The CRSS values corresponding to OD ($CRSS_O$) and SD ($CRSS_S$) in γ-TiAl single crystals were measured by Inui *et al*. [119] and other authors [123-126] and are summarized in Figure 1.14,

which shows the variations of these parameters with the Al content and with temperature in single crystal gamma alloys. In general, increasing the Al concentration results in an increase of the CRSS values. Additionally, both $CRSS_O$ and $CRSS_S$ present anomalous behavior with temperature, as both exhibit a peak at temperatures between 700 °C and 1000 °C. Knowing the CRSS values corresponding to the different deformation mechanisms of engineering alloys, as well as how alloying additions and operating service conditions (temperature, strain rate) affect those values is critical to the development of materials with improved properties. However, current methodologies to measure CRSS values are very time consuming, as they involve the fabrication of single crystals with different orientations in combination with numerical approaches, such as finite element modeling. Devising new, more efficient methodologies to evaluate CRSS values, especially in polycrystalline, multi-phase microstructures, is a timely issue that could certainly contribute to accelerate the design of advanced intermetallics.

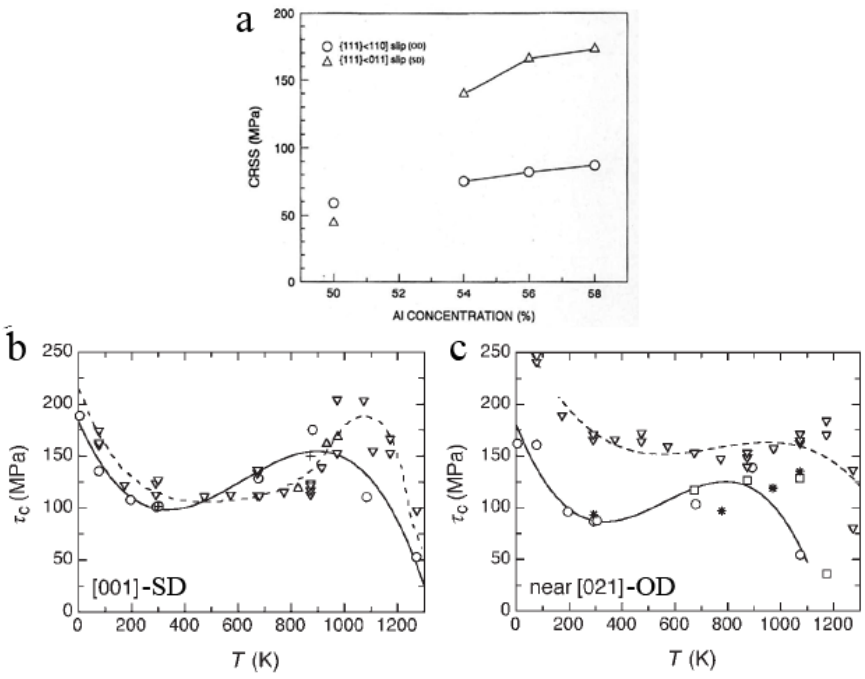

Fig. 1.14 Variation of the CRSS values corresponding to different slip systems with: (a) the Al content, for PST Ti-50Al [113] and Ti-54-58Al single crystals [119]; and (b, c) the temperature in ○▽ Ti-56Al, △ Ti-55.5Al , +Ti-56Al, □Ti-56Al and *Ti-54.5Al [7].

γ-TiAl alloys are susceptible to creep at low constant stresses and temperatures above 650 °C-750 °C ($T>0.4T_M$). The typical service conditions for LPT turbine blades (150 MPa, 750 °C) are comprised within these stresses and temperature ranges and, thus, improving the creep resistance of γ-TiAl alloys is of critical importance. A distinct feature of creep in γ-TiAl

alloys is that they usually exhibit a limited secondary creep region that is characterized by the absence of a steady-state, in which the creep rate reaches a minimum and then increases with strain leading to the tertiary stage [7, 127]. This minimum creep rate ($\dot{\varepsilon}_{\min}$) depends on the temperature, the stress, the alloy chemistry and microstructure [7, 128]. In addition, $\dot{\varepsilon}_{\min}$ is observed to vary as a function of the lamellae orientation with respect to the applied stress, as revealed by studies of PST TiAl alloys. While those with hard orientations exhibit a lower $\dot{\varepsilon}_{\min}$ than that associated to polycrystals, in the ones with soft orientations $\dot{\varepsilon}_{\min}$ is comparable to that of the latter [129, 130]. The application of the Dorn approach to α_2+γ TiAl polycrystalline alloys has rendered wide variations of the stress exponents, n, and of the activation energies for creep, Q_c, suggesting that the applicability of this phenomenological methodology to such complex microstructures is questionable [7, 130-132]. In general terms, dislocation slip and mechanical twinning are active during the secondary creep stage. In particular, dislocation climb appears to be the rate controlling process at stresses below a certain threshold, which depends of the microstructural parameters, such as colony size and lamellar spacing, and dislocation glide would be dominant at higher stresses [133]. At low strain rates diffusion-based mechanisms such as grain/colony boundary sliding (GBS/CBS) have been also observed to contribute to deformation, although their activation is still a matter of discussion [128, 134-139]. In particular, the influence of microstructural parameters such as the colony size and the presence of equiaxed grains on the incidence of GBS/CBS as well as the prevailing accommodation mechanisms, are not completely understood. Finally, degradation of the lamellar structures due to phase transformations and dynamic recrystallization, the formation of shear bands, grain boundary sliding and formation of voids is reported for the tertiary creep stage [7, 140]**.**

Fully lamellar TiAl microstructures outperform equiaxed and duplex microstructures in terms of creep resistance [128, 141-149]. Systematically increasing the volume fraction of the lamellar constituent in a microstructure composed of equiaxed γ grains and colonies of α_2+γ lamellae leads to lower creep rates and extended creep lives. In addition, significantly reduced creep rates for all stages have been observed for finer lamellar spacing (λ) in fully lamellar polycrystalline microstructures containing 140 <λ< 660 nm for Ti-47Al [142], 120 < λ< 450 nm for Ti-48Al [143], 55 <λ < 400 nm for Ti-45-2Nb-2Mn+0.8v% TiB_2 [134]. However, below such limits lamellae become unstable during elevated-temperature creep [7, 135, 150].

1.1.6.2 Fracture mechanisms

At room temperature γ-TiAl alloys undergo brittle fracture. Lamellar microstructures are known to have greater fracture toughness than duplex ones due to crack deflection at lamellar interfaces and to the development of microcracking and crack bridging ligaments [7, 151]. With increasing temperature the fracture toughness of both lamellar and duplex structures increases, but this effect is most pronounced in the latter [7]. Crack propagation mechanisms in lamellar microstructures depend on the temperature as well as on the relative orientation between the lamellae and the applied stress [115]. At room temperature in lamellar microstructures, cracks may propagate both across lamellae (translamellar) or along lamellae interfaces (interlamellar) [114, 129, 152, 153]. When the lamellae are oriented parallel to the loading axis, cracks are perpendicular to the lamellae interface and propagate following a zigzag path. This translamellar crack propagation highly depends on the resistance of the different interfaces and gives rise to very rough fractures surfaces. When the lamellae are perpendicular to the loading axis cracks propagate along the lamellae interfaces, causing delamination and lead to a typical cleavage-like fracture. Cleavage occurs along the habit planes and tends to start on the α_2/γ higher energy interfaces. Finally, when lamellae are inclined with respect to the loading axis a mixed fracture behavior is observed. Nevertheless, higher incidence of delamination and cleavage has been reported. In duplex microstructures, transgranular cracks predominate. At high temperatures, colony and grain boundaries and, in particular, triple points, are favorable sites for crack nucleation and propagation in lamellar and duplex microstructures. The nucleation of wedge cracks due to grain/colony boundary sliding is often observed [154, 155].

1.1.7 Industrial applications

γ-TiAl alloys are established as recognized and attractive alloys for the aerospace industry [3-6] owing to their high specific properties combined with its good behavior under high temperature service conditions. With the aim of reducing fuel consumption, aircraft companies plan to substitute the older and heavier Ni-base superalloys with the novel and lighter γ-TiAl alloys, with the key objective of reaching a 40 % weight reduction. Aircraft engine components must perform well under different pressure and temperature conditions depending on their position with respect to the combustor system. Therefore specific materials must be considered for the different engine sections in order to reach high efficiency levels under low fuel consumption. Particularly, gamma titanium aluminides are thought to be

placed in the low pressure turbines (LPT) blades which make 20% of the engine's weight and which operate at temperatures of about 750 °C [5-7, 156, 157].

These materials and, in particular, the Ti-48Al-2Cr-2Nb alloy, have already found commercial uses in General Electric (GE) engines in the last two stages of the seven-stage LPT blades on GEnx engines, which are used in Boeing 787 dreamliner planes that are flying for companies such as United Airlines, British Airways or Qatar airways. In May 2013, 240 engines were in service, with more than 585000 h of operation and 112000 cycles, performing with a 99.94% of reliability. On the other hand, Rolls-Royce (RR), in collaboration with ITP (Industria de Turbo Propulsores S.A.), the main company leading LPT manufacturing is betting for the Ti-45Al-2Nb-2Mn+0.8%TiB_2 alloy as the best candidate [158]. Since 2007, important efforts have been carried out by RR to incorporate TiAl intermetallics on Trent 1000 engines that were first used on flight in 2011 on Boeings 747 and 787.

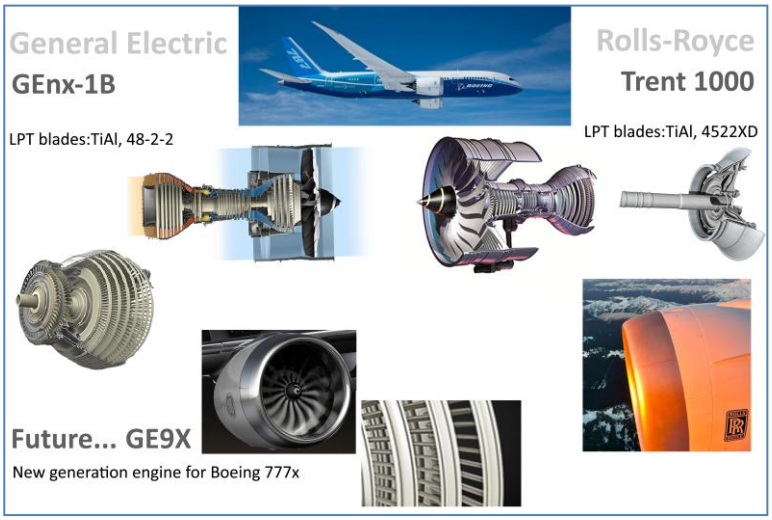

Fig. 1.15 γ-TiAl LPT Blades present on General Electric and Rolls-Royce engines for Boeing 787 manufacturing

γ-TiAl alloys are also potential lightweighting materials for the automotive industry. The high temperature capabilities of these materials allow for good service behavior on the combustion engine which must operate under elevated gas pressures and temperatures comprised between 850 °C and 1050 °C. Examples of these components are the engine intake and exhaust valves, the turbocharger wheels or the connection rods [7, 159, 160]. Inclusion of gamma TiAl alloys in Formula 1 cars is expected to be facilitated by new regulations which are about to be put in place in the period 2013-2014 [161].

Finally, γ-TiAl alloys are also being considered for high temperature nuclear applications owing to their superior creep, irradiation and oxidation resistance [162].

1.2 *In situ* electron microscopy

Traditionally, materials´ properties have been characterized through *ex situ* techniques using post mortem samples. Inherent limitations were always assumed as conclusions needed to be inferred from the acquired data or the materials inspection after testing. Actually, these *ex situ* characterization techniques have already allowed us to understand well known transformation mechanisms or to establish the relationship between the material's microstructures and their final mechanical properties, giving even the possibility to propose general models for a large variety of materials. Nevertheless, there is a lack of knowledge about when and how the transformations happen or how damage nucleates and progresses during constraining. Therefore, *in situ* electron microscopy techniques [163, 164] have been developed during the last decades in order to fill this gap.

The first works considering *in situ* electron microscopy date from the 1960s, when materials science found a necessity to describe more deeply dynamic processes [164, 165]. *In situ* electron microscopy has been utilized to investigate a wide variety of experiments and materials. Initially, *in situ* experiments were more frequently carried out by TEM [166-172]. However, *in situ* SEM works [163, 164, 173] have received increasingly more attention due to their high reliability and the recent significant improvements in high resolution SEM imaging. The following section will go into further explanation of *in situ* SEM techniques developed until today, which are relevant to the research work presented here.

1.2.1 *In situ* SEM experiments

In situ SEM experiments aim to understand the materials behavior by following SEM observations of morphological changes occurring in the course of time in the investigated samples under specific constraints [163, 174, 175].

In situ SEM experiments are mainly limited by the capabilities of the microscope and the planned research objectives (materials and applied constraints)[163, 175]. To carry out these dynamic experiments, the chambers of the microscopes are considered as microlaboratories where specific stages are included and different tests conditions are performed, varying temperature and pressure. Engineering advances on the design of stages for specimens, which support special experimental conditions and fit inside the tightly packed SEM chamber, have been critical on the development of *in situ* SEM techniques. High temperature *in situ* SEM experiments are in fact benefited by the not conductive, neither oxidative, vacuum properties within the chamber. However, considerable challenges are associated with heating and

thermal stabilization in vacuum atmospheres, as well as with measuring the reached temperatures [176]. Environmental scanning electron microscopes (ESEM) allow to carry out experiments under different atmospheres [164].

Due to the complexity of the *in situ* SEM experimental procedure, the behavior of the materials must be carefully evaluated *ex situ* before testing and the geometry of the samples should be designed according that. Sample's size can usually vary from 1 μm to 50 mm depending on the testing stage. *In situ* characterization of materials involving electron microscopy has been developed over the past decade to the point where high resolution SEM images combined with energy dispersive X-ray spectroscopy and electron backscattered diffraction (EBSD) maps [177] can be obtained dynamically at different strain levels. Currently only 2D surface observations [178] are possible, and therefore the constraints imposed on grains within a bulk specimen are not completely considered. However, in the near future this technique will be combined with the capabilities of focus ion beam (FIB) microscopy in order to facilitate examination of materials in 3D.

In situ SEM may be carried out under different constraints (atmospheric pressure, temperature, electrical or magnetic fields and load, among others). This technique has been utilized, on the one hand, to understand the fundamentals of different growth and transformation phenomena [163]. For example, in the area of metallurgy, it was utilized to investigate the titanium hcp to bcc phase transformation by Seward *et al*. [179], by using experimental devices similar to those developed by Bozzolo *et al*. [180] for *in situ* annealing experiments. *In situ* ESEM has also been utilized for biology and soft matter research [164, 181, 182]. Finally, the advent of *in situ* mechanical testing micromachines has allowed to analyze the materials deformation and fracture mechanisms [183-185]. This methodology has been mainly developed for metals research [186, 187], as will be reviewed in next section, although it has occasionally also been applied to analyze damage mechanisms in polymers [188], fiber-reinforced composites [189-192] or adhesive joints [193].

1.2.2 *In situ* SEM mechanical testing

In situ SEM mechanical testing aims to describe the deformation and fracture mechanisms of different materials by following the microstructure evolution of the samples under straining [163, 174]. *In situ* SEM mechanical testing experiments can be performed by applying different types of loading conditions [183], which include tension, compression, bending, creep and fatigue. In addition, *in situ* nanoindentation [184] is currently becoming a very useful technique to characterize mechanical properties in sub-micron scales. There are

multiple types of *in situ* mechanical testing stages. Microtensile testing machines with screw driven miniature load frames (Figure 1.16(a)) have been carefully placed below the beam gun during the last decade [194-196]. Moreover, recent advances on micro-electro-mechanical (MEMS) force sensors [197, 198] have allowed a scale reduction and more precision handling of the devices (Figure 1.16(b)). *In situ* SEM mechanical testing aided by digital imaging correlation (DIC) has also allowed a more precise measurement of the displacement or strains [199, 200], thus favoring a better correspondence between *in situ* and *ex situ* tests and with numerical models.

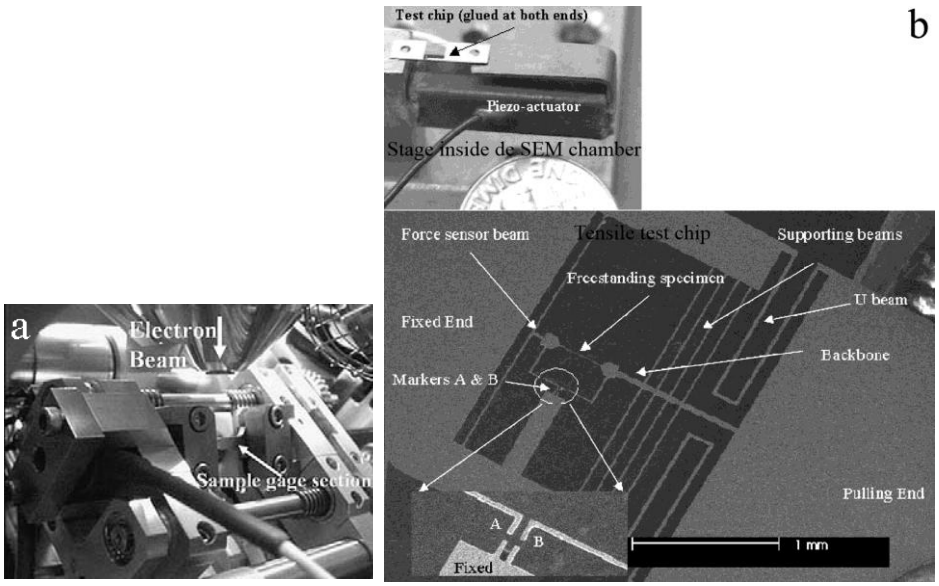

Fig. 1.16. *In situ* (a) microtensile stage and (b) tensile test chip formed by MEMS sensors and structures.

Owing to the high potential and versatility of this technique, multiple types of materials have been mechanically characterized *in situ* during the last years [201-213]. Among metals, pure titanium and titanium alloys, magnesium alloys, aluminum alloys, nickel alloys or steels. *In situ* SEM mechanical testing has been utilized to improve the current knowledge about slip, twinning or diffusion based deformation mechanisms at a wide range of temperatures. In particular, in combination with EBSD, it has significantly helped to examine slip and twin activity in metals [214-219], as it allows to assign the observed slip and twin traces to specific slip and twinning systems. Thus, it helps to better understand the kinetics of the different deformation mechanisms and to relate their activity to specific microstructural features. Furthermore, the possibility of observing crack nucleation and growth inside or along specific microfeatures facilitates the understanding of the failure mechanisms [220-227]. *In situ* SEM

mechanical testing become even more interesting when aiming to define thermomechanical behavior of materials, which requires applying high temperature conditions. It gives the possibility to exactly reproduce the real materials service conditions, such as the ones suffered in the engines environments, and so define possible service failure mechanisms. Most *in situ* tests have been carried out at temperatures up to 600 °C [228, 229], although higher temperatures have started to be utilized in recent years [230, 231]. Understanding the microscale deformation mechanisms is useful for modeling and simulations aiming to link the microscale to the mesoscale behavior. In turn, simulations require verification through *in situ* microscale observations. Thus, the information provided by *in situ* testing techniques is proved to be very useful to build more powerful models that predict more accurately the mechanical behavior given the processed microstructural condition.

To date little work has been carried out in γ-TiAl by *in situ* SEM mechanical testing. A few studies have investigated the influence of the microstructure on the room temperature fracture mechanisms or the role of different interfaces in toughening through shear ligament formation [232-238]. However, the high temperature *in situ* mechanical behavior of γ-TiAl alloys has still not being deeply investigated [239].

Motivation and objectives

2

2. Motivation and objectives

2.1 Motivation

There are several important challenges that have to be overcome before γ-TiAl alloys can replace the current Ni superalloys in high temperature aerospace components. In particular, among them, the high-temperature capabilities of these materials must be improved in order to enhance their service life. Moreover, the intricate nature of the γ-TiAl alloys' microstructures, governed by a large number of parameters (composition, colony and grain size, lamellae size, volume fraction of the two phases, misorientation and character of the interfaces), makes isolating the correlation of one microstructural feature to the mechanical properties difficult. In order to solve this demanding task, further analysis of the deformation and fracture mechanisms might be helpful to understand the relationship between the microstructure and the mechanical properties under service conditions and it would facilitate the microstructural design of γ-TiAl alloys for a wider range of engineering applications.

Characterization of the deformation and fracture mechanisms in γ-TiAl intermetallics has been mostly carried out by *ex situ* mechanical testing. These testing methods have limitations as it is not possible to know neither the order of activation of the different deformation modes nor the stress or strain at which they occur during the experiment. Furthermore, characterization of the dislocation activity in γ-TiAl intermetallics has been mostly carried out by transmission electron microscopy (TEM). While this technique allows resolving individual dislocations, it has inherent limitations [240], including the difficulty in sampling large volumes, the likelihood of removing dislocations during sample preparation and the damage of the thin area by beam irradiation, which might bias the analysis. The previously explained disadvantages can be overcome by the utilization of *in situ* testing methods, which allow for the observation of the microstructure evolution in real time and therefore facilitate the study of the kinetics of the deformation and failure mechanisms. *In situ* mechanical testing in the scanning electron microscope (SEM), aided by electron back-scattered diffraction (EBSD), is

emerging as a complementary method to analyze slip activity in metallic materials [241, 242]. This technique, which has not been utilized to date to investigate γ-TiAl alloys, would clearly be very helpful to understand the links between the microstructure and the activation of different deformation and fracture mechanisms in these intermetallics.

2.2 Objectives

The main objective of this research work is to **investigate the relationship between the microstructure and the high temperature deformation and fracture mechanisms of a γ-TiAl alloy (Ti-45Al-2Nb-2Mn(at.%)-0.8vol.%TiB_2) by *in situ* mechanical testing in the SEM aided by EBSD**. The following partial objectives derive from the previous general one:

- To **generate a large variety of microstructures** in the Ti-45Al-2Nb-2Mn+0.8vol.%TiB_2 alloy by centrifugal casting and powder metallurgy, followed by heat treatments. A thorough characterization of all the microstructures thus generated will be carried out, consisting on the estimation of the grain and colony sizes, of the interlamellar spacing and of the lamellae boundary misorientation.

- To investigate the deformation and fracture mechanisms of the different Ti-45Al-2Nb-2Mn+0.8vol.%TiB_2 alloy microstructures generated. With this purpose ***in situ* mechanical testing inside a scanning electron microscope (SEM), aided by EBSD**, will be performed at room and high temperature (580 °C-700 °C) and the evolution of the microstructures during straining will be characterized.

- To establish links between selected microstructural parameters and the active deformation and fracture mechanisms.

3 Experimental procedure

3. Experimental procedure

3.1 Material and processing

The γ-TiAl intermetallic alloy studied in this work had a nominal composition of Ti-45Al-2Nb-2Mn(at.%)-0.8vol.%TiB_2, also known as Ti4522XD [56-58]. The intermetallic was processed by centrifugal casting and powder metallurgy routes in order to generate a range of different microstructures. The processing methods are described below.

3.1.1 Centrifugal casting

The Ti4522XD alloy was processed by centrifugal casting in the form of low pressure turbine blades (CC-LPT) and rectangular cast specimens (CC) (Figure 3.1). The CC-LPT blades (Figure 3.1(a)) were provided by Industria de Turbopropulsores S.A. (ITP, Bilbao, Spain). This material was centrifugally cast at the Institute of Metals Research of the Chinese Academy of Science (Shenyang, China) and subsequently hot isostatically pressed at 1260 °C and 140 MPa for 4 hours in order to remove any remnant porosity. Blades were finally heat treated at 1080 °C for 8 hours in a vacuum furnace followed by furnace cooling. The rectangular cast ingots specimens (CC) (Figure 3.1(b, c)) were centrifugally cast at ACCESS e. V. TechCenter (Aachen, Germany) [78]. Samples were centrifugally cast in a Linn Supercast equipment with the following conditions: Mould rotation velocity=250 rpm; mould preheating temperature: 1200 °C; superheat: 20-100 °C; ceramic moulds coated with Y_2O_3. The cast specimens were subsequently hot isostatically pressed at 1185 °C and 170 MPa for 4 hours in order to remove any remnant porosity. The dimensions of the castings were 44 mm x 20 mm x 2.5 mm.

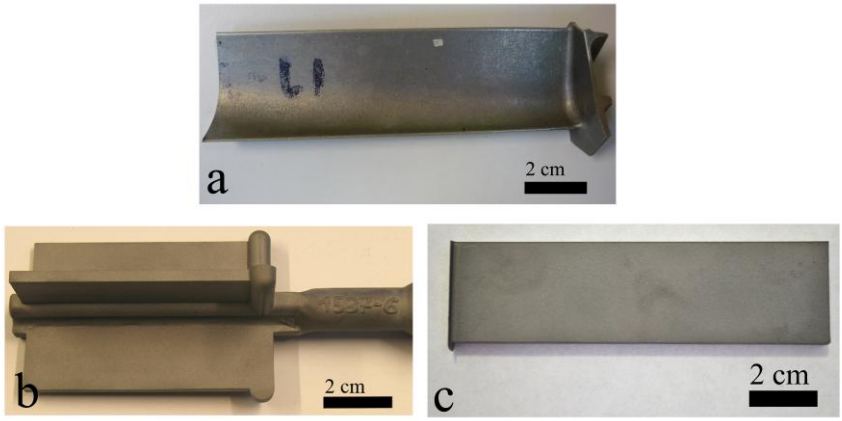

Fig. 3.1 Ti4522XD cast samples: (a) CC-LPT blade and (b, c) rectangular centrifugal castings (CC).

3.1.2 Powder metallurgy route

The starting material was gas atomized prealloyed powders (Ti4522XD) produced by EIGA [66] (Electrode induction gas atomization) in the Helmholtz-Zentrum für Material und Küstenforschung GmbH (Geesthacht, Germany).

The Ti4522XD intermetallic prealloyed powders were consolidated by hot isostatic pressing (HIP) at 1200 °C and 200 MPa during 4 hours at the Forschungszentrum Jülich (Jülich, Germany). The as-HIPed material will be called hereafter PM material.

The Ti4522XD powders were also pressed by field assisted hot pressing (FAHP) in a Gleeble 3800 equipment (Dynamic Systems Inc., USA), which allows physical simulation of processing. In this case it was used to perform the pressing and sintering steps simultaneously, by applying a continuous low frequency alternate current to heat the material by Joule effect. The prealloyed powder was poured into specific cylindrical graphite dies for the consolidation. The dimensions of the graphite die and punch set-up are shown on Figure 3.2(a). During processing, the temperatures in the two punches and the center of the die were registered. For this purpose, three thermocouples were glued with high temperature cement. An outside view of the Gleeble vacuum chamber with the gripped graphite die during processing is shown in Figure 3.2(b). The graphite die was gripped at a constant defined load inside the vacuum chamber. The applied load was 50 MPa and it was applied once the degassing temperature was reached. By observing the vacuum pressure, it was established that the degassing was stabilized at temperatures above 200 °C. The γ-TiAl alloy has been processed by FAHP for a

period of 2 to 10 minutes at different temperatures. The conditions were: FAHP1, 900 °C - 10 min; FAHP2, 1000 °C - 10 min; FAHP3, 1100 °C - 10min; FAHP4, 1250 °C - 10 min; FAHP5, 1350 °C - 2 min. The heating rate was always programmed to be 100 °C/min, while the cooling rate registered was of 140 °C/min.

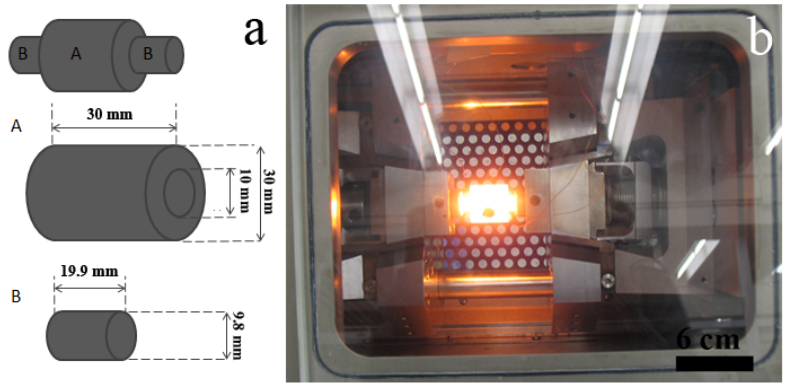

Fig. 3.2 (a) Graphite die and punch dimensions and (b) interior of the Gleeble 3800 chamber during FAHP.

3.1.3 Thermal analysis and heat treatments

Differential thermal analysis (DTA) was performed in a Setsys Evolution thermogravimetric analyzer TGA & DTA/DSC (Setaram, France) in order to determine the phase transformation temperatures corresponding to the alloy investigated.

Post processing heat treatments were performed with the aim of generating a variety of microstructures. Heat treatments were performed in a muffle furnace, where the heating rate was always programmed to be 10 °C/min. In order to avoid possible oxidation during heat treatments, the samples were wrapped in Ta foil and encapsulated in purged quartz tubes filled with Ar (Figure 3.3). In particular, the CC specimens were solution treated during 2 hours at 1300 °C and subsequently cooled in water (water quenching, CCWQ), in oil (oil quenching, CCOQ), in air (air cooling, CCAC) and in the furnace (furnace cooling, CCFC). CCWQ samples were subsequently annealed at 850 °C, 950 °C and 1150 °C during 1 hour and 8 hours in order to decrease internal stresses and to analyze the effect of the annealing temperature on the microstructure. Samples were identified as: CCWQ850C-1h, CCWQ850C-8h, CCWQ950C-1h, CCWQ950C-8h, CCWQ1150C-1h, CCWQ1150C-8h, respectively. The PM material was also heat

treated during two hours at 1300 °C and, subsequently, quenched in water and cooled in the furnace. The samples thus obtained were named PMWQ and PMFC, respectively. The PMWQ material was subsequently annealed at 850 °C during 8h in order to reduce internal stresses and samples were named PMWQ850C-8h.

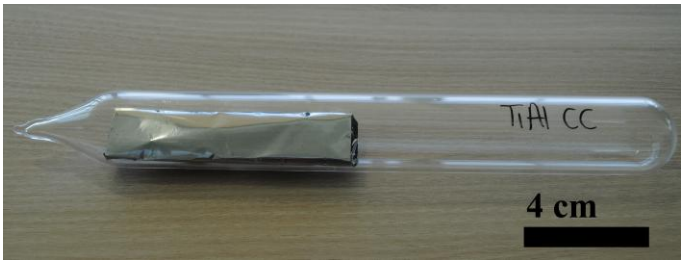

Fig. 3.3 CC Ti4522XD sample wrapped in Ta foil inside a quartz tube filled with Ar.

3.2 Microstructural characterization

X-ray diffraction (XRD) was utilized to identify the phases present in the processed materials. Room and high temperature (600 °C-1000 °C) XRD was performed using a X-ray diffractometer Philips Panalytical X'Pert PRO MPD (Almelo, The Netherlands), furnished with an Anton Paar HTK 1200 temperature chamber (Graz, Austria). The used X-ray beam corresponded to the K_α Cu excitation line (λ=1.542 $\dot{A}$) obtained by an X-ray tube consisting on a Cu anode and a W filament excited with a 40 mA current. The potential to accelerate the electrons was of 40 kV. The samples were scanned varying the 2θ angle from 15 ° to 80 ° with a defined step of 0.03 °. Sample preparation for XRD examination consisted of fine grinding using increasingly finer SiC grits (down to 1200).

Microstructure analysis was also performed using scanning electron microscopy (SEM) and transmission electron microscopy (TEM). SEM analysis was carried out in a Zeiss (Jena, Germany) EVO MA15 system equipped with Energy Dispersive Spectroscopy (EDS) capabilities (Oxford INCAx-act) and in a field emission gun Mira-Tescan (Brno, Czech Republic) SEM. Samples for SEM examination were cut with a diamond disk and mounted in an epoxy resin. They were then polished using silicon carbide paper and diamond paste and, finally, with 0.06 µm colloidal silica. The average colony size was determined using the ASTM grain size standard [243] on the backscattered (BSE) SEM micrographs with the Olympus Image Analysis software. TEM analysis was performed using a FEI Instruments (Oregon, USA) Tecnai T20 TEM at 200 kV and also using a JEOL JEM 2100 (Tokio, Japan) TEM at 200 kV. The TEM foils were prepared by grinding down the material to a thickness of approximately 200 µm, then punching 3 mm

diameter disks, and finally thinning them to electron transparency using a Struers (Ballerup, Denmark) twinjet Tenupol-5 electropolisher until perforation. The electropolishing solution, which consisted of 5% perchloric acid, 35% butanol, 60% methanol, was held at a constant temperature of -30 °C and 40 V. The lamellar spacing was determined using several bright field TEM images, in the "edge-on" condition, and dark field imaging. The α_2 lamellar thickness was examined by isolating the (0001) α_2 diffraction spot of the [1120] α_2 selected area diffraction pattern (SADP), which overlaps the <110> SADP of the γ phase according to the $(0001)_{\alpha_2}\|\{111\}_\gamma$, $\langle 11\bar{2}0\rangle_{\alpha_2}\|\langle 1\bar{1}0|_\gamma$ Blackburn orientation relationship [40] (Figure 3.4). By comparing the α_2 lamellar width with λ, which constitutes the average lamellar width of both phases, the γ lamellae width was obtained.

Electron backscattered diffraction (EBSD) was carried out in a field emission Mira-Tescan SEM (Brno, Czech Republic) equipped with an EDAX-TSL (Mahwah, NJ, USA) EBSD system. Sample preparation for EBSD involved grinding using increasingly finer SiC paper, down to a grit size of 4000, followed by 4 h of polishing with a mixture of 0.04 μm colloidal silica and H_20_2. It is well known that, for γ-TiAl alloys with 45-48% Al the volume fractions of the α_2 and γ phases are, respectively, comprised within the intervals 5-20% and 80-95% [6, 7]. Since the γ phase has been recognized to accommodate most of the strain, only this phase was indexed. The fact that most of the examined areas were indexed with a high confidence index (CI>0.2) is consistent with the presence of a very small fraction of the α_2 phase. The structural parameters used to index the γ phase were a=0.3976 nm and c=0.4049 nm.

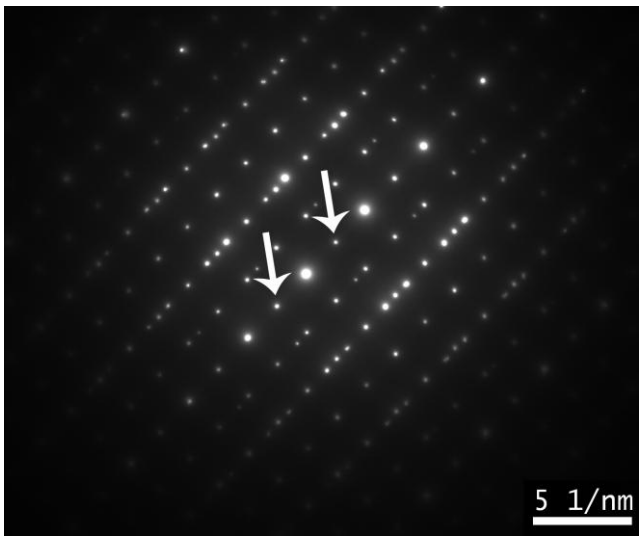

Fig. 3.4 [1120]α_2 SADP with arrows pointing (0001) α_2 reflections utilized for dark field imaging of the α_2 phase.

3.3. Mechanical behavior

3.3.1. *In situ* mechanical testing

The CC-LPT, CC, CCFC and PMFC materials were selected for the *in situ* mechanical tests, as they exhibited clearly different microstructures and therefore allowed for an investigation of the influence of various microstructural parameters on the mechanical behavior. Several tensile specimens were electrodischarge-machined from all these materials with the geometry illustrated in Figure 3.5. This unusual geometry was designed especially for these *in situ* tests in order to facilitate the location of the area in which fracture would initiate, which is of crucial importance for the detection of the crack nucleation sites and the follow-up of crack propagation. As the intermetallic alloy under study is significantly brittle, a flat notch of 1 mm was done in the gage section with the highest possible angle.

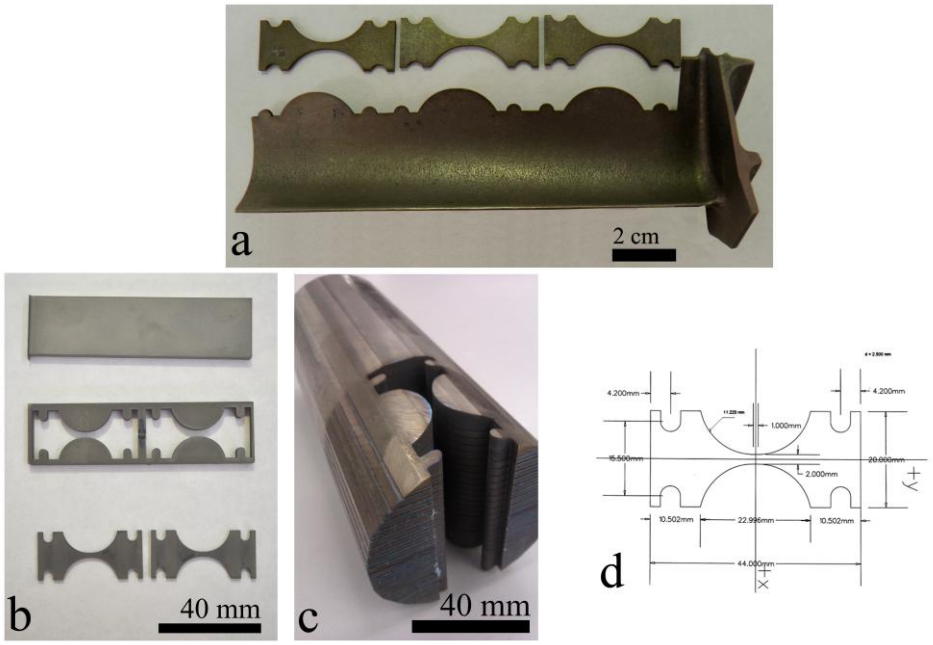

Fig. 3.5 Test specimens machined from (a) LPT blades (CC-LPT), (b) centrifugally cast rectangular bars (CC), and (c) HIPed ingots (PM); (d) schematic drawing of the tensile

Table 3.1 summarizes the conditions under which the different materials were tested. *In situ* tensile tests were conducted at a constant strain rate of $10^{-3}s^{-1}$ at room temperature (RT), 580 ± 30 °C and at 700 ± 30 °C, while *in situ* tensile-creep tests were carried out at 700 ± 30 °C and at constant stresses (σ_{cr}) ranging between 50 and 98% of the maximum flow stress (σ_{max}).

The maximum flow stress for the tested materials were: σ_{max}(CC-LPT)= 520 MPa; σ_{max}(CC)=460 MPa; σ_{max}(CCFC)=498 MPa; σ_{max}(PMFC)=467 MPa .

Table 3.1 *In situ* mechanical testing conditions

	$\varepsilon=10^{-3}s^{-1}$ RT	$\varepsilon=10^{-3}s^{-1}$ 580 °C	$\varepsilon=10^{-3}s^{-1}$ 700 °C	σ_{cr}=50-65%σ_{max} 700 °C	σ_{cr}=85%σ_{max} 700 °C	σ_{cr}=95%s_{max} 700 °C	σ_{cr}=98%σ_{max} 700 °C
CC-LPT	X		X	X			
CC	X	X	X	X	X	X	X
CCFC		X	X	X			
PMFC		X	X	X			

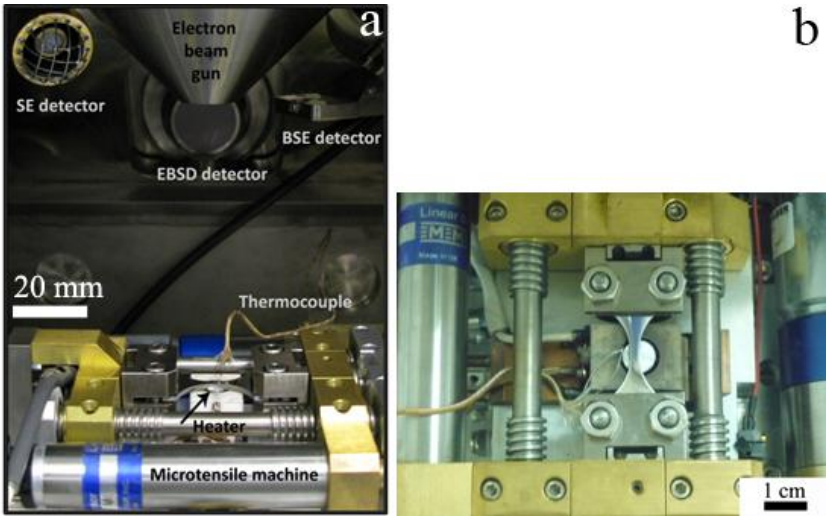

Fig. 3.6 (a) *In situ* tensile-stage inside the SEM; (b) view from the top of the gripped tensile sample on the in situ stage.

In situ tests were performed using the screw-driven tensile stage placed inside the SEM which is shown in Figure 3.6. The load was measured using a 4,448 N load cell. The tensile tests were performed at a displacement rate of 0.004 mm/sec ($\dot{\varepsilon}\sim10^{-3}s^{-1}$). For the tensile-creep tests the load was applied at 250 N/min until reaching 90% of the desired creep stress (σ_{cr}) and then at 25 N/min until reaching σ_{cr}. The temperature was controlled using a constant-voltage power supply to a 6 mm diameter tungsten-based heater located just below the gage section of the sample. An open-bath, closed-loop chiller was used to circulate distilled water at room temperature through copper tubes to prevent the tensile stage from overheating. In the case of CC, CCFC and PMFC samples, temperature was controlled using a fine-gage K-type

thermocouple spot-welded to the gage section of each sample. In CC-LPT test samples it was not possible to spot-weld the thermocouple without introducing damage and, thus, it was placed against the gage section. To have a more precise control of the tests temperatures in the CC-LPT samples, the temperature measured by the thermocouple placed against the sample's gage section (T_{inf}) was compared to another measurement by a spot-weld thermocouple in a damaged sample (T_{sup}). Figure 3.7 illustrates the values of T_{inf} and T_{sup} registered during heating. Once the gage-section´s desired temperature was reached, the sample was held at least 30 minutes prior to applying the load. The pressure in the SEM chamber never exceeded $4x10^{-6}$ torr, and therefore oxidation did not detrimentally affect the SEM imaging. Further details of this apparatus and testing technique can be found elsewhere [244, 245].

BSE SEM images were acquired before and after testing and secondary electron (SE) SEM imaging was carried out at periodic displacements during the tests. Tensile tests were thus interrupted at certain loads to acquire the mentioned SE images. However, due to the low strain rates typical of creep tests (10^{-3}-10^{-7} s^{-1}), SE SEM imaging did not require any test interruptions. The strain values were estimated from the displacement measurements taking into account the heated gage length of the samples.

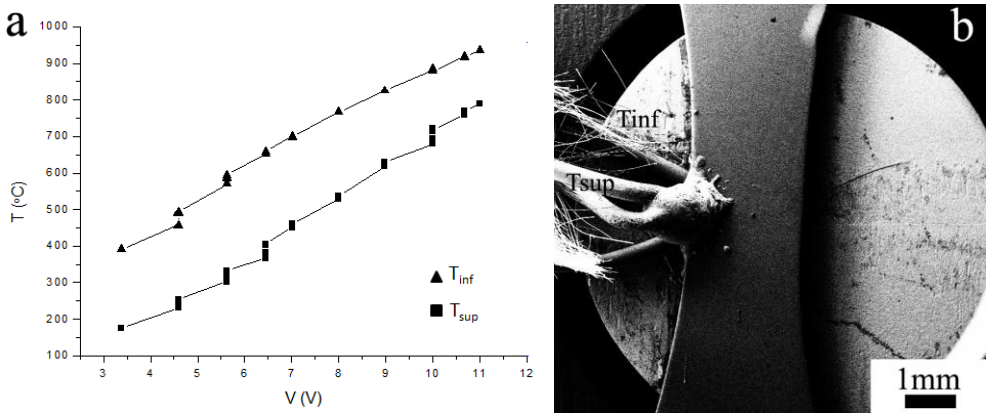

Fig. 3.7 (a) Calibration of the temperature measurement for the *in situ* tests in CC LPT samples, (b) secondary electron (SE) SEM micrograph showing the position of the two thermocouples during calibration.

3.3.2 *In situ* microtexture characterization: *Slip Trace Analysis*

The microtextures of CC, CCFC and PMFC samples were analyzed in selected areas of the specimens, before and after testing, by EBSD. Tensile and tensile-creep samples were prepared for EBSD as described previously (section 3.2). A challenge associated to EBSD examination of the γ-TiAl alloy under study is the large difference in size between individual lamellae and lamellar colonies, amounting to approximately three orders of magnitude. Thus, resolving individual lamellae required acquiring maps at high magnification, in which a limited number of colonies were included. In order to address this issue, orientation maps were obtained at several areas of the specimens´ gage length. Misorientation distribution histograms were analyzed for the *in situ* SEM studied areas before and after straining with the aim of investigating the evolution of the nature of the boundaries during testing.

The activation of different slip systems was estimated from the analysis of the slip plane traces visible in the SEM micrographs acquired *in situ* during straining and the EBSD orientation maps of the same areas. This analysis was performed following a previously detailed methodology [244-246] consisting of the following steps. First, identification on the SEM micrographs of a individual slip plane trace in a given grain (Figure 3.8(1,2)); second, calculation of the 12 plane traces corresponding to all slip systems of that particular grain by the cross product of each slip plane and the surface normal (Figure 3.8(3)); third, selection of the slip systems whose traces match the one observed experimentally. Due to the geometry of the fct lattice each observed trace is shared by three slip systems (one OD and two SD, in red in Figure 3.8(4)). Thus, determination of the actual active system is not trivial. In this thesis a methodology for slip system selection is proposed (section 4.2.4.).

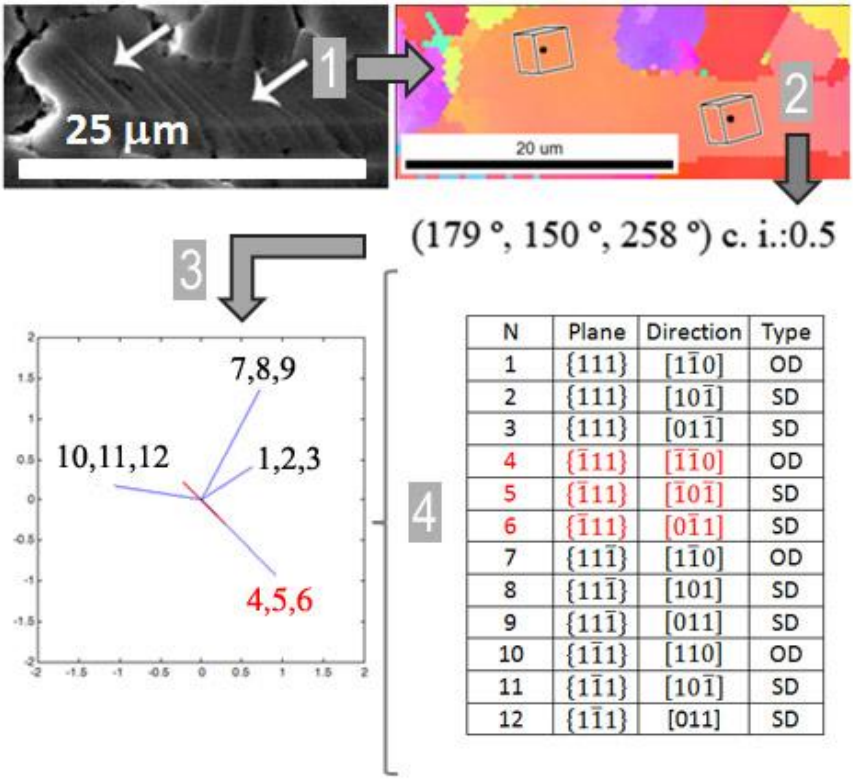

N	Plane	Direction	Type
1	$\{111\}$	$[1\bar{1}0]$	OD
2	$\{111\}$	$[10\bar{1}]$	SD
3	$\{111\}$	$[01\bar{1}]$	SD
4	$\{\bar{1}11\}$	$[\bar{1}\bar{1}0]$	OD
5	$\{\bar{1}11\}$	$[\bar{1}0\bar{1}]$	SD
6	$\{\bar{1}11\}$	$[0\bar{1}1]$	SD
7	$\{11\bar{1}\}$	$[1\bar{1}0]$	OD
8	$\{11\bar{1}\}$	$[101]$	SD
9	$\{11\bar{1}\}$	$[011]$	SD
10	$\{1\bar{1}1\}$	$[110]$	OD
11	$\{1\bar{1}1\}$	$[10\bar{1}]$	SD
12	$\{1\bar{1}1\}$	$[011]$	SD

Fig. 3.8 Slip trace analysis: 1-Slip trace identification by *in situ* SEM; 2-Measurement of the Euler angles in the studied region by EBSD; 3-Calculation of the traces corresponding to the 12 available slip systems; 4-Selection of the possible slip systems associated to an experimentally observed slip trace. Note that in this example slip systems 4, 5, 6 were all parallel to the slip trace. The methodology proposed to choose the active slip system out of this trio is described in section 4.2.4.

3.4 Experimental outline

Figure 3.9 summarizes the materials and experimental techniques utilized during this thesis.

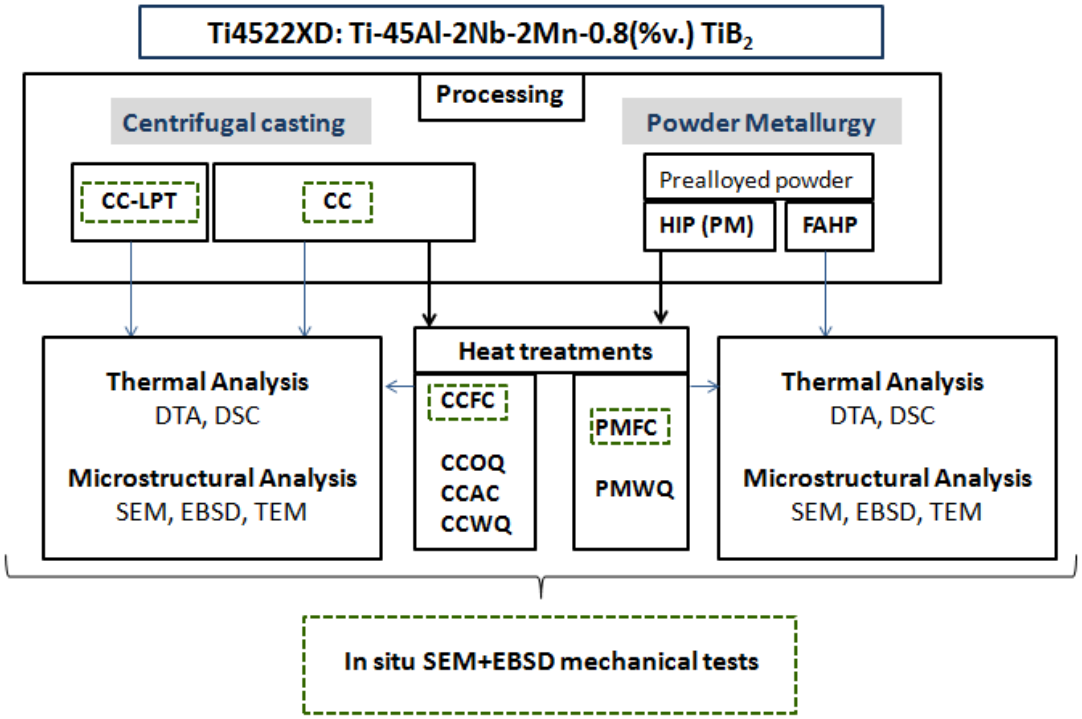

Fig. 3.9 Materials and experimental methods utilized during this research work.

4 Results and discussion

4. Results and discussion

4.1 Microstructural development

A wide range of microstructures were generated in order to investigate the link between microstructural parameters and the mechanical behavior. Two main processing routes were utilized, one based on centrifugal casting, the technique commonly used to fabricate turbine blades, and the second on powder metallurgy. Further microstructural development was carried out by subsequent heat treatments. In the following, the different microstructures are described in detail.

4.1.1 Centrifugal casting route

4.1.1.1 As-cast microstructures

The Ti4522XD alloy was processed by centrifugal casting in the form of low pressure turbine blades (CC-LPT) and rectangular cast specimens (CC). In Figure 4.1, the XRD pattern corresponding to the CC-LPT samples, reveals the presence of the two γ and α_2 phases. As shown in Figure 4.2(a, b), this material possesses a polycrystalline nearly lamellar microstructure formed by a minor fraction of equiaxed grains embedded in a matrix of lamellar colonies. Table 4.1 reveals the composition of the γ and α_2 phases (dark and bright contrast in Figure 4.2, respectively), measured by EDS in the SEM. B-rich reinforcement particles were identified by their typical globular and needle shapes and they were observed to be mainly located inside the colonies, along or across the lamellae. The distribution of colony sizes (CS) is very wide, as shown in Figure 4.2(c). The average CS is 194±121 µm, with values ranging from 52 µm to 636 µm. Figure 4.3(a, b) illustrates representative TEM images of the CC-LPT lamellar structure. As shown in Figure 4.3(c, d) the distributions of the lamellar spacing values corresponding to both phases (λ_γ and $\lambda_{\alpha 2}$) are also very wide. In particular λ_γ is comprised

within the interval [47, 1245] nm and $\lambda_{\alpha 2}$ within [85, 603] nm. The average values of the lamellar spacing of the γ and α_2 phases are 319±339 nm and 287±133 nm, respectively. The dispersion from average values is more pronounced in the γ phase than in the α_2 phase.

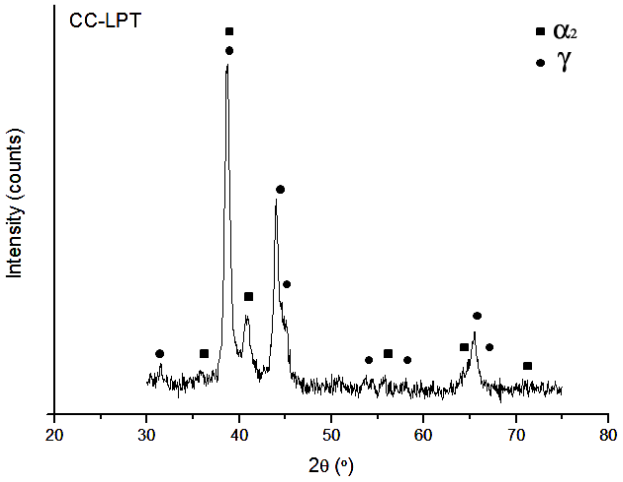

Fig. 4.1 XRD pattern of CC-LPT material.

Table 4.1 Semi-quantitative composition of the α_2-Ti_3Al and γ-TiAl phases measured by EDS.

	Bright BSE SEM contrast α_2-Ti_3Al (at. %)	**Dark BSE SEM contrast γ-TiAl (at. %)**
Ti	56.3	48.9
Al	39.9	47.3
Mn	1.4	1.3
Nb	2.4	2.4

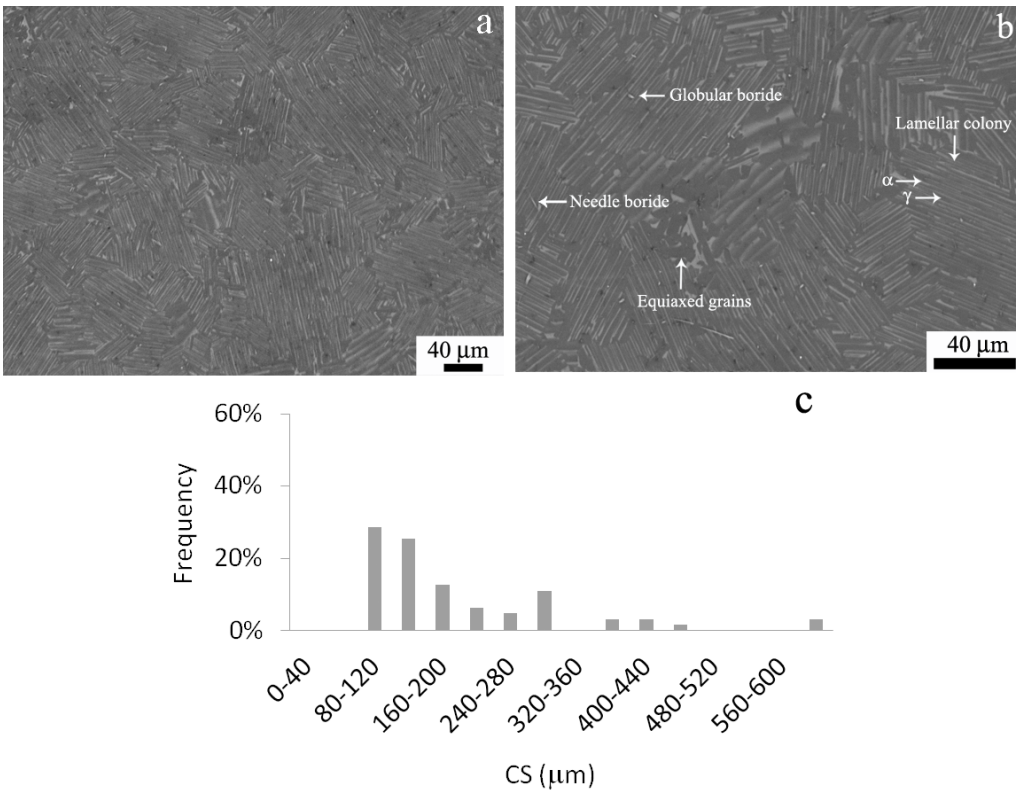

Fig. 4.2 (a, b) BSE SEM micrographs at different magnifications showing the CC-LPT nearly lamellar microstructure; (c) colony size distribution.

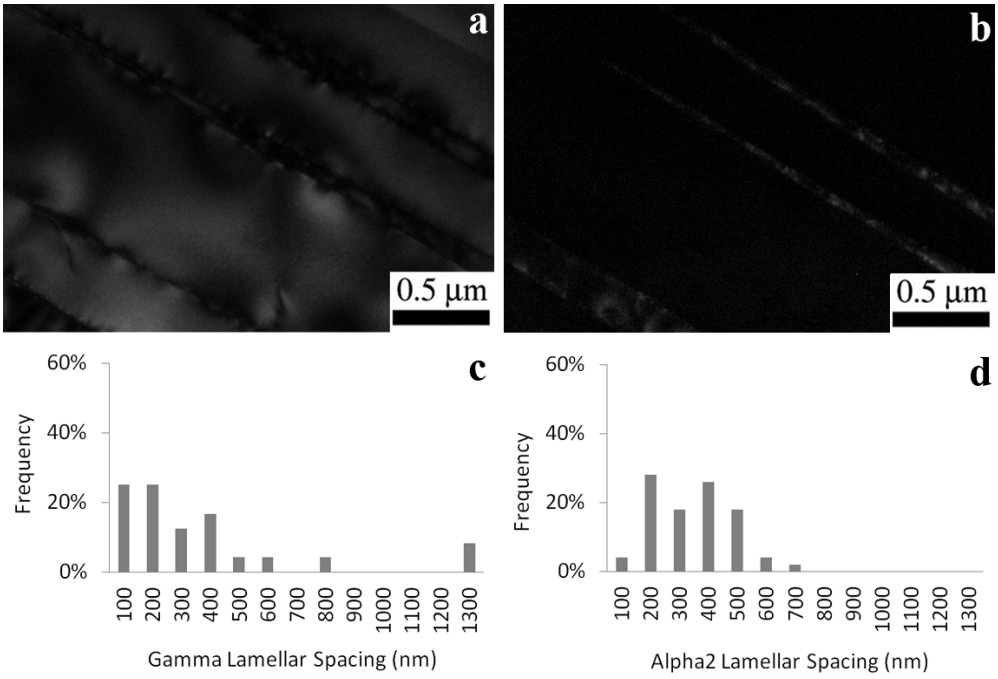

Fig. 4.3 TEM micrographs of the CC-LPT lamellae obtained by (a) bright field and (b) dark field imaging. In the latter, the bright areas correspond to the α_2 phase; lamellar spacing distribution corresponding to the (c) γ and (d) α_2 phase.

Figure 4.4, the XRD pattern corresponding to CC specimens, shows that their microstructure is also formed by the above mentioned two phases. Furthermore, as illustrated in Figure 4.5(a, b), they exhibit also a polycrystalline nearly lamellar microstructure with a small fraction of equiaxed grains. The B-rich phase is located both inside the colonies and at the colony boundaries and typically exhibits a lacey shape. The CC average lamellar CS is 126±52 µm, with values ranging from 40 µm to 252 µm (Figure 4.5(c)). Figure 4.6(a, b) illustrates the fine nature of the lamellae and the lamellar spacing distribution of both phases. The average lamellar thicknesses of the γ and α_2 lamellae are 465$\pm$270 nm and 286$\pm$288 nm, respectively. As shown in Figure 4.6(c, d), lamellar spacing distributions are very wide, with λ_γ values comprised within the interval [51, 1259] nm and $\lambda_{\alpha 2}$ values within the interval [30, 1259] nm.

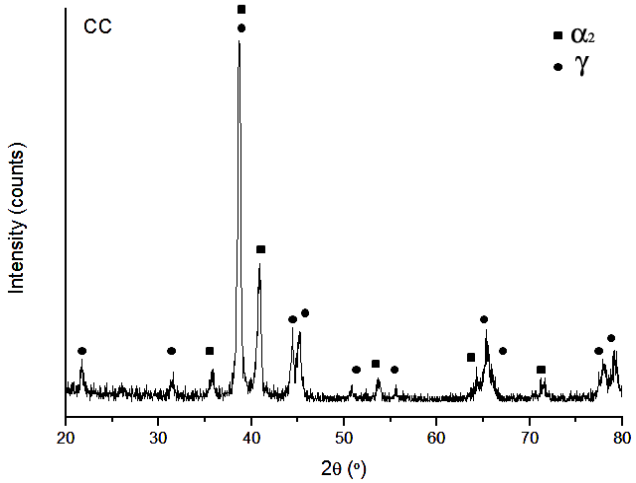

Fig. 4.4 XRD pattern of CC material.

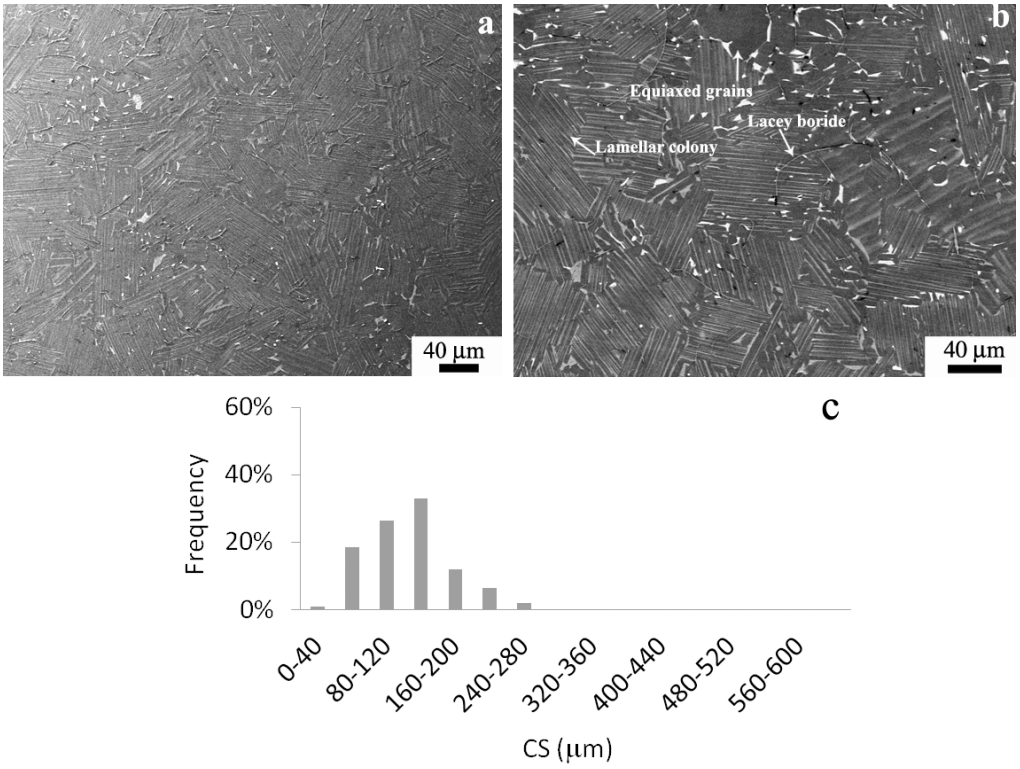

Fig. 4.5 (a, b) BSE SEM micrographs at different magnifications showing the CC nearly lamellar microstructure; (c) colony size distributions.

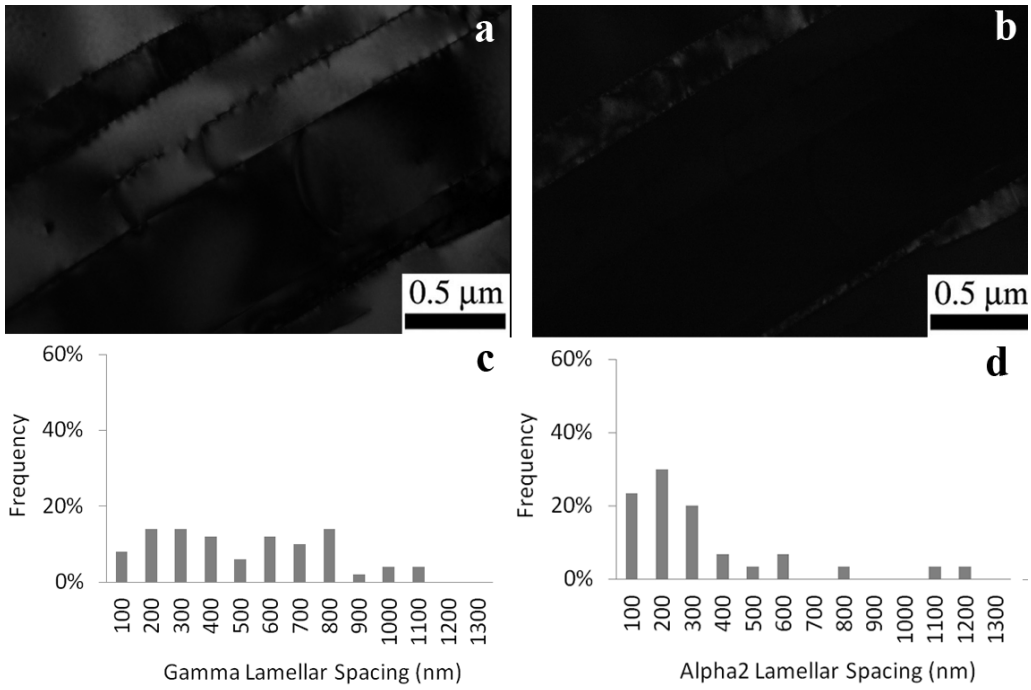

Fig. 4.6 TEM micrographs of the CC lamellae obtained by (a) bright field and (b) dark field imaging. In the latter the bright areas correspond to the α_2 phase. Lamellar spacing distribution corresponding to the (c) γ and (d) α_2 phase.

4.1.1.2 Cast and heat treated microstructures

The thermal behavior of the CC material was analyzed by differential thermal analysis (DTA) in order to determine the phase transformation temperatures and, thus, to design optimal post-processing heat treatments for the development of a wide variety of CC Ti4522XD alloy microstructures. Figure 4.7 shows the DTA analysis corresponding to this material. The following transformation temperatures were measured: $T_{cc\text{-}eutectoid}$= 1150 °C, $T_{cc\text{-}\alpha\ transus}$= 1290 °C and $T_{cc\text{-}melting}$= 1490 °C. Taking these values as a reference, the CC specimens were solution treated at 1300 °C during 2 hours and then cooled at different increasing rates: in the furnace (CCFC) at measured 10 °C/min, in air (CCAC) at measured 50 °C/min and by quenching in oil (CCOQ) and water (CCWQ). Still further microstructure development was pursued by carrying out annealing treatments in the CCWQ samples at temperatures close to $T_{cc\text{-}eutectoid}$, (850 °C, 950 °C and 1150 °C). The microstructures obtained following the various heat treatments are described below.

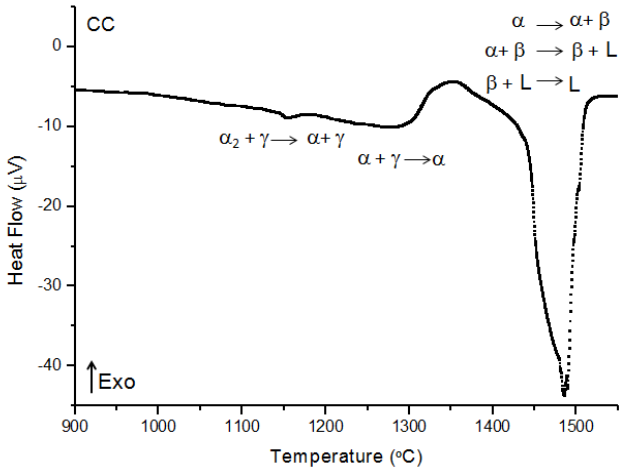

Fig. 4.7 DTA analysis of the CC Ti4522XD alloy.

The microstructure of the CCFC specimens was, again, formed by the α_2 and γ phases, as evidenced in the XRD pattern of Figure 4.8. The BSE SEM micrographs of Figure 4.9 and Figure 4.11 (a, b) revealed the presence of lamellar colonies and the almost complete absence of equiaxed grains defining a fully lamellar microstructure with well interlocked boundaries. Needle and globular borides were observed to be present inside the colonies. Lamellar CS ranged from 80 μm to 463 μm (Figure 4.9(c)), with an average value of 183±83 μm. TEM analysis revealed a significant lamellae refinement following this heat treatment (Figure 4.10 (a,b)). The average values of the lamellar widths were 210±140 nm and 160±160 nm for γ and α_2 phases, respectively. As shown in Figure 4.10(c, d), the distribution is very wide, with λ_γ values comprised within the interval [35, 471] nm, and $\lambda_{\alpha 2}$ values within [13, 578] nm, and with standard deviations close to the average values.

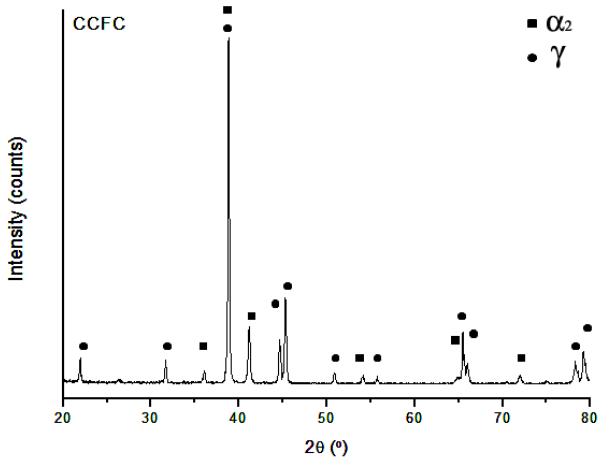

Fig. 4.8 XRD pattern of the CCFC material.

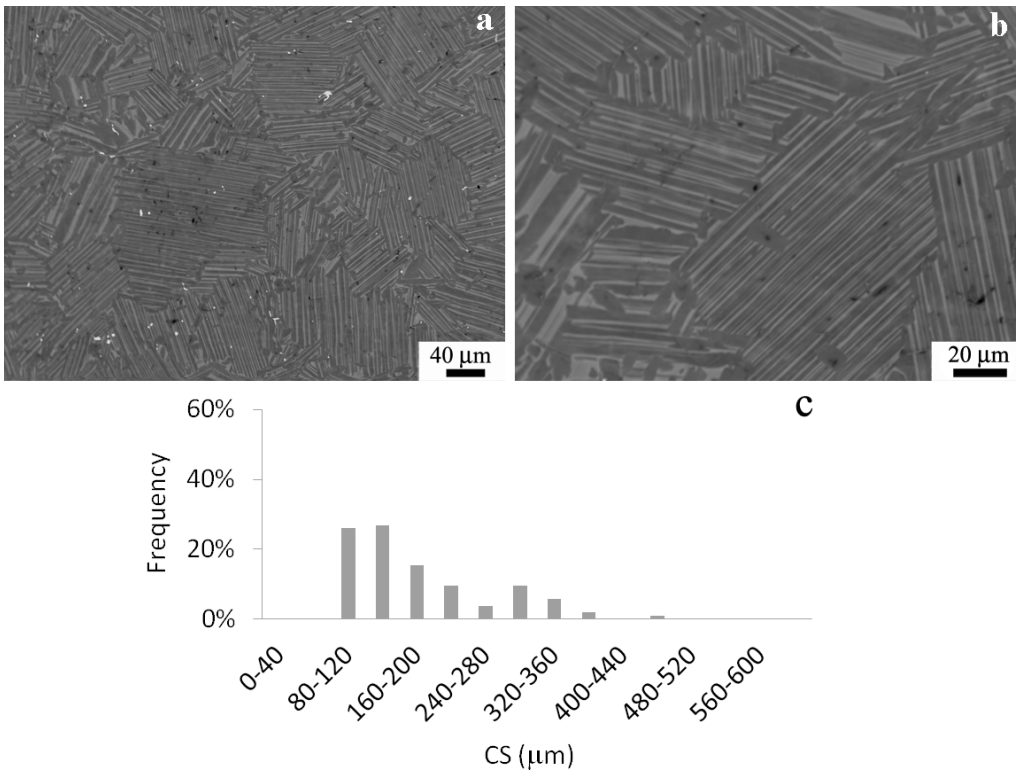

Fig. 4.9 (a, b) BSE SEM micrographs at different magnifications showing the CCFC fully lamellar microstructure; (c) colony size distribution.

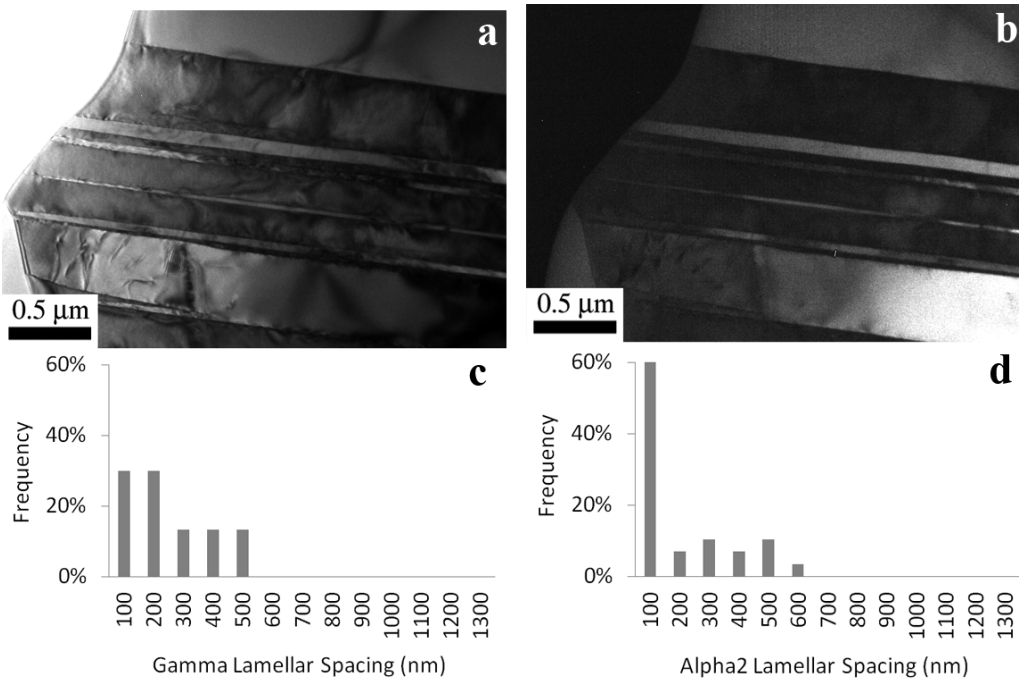

Fig. 4.10 TEM micrographs of the CCFC lamellae obtained by (a) bright field and (b) dark field imaging. In the latter, the bright areas correspond to the α_2 phase; lamellar spacing distribution corresponding to the (c) γ and (d) $\alpha_2$phase.

The main microstructural parameters of the specimens cooled in air (CCAC), as well as of those oil quenched (CCOQ) and water quenched (CCWQ) are compared in Table 4.2 and in Figure 4.11. All were characterized by fully lamellar (FL) microstructures with a considerable refining of CS and lamellar spacing with increasing cooling rate. CCWQ microstructures showed migration patterns along the lamellar colony boundaries that can be associated to retained microstructures at such high cooling rates. B-rich phases were observed in all the materials. Their morphology was found to vary with the cooling rate. A higher amount of globular and needle borides were present in the CCAC and CCOQ materials (Figure 4.11(d, f)), while lacey particles were more predominant in the CCWQ specimens (Figure 4.11(h))**.** The CCWQ material was subsequently annealed at 850 °C, 950 °C and 1150 °C during 1h and 8h in order to relieve internal stresses. Figure 4.12 illustrates the CCWQ microstructures obtained after the different annealing treatments and Table 4.2 classifies the microstructures obtained and summarizes the corresponding average lamellar CS values. Annealing at 850 °C during 1h and 8h (Figure 4.12(a, b)) resulted in the retention of the fully lamellar microstructure. Lamellar colony

boundaries were better defined and migration patterns disappeared. A significant coarsening of the CS was obtained after annealing during 1h, while longer annealing time gave rise to CS values similar to those of the CCWQ samples. Therefore, CCWQ-850-8h was considered a representative refined and stabilized microstructure for the Ti4522XD alloy. Annealing at temperatures close to the eutectoid point (950 °C and 1150 °C) promoted the development of gamma grains along the colony boundaries (white arrows in Figure 4.12(c-f)), i.e., the formation of duplex microstructures.

Table 4.2 Type of microstructure and average colony size of all the heat treated CC samples.

	Microstructure	**Average colony size (μm)**
CCFC	FL	183
CCAC	FL	111
CCOQ	FL	101
CCWQ	FL	88
CCWQ+850 – 1h	FL	116
CCWQ+850 – 8h	FL	85
CCWQ+950 – 1h	Duplex	117
CCWQ+950 – 8h	Duplex	121
CCWQ+1150 – 1h	Duplex	96
CCWQ+1150 – 8h	Duplex	83

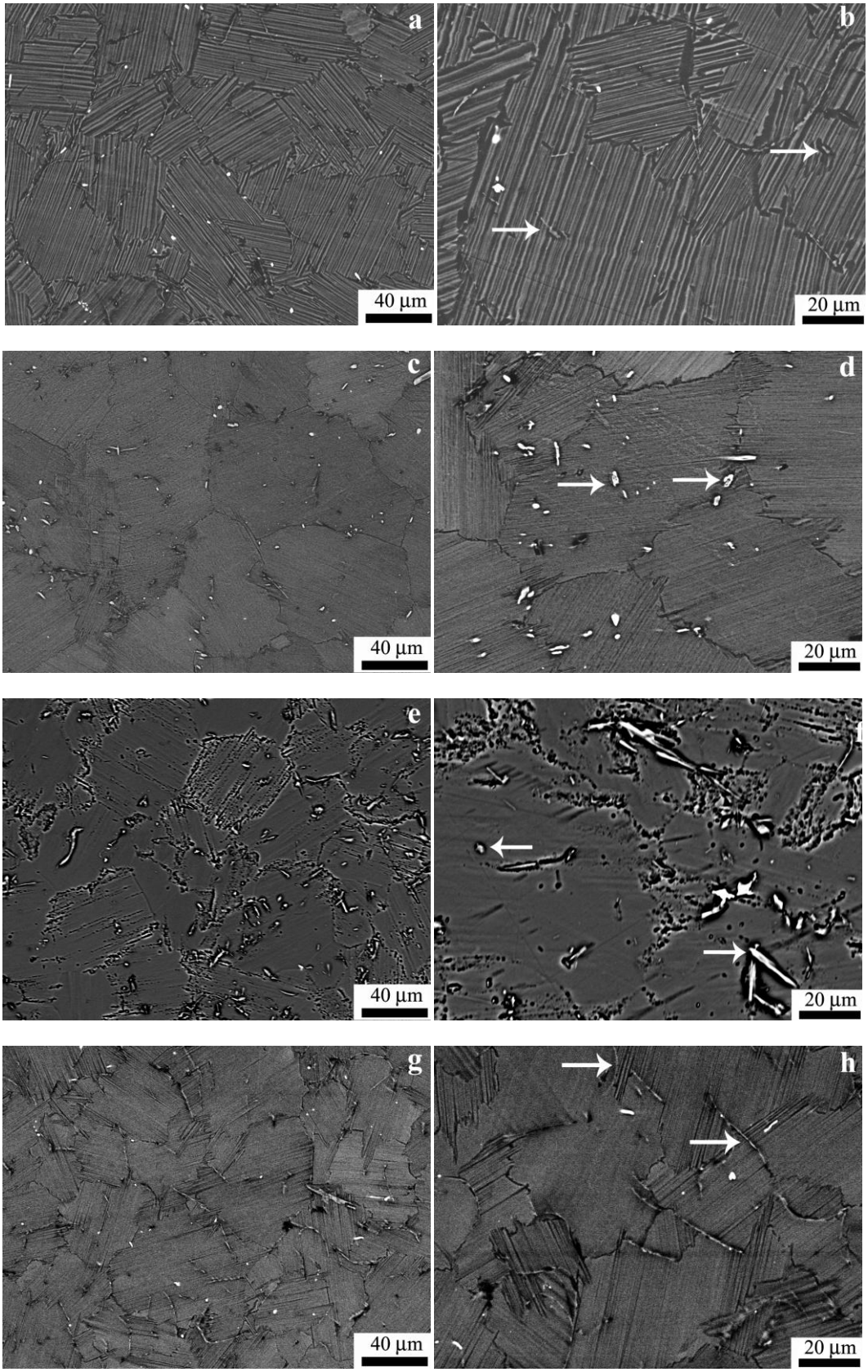

Fig. 4.11 BSE SEM micrographs showing the (a, b) CCFC, (c, d) CCAC (e, f) CCOQ and (g, h) CCWQ lamellar microstructures. White arrows point borides.

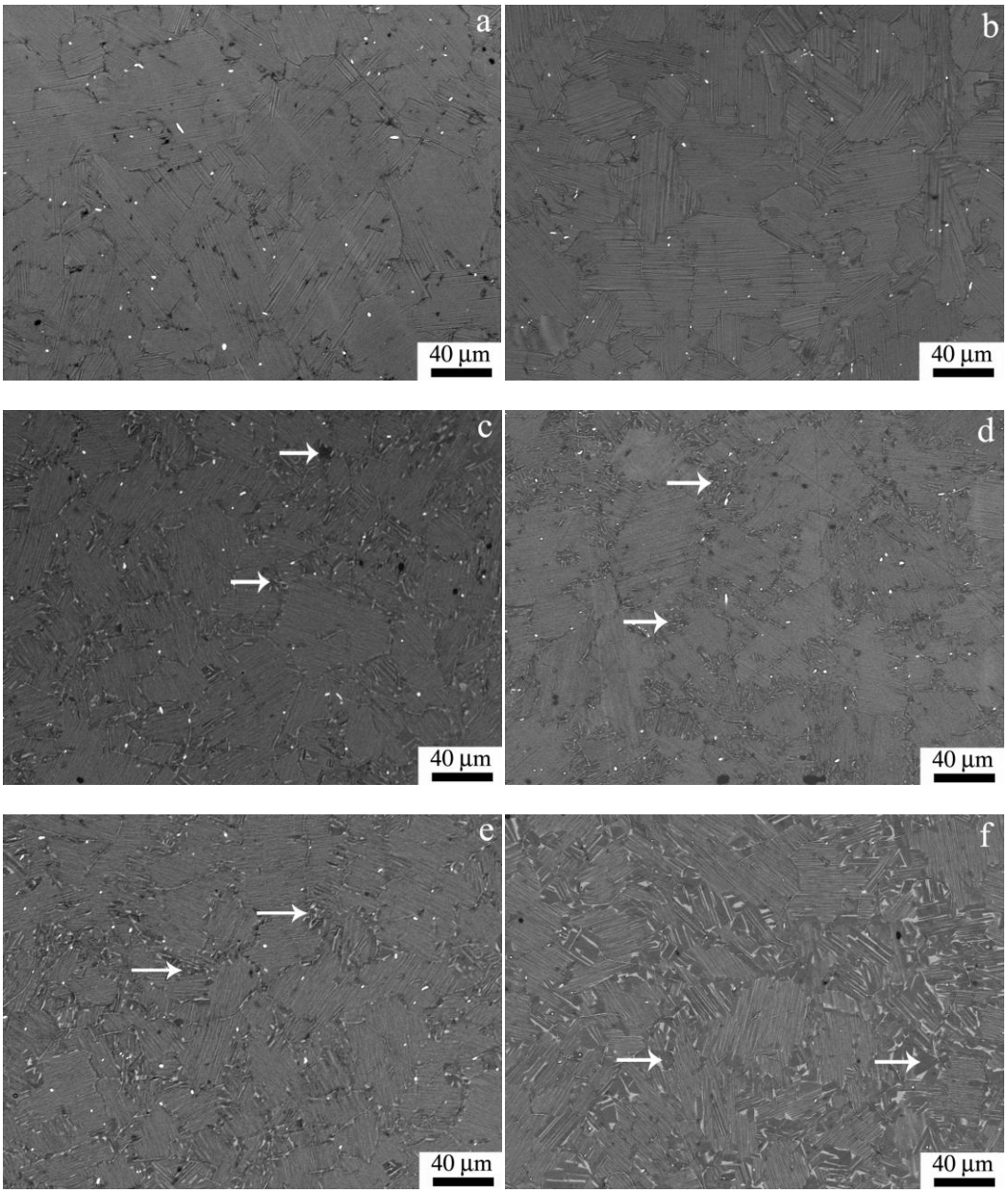

Fig. 4.12 BSE SEM micrographs showing the CCWQ+850 (a) 1h, (b) 8h; CCWQ+950 (c) 1h, (d) 8h; CCWQ+1150 (e) 1h, (f) 8h. White arrows point gamma grains along colony boundaries.

4.1.2 Powder metallurgy route

4.1.2.1 Prealloyed powder

The XRD pattern of the Ti4522XD prealloyed powder (Figure 4.13) shows that the material mainly contains the α-Ti_3Al phase (a=2.8175 $\dot{A}$; c=4.6100 $\dot{A}$). The absence of the superlattice peak at 2θ=26.2 ° confirms the absence of the α_2 stable phase. The estimated cooling rate reached during the EIGA [66] process is $\sim 10^5$ °C/s, a value lower than that considered as rapid solidification processes but higher than that typical of conventional gas atomization. The presence of the observed metastable α phase and the absence of the γ phase are consistent with this relatively high cooling rate. The gas atomized prealloyed powder had the typical spherical morphology shown in Figure 4.14. The average particle size was 51 μm and the particle sizes measured at 10, 50 and 90% of the total powder volume were 17.3, 51.2 and 117.8 μm, respectively. Different microstructures were identified in particles with different sizes (Figure 4.14 (a, b)).

BSE SEM micrographs reveal, in small particles (ϕ<50 μm) (Figure 4.14(a)), the presence of a darker matrix internally divided by a brighter phase in boundary regions. Due to the higher cooling rates that small particles suffer, it could be suggested that these particles are composed by not stable phases. Then, the matrix areas could be associated to α-metastable phase, while the brighter areas could be related to phases enriched by heavier β stabilizer elements. Larger particles (ϕ>50 μm) (Figure 4.14(b)) have a microstructure composed by dendrites that in some areas have grown into single grains thanks to longer solidification periods. Areas between the nucleated grains show darker channels that might be composed by higher Al concentration, the lowest melting point element. Nevertheless these channels are mainly characterized by bright ribbons which could be associated to the borides precipitation in the form of lacey shapes, as the reinforcements precipitates in lower solidification rates conditions [87]. Occasionally, as illustrated in Figures 4.14(c, d), the microstructure inside the particles is heterogeneous, and brighter large grain clusters become apparent. EDX analysis confirmed that the brighter regions contain higher Nb concentration and lower Mn concentration. The different microstructures obtained might be consequence of the size influence on the solidification rate at a constant pre-defined cooling rate during the EIGA. process. Similar microstructures have been reported by Yang *et al*.[87].

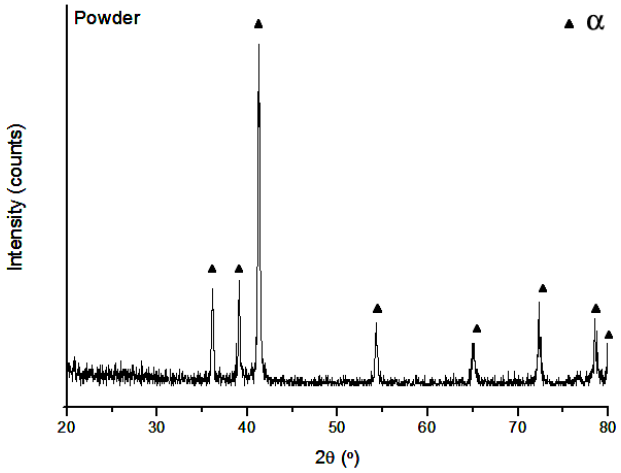

Fig. 4.13 XRD pattern of the as-atomized prealloyed Ti-45Al-2Nb-2Mn-0.8vol.%TiB_2 powder

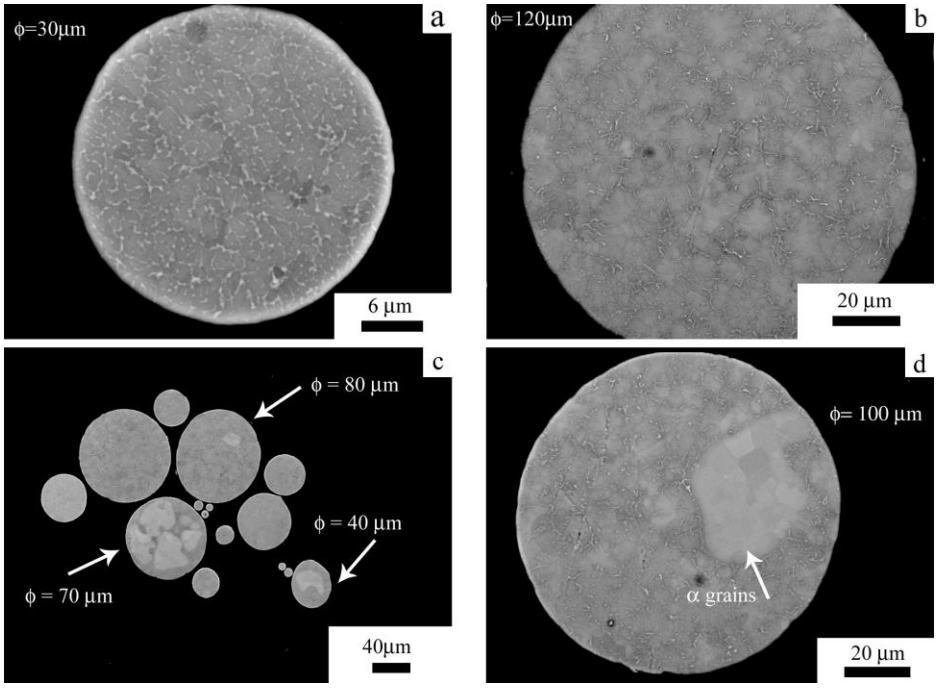

Fig. 4.14 BSE SEM micrographs showing the microstructure of the prealloyed powders: (a) 30 μm diameter particle and (b) 120 μm diameter particle; (c, d) single phase grain clusters present in particles of different sizes.

The thermal behavior of the prealloyed powder and the CC alloy is compared in Figure 4.15(a). Both DTA profiles are observed to be similar, except in the range of temperatures comprised between 600 °C to 750 °C, where the powders present a couple of peaks that are absent in the CC alloy. In order to understand the transformations occurring in the powder at these temperatures, high temperature XRD was performed in the powders at 600 °C, 800 °C and 1000 °C (Figure 4.15(b)). The XRD pattern obtained from the powder at 600 °C shows a decrease in the intensities of the α peaks. Increasing the temperature to 800 °C leads to a greater decrease of α peaks combined with the appearance of the γ-TiAl, and α_2-Ti_3Al peaks, suggesting that the α metastable phase started to transform into $\alpha_2+\gamma$ at around this temperature. Finally, at the highest temperature (1000 °C), the transformation is completed and the α_2 and γ peaks intensities are higher and clearly recognizable. The transformations observed by high temperature XRD are consistent with the reported DTA profile. It seems that once the metastable powder is heated to temperatures above 800 °C, stable γ phase appears and rising the temperatures leads to the stabilization of $\alpha_2+\gamma$ phases, according to the equilibrium phase diagram [22, 70, 93, 102]. Therefore, in order to achieve a complete transformation during the consolidation of the previous α metastable powder, the sintering temperature must be equal or greater than 1000 °C.

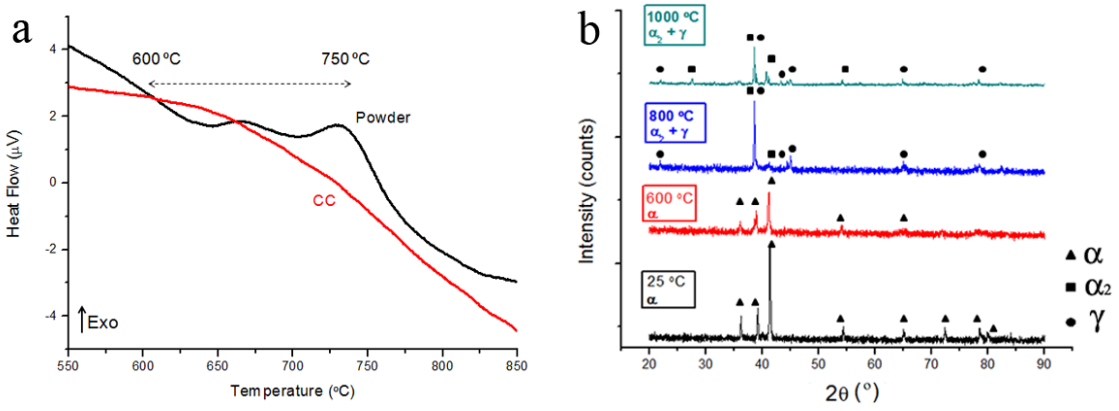

Fig. 4.15 (a) DTA analysis comparing the prealloyed powder and the CC materials showing different thermal behavior at 600 °C - 750 °C; (b) XRD patterns of prealloyed Ti4522XD powder at 25 °C, 600 °C, 800 °C and 1000 °C.

4.1.2.2 Hot isostatically pressed material

The as-atomized prealloyed powders were HIPed at 1200 °C and 200 MPa during 4h. During HIPing the α metastable phase transformed into the γ and α_2 stable phases, as illustrated in the XRD pattern of Figure 4.16. The BSE SEM micrographs of Figure 4.17 reveal that the as-HIPped PM material developed a near gamma microstructure in which the former powder particles could still be distinguished. Brighter areas are visible in the former powder boundaries and could be associated with a higher concentration of the α_2-Ti_3Al phase. The near gamma microstructure was characterized by an average grain size of 4.4±2.6 μm. Grain sizes varied within the interval [0.6-11.4] μm.

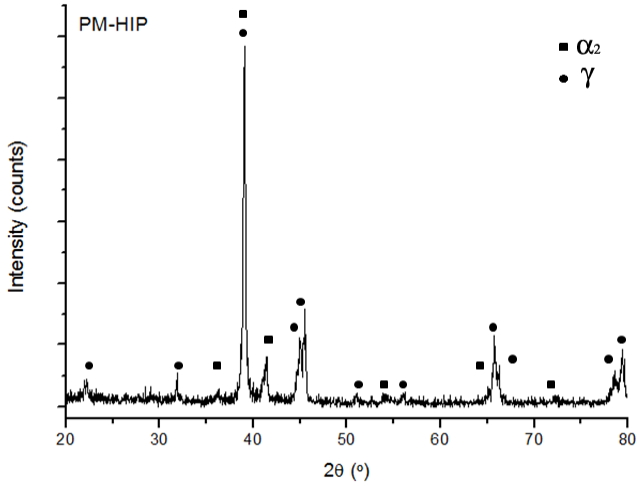

Fig. 4.16 XRD pattern of as-HIPed material.

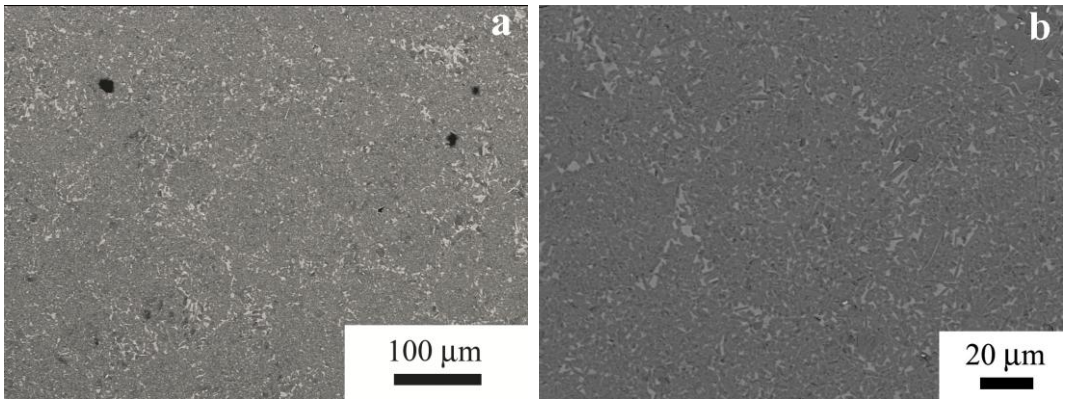

Fig. 4.17 (a, b) BSE SEM micrographs of the as-HIPed PM material.

4.1.2.3 Hot isostatically pressed and heat treated material

The HIPed PM material was solution treated during two hours at 1300 °C and, subsequently, furnace cooled (PMFC) and water quenched (PMWQ). The PMWQ material was subsequently annealed at 850 °C during 8h in order to reduce internal stresses (PMWQ-850-8h). Figure 4.18 illustrates the XRD patterns of the PMFC and PMWQ-850-8h samples, revealing that they were composed by the γ and α_2 equilibrium phases. The PMFC material had a duplex microstructure (Figure 4.19(a, b)), formed by equiaxed gamma grains with an average size of 4±1 μm and lamellar colonies of 98±34 μm in diameter. The PMFC lamellar CS ranged from 45 μm to 205 μm. The CS distribution is shown in Figure 4.19(c). In contrast, the PMWQ-850-8h sample exhibited a refined fully lamellar microstructure (Figure 4.20) with an average CS of 33 μm.

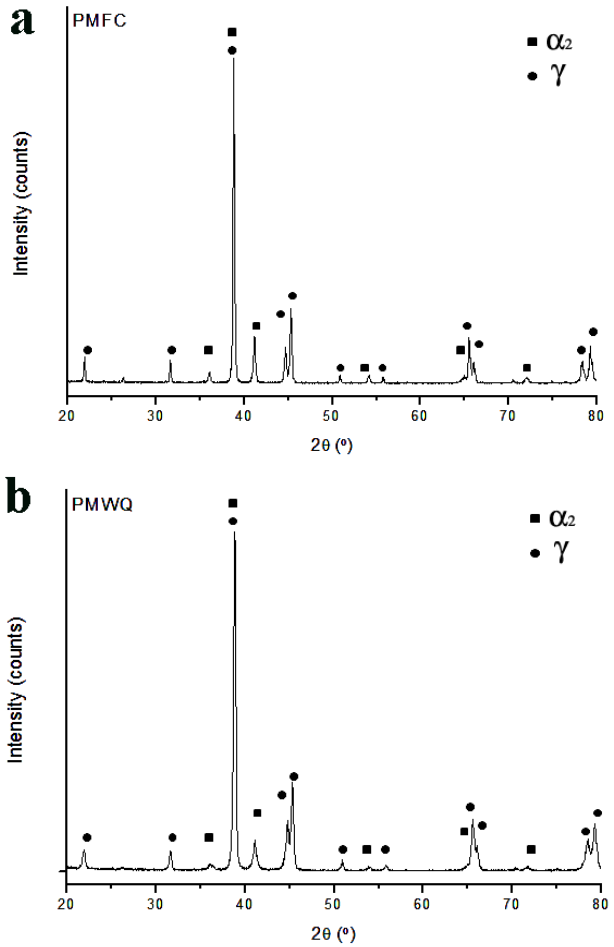

Fig. 4.18 XRD patterns corresponding to the (a) PMFC and (b) PMWQ-850-8h samples.

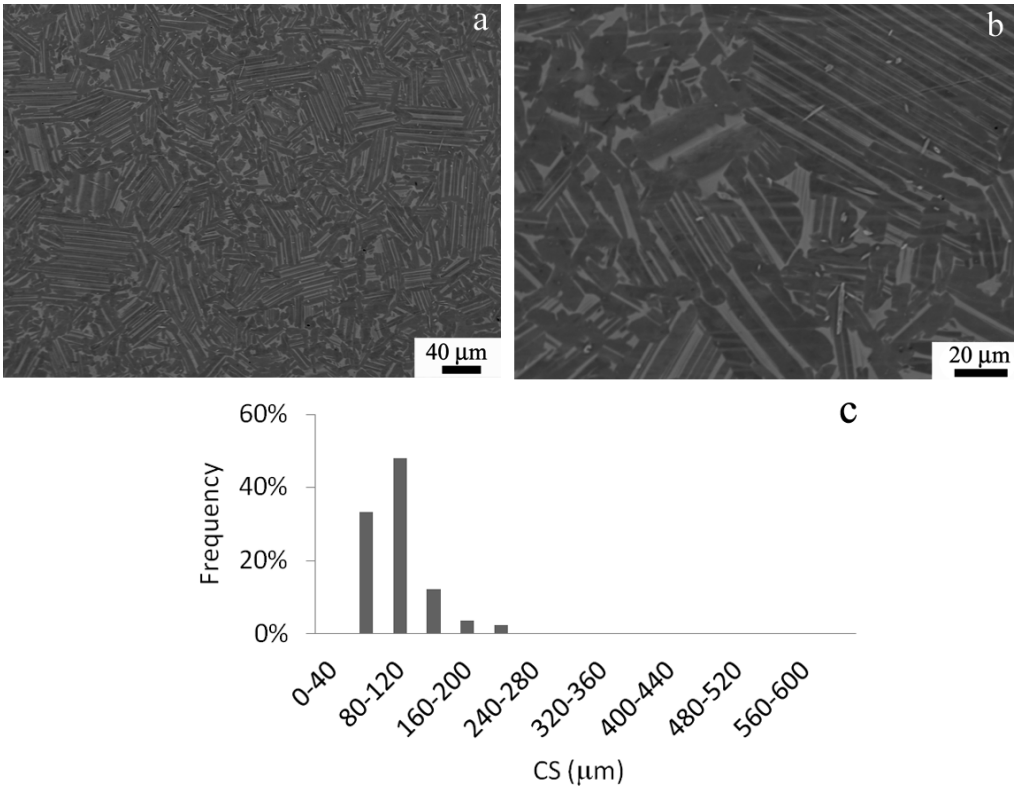

Fig. 4.19 (a, b) BSE SEM micrographs at different magnifications showing the PMFC fully lamellar microstructure; (c) colony size distribution.

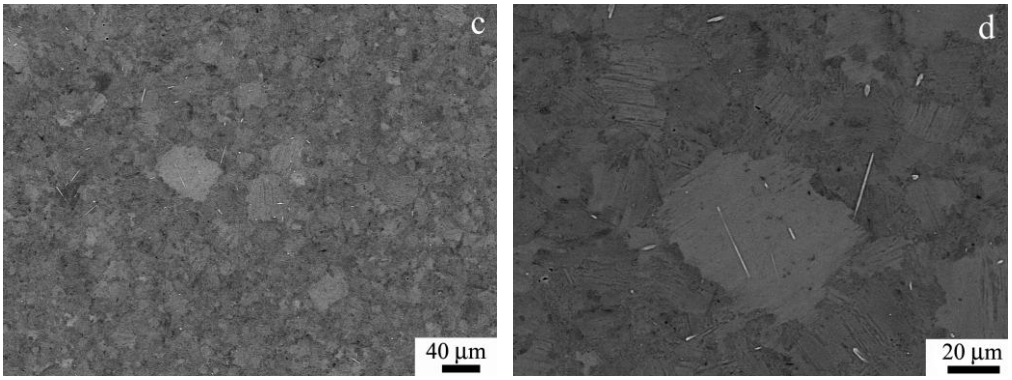

Fig. 4.20 (a, b) BSE SEM micrographs of the refined fully lamellar PMWQ (PMWQ-850-8h) microstructure.

4.1.2.4 Field assisted hot pressed material

The as-atomized prealloyed powders were also consolidated by Field Assisted Hot Pressing (FAHP) in the following conditions: 900 °C - 10 min (FAHP1) ; 1000 °C - 10 min (FAHP2); 1100 °C - 10min (FAHP3); 1250 °C - 10 min (FAHP4) and 1350 °C - 2 min (FAHP5). The XRD patterns corresponding to the different samples (Figure 4.21) show the presence α_2 and γ phases after consolidation at all the studied sintering temperatures and times. At the highest processing temperatures the α_2 and γ peaks become more intense and better defined, suggesting that the α-metastable phase is transformed into $\alpha_2+\gamma$ phases and the volume fraction of both phases increases with temperature. This is consistent with the high temperature XRD observations (Figure 4.15(b)).

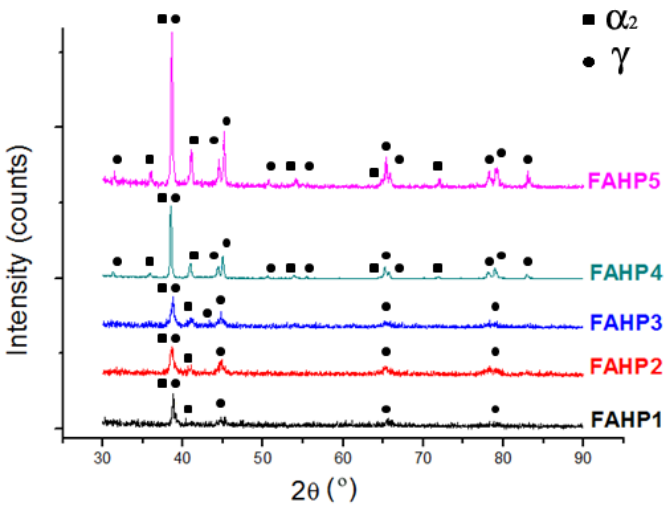

Fig. 4.21 XRD patterns corresponding to the FAHP1, FAHP2, FAHP3, FAHP4 and FAHP5 materials.

Figure 4.22 shows several BSE SEM micrographs illustrating the microstructure of the FAHP1 samples at the center (Figure 4.22(a, b)) and at the edge (Figure 4.22(c, d)) of the consolidated sample. Regardless to the location, a clear footprint of the former powder particle boundaries is present. At the center of the sample a duplex microstructure can be recognized (Figure 4.22(b)) as the metastable and heterogeneous microstructure present in the as-received powder particles starts to transform into the equilibrium phases and homogenize by diffusion at 900 °C. Moreover, Figure 4.22(b) shows the former single phase regions transformed into equilibrium lamellar colonies consisting of α_2 and γ phases. The

different lamellae orientations correspond to the former equiaxed grains orientation identified in the brighter single phase areas of the as-received powder (Figure 4.14(d)). It is well known that an increase of the processing temperature in these alloys entails the stabilization of the α regions promoting the formation of lamellar microstructures [26, 29, 70]. Therefore, in FAHP1 processing, lamellar microstructures first appear in the regions with higher concentration of α retained single phase. However, the lamellar colonies are surrounded by a high amount of equiaxed grains because the processing temperature might not be high enough to go through the eutectoid transformation into the stable α phase field.

In FAHP1 samples the densification is complete in the center, whereas a high concentration of pores is located near the edges (Figure 4.22(c)), where the temperature measured by the die's thermocouple was of 900 °C (T_{FAHP1}). This observation evidences a gradient of the temperature in the radial direction of the sample. It seems that the optimum sintering temperature is not reached in the edges since the powder densification is just starting and poor diffusion phenomena have taken place in these areas. However, the optimum densification observed in the center of the sample reveals an increase in the temperature respecting the measured T_{FAHP1}. This gradient in temperature has also been reported and modeled by other authors for similar hot consolidation processes such as spark plasma sintering [69, 70]. Figure 4.22(c) shows evidences of sintering and densification by the formation of sintering necks between particles. In particular, a close up view of these powder particle boundaries situated near the edge of the sample is shown in Figure 4.22(d). The EDX analysis taken from points A, B and C was found to be 72-75% Al, 23-25% Ti, 1-2% Nb, 1% Mn, indicating that the composition of the phase formed is close to that of Al_3Ti phase. In the field activated sintering processes the particle boundaries experience the highest temperatures due to the generation of sparks or due to the high resistance to the current path; and if sufficient time is employed mass transport takes place either by surface, grain boundary or volume diffusion. As the diffusion coefficient of Al in Ti and TiAl intermetallic is higher than that of Ti and other alloying elements [247], the elemental segregation to the particles surfaces can take place which leads to the formation of Al enriched areas. The presence of interdendritic regions in the original powder particles with high concentration of Al could also serve as a source.

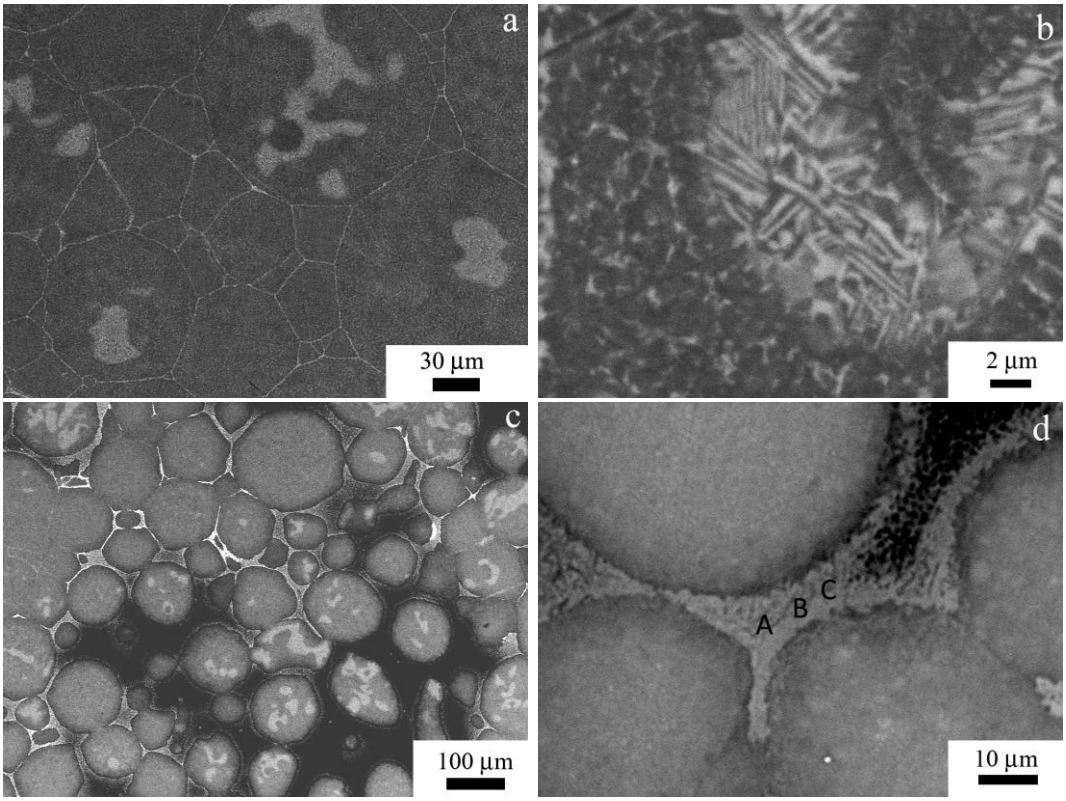

Fig. 4.22 BSE SEM micrographs showing the microstructure of the FAHP1 consolidated sample: (a, b) duplex microstructure in the center of the sample; (c) evidence of incomplete sintering at the edges of the sample; (d) Al_3Ti phase in boundary area between the powder particles (edge regions).

The gradient in density was not observed when the material was processed at 1000 °C (FAHP2). BSE SEM micrographs in Figure 4.23(a, b) show the duplex microstructure, composed by equiaxed grains and lamellar colonies throughout the sample radius. The average CS was 23 µm. No pores or elemental segregation were observed throughout the sample, suggesting that processing at and above 1000 °C allows a proper consolidation of the γ-TiAl alloy since the densification stage is well developed along the whole sample. A general view of this microstructure (Figure 4.23(a)) still evidences the former powder particles and a microstructure similar to that observed in the center of the FAHP1 sample (Figure 4.22(a)). In this condition, a gradient in the microstructure was not observed suggesting that when sintering was performed at 1000 °C the entire sample was processed in the same phase field, below the eutectoid transformation [26, 29, 70, 104]. Therefore, sintering at T>900 °C and below the eutectoid point promotes a complete densification of the material with a duplex microstructure.

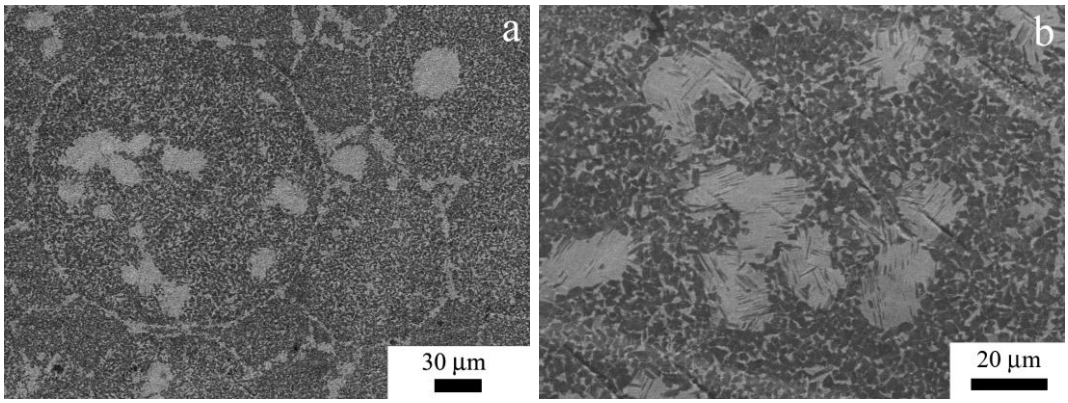

Fig. 4.23 BSE SEM micrographs showing the duplex microstructure of the FAHP2 consolidated sample. (a) Evidence of former powder particles; (b) a combination of lamellar colonies and equiaxed grains.

A nearly lamellar microstructure can be recognized at the center of the sample processed at 1100 °C (FAHP3) (Figure 4.24(a, b)). However, a radial gradient in the microstructure was again observed with a transition from nearly lamellar at the center (right in Figure 4.24(c)) to duplex at the edge (left in Figure 4.24(c)). A good distribution of the alloying elements is confirmed by EDS in these transition areas. In this case, the gradient in the microstructure along the sample's radial direction might be associated to the stability of the phases. As previously mentioned, according to this, processing at different temperatures promote the stability of different phases and finally several microstructures will be formed [26, 29, 70, 104]. Therefore, during the FAHP3 processing, the real temperature of the material in the center of the sample might be higher and above the eutectoid point since higher volume fraction of lamellar colonies and no signs of former powder particles can be observed. However, in the edge of the sample, the sintering temperature (T_{FAHP3}=1100 °C) is below the eutectoid point and a duplex microstructure is recognized as occurred with FAHP1 and FAHP2.

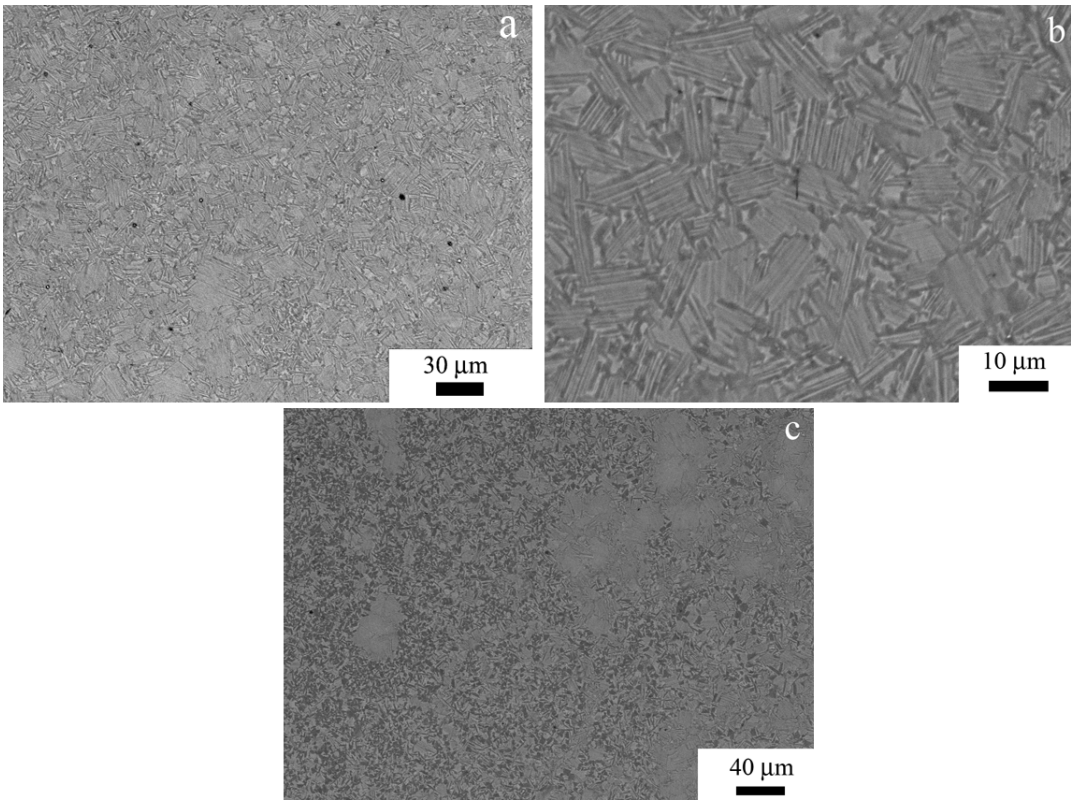

Fig. 4.24 BSE SEM micrographs showing the FAHP3 (a, b) nearly lamellar microstructure and (c) heterogeneous microstructure.

After processing the intermetallic at 1250 °C (FAHP4), a nearly lamellar microstructure was found throughout the sample (Figures 4.25(a, b)) with a refined lamellar CS of 9 μm. Since the processing temperature is above the eutectoid point on cooling, $\alpha_2+\gamma$ phases will precipitate from $\alpha+\gamma$ phases following the equilibrium phase diagram and forming nearly lamellar microstructures [26, 29, 70, 104]. Finally, processing at 1350 °C (FAHP5), fully lamellar microstructures were obtained (Figures 4.25(c, d)) with a coarser lamellar CS of 27 μm. This observation confirms that processing at temperatures above the α-transus leads to microstructures completely composed by lamellar colonies and that increasing processing temperatures also leads to a growth in the CS. Nevertheless, as it has been observed in all the processed samples, the average lamellar CS reached, thanks to the short time at temperature and the fast cooling rate provided by FAHP, is significantly lower than that obtained by conventional casting [248]. In addition, brighter areas are found within the lamellar structure. These brighter areas, associated to heavier elements, might be related to a possible retained β-phase [249]. However, not significant predominance of β-phase is recognized as it is not identified in the corresponding XRD pattern (Figure 4.21).

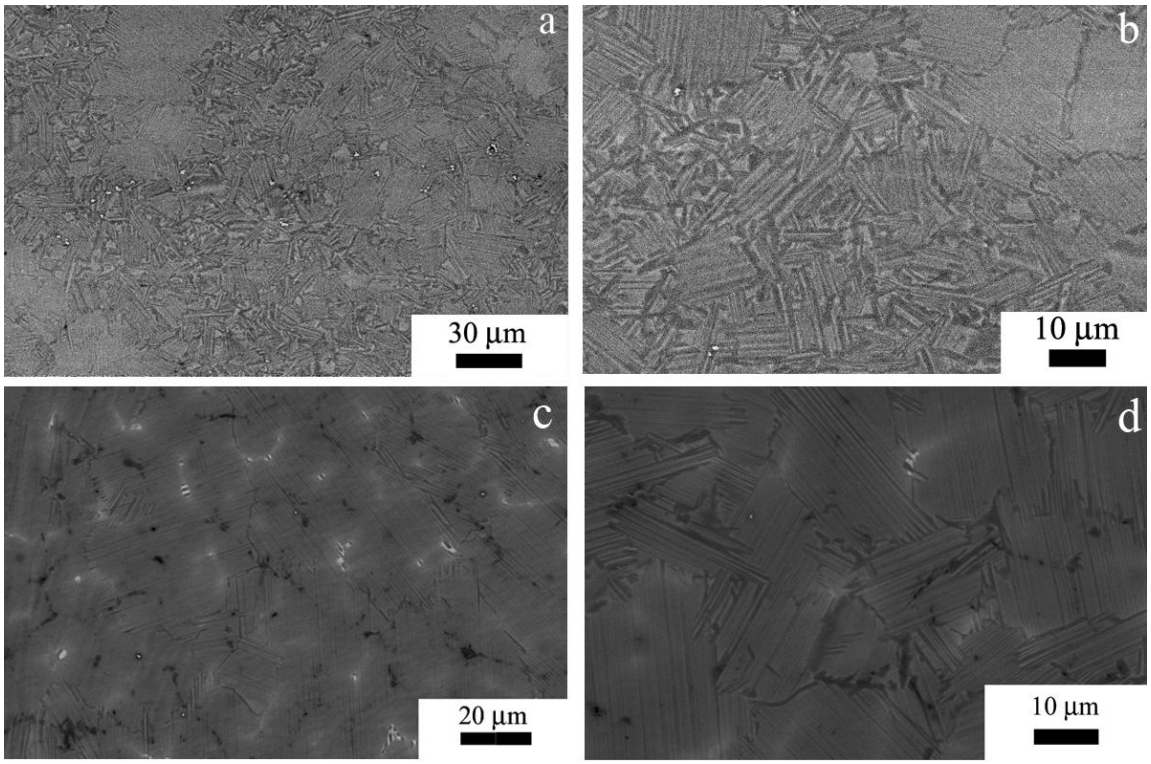

Fig. 4.25 BSE SEM micrographs showing the microstructure of the (a, b) FAHP4 nearly lamellar microstructure; (c, d) FAHP5 fully lamellar microstructure.

4.1.3 Microstructures selected for *in situ* mechanical testing

The materials selected for high temperature *in situ* mechanical testing were CC-LPT, CC, CCFC, and PMFC as they possess widely varying microstructures, which are expected to result in marked differences in the mechanical behavior [7]. In particular, as described in the following chapters, the deformation and fracture mechanisms will be investigated in these materials. Table 4.3 summarizes the main microstructural parameters of the selected materials.

Table 4.3 Microstructure type, colony size and lamellar spacing values for the CC-LPT, CC, CCFC and PMFC materials.

	CC-LPT	**CC**	**CCFC**	**PMFC**
Microstructure	NL	NL	FL	Duplex
Average colony size (CS) (μm)	194±121	125±53	183±83	98±34
Colony size (CS) range (μm)	[52-636]	[39-252]	[80-463]	[45-205]
Average grain size (μm)	-	-	-	4.4±2.6
Grain size range (μm)	-	-	-	[0.6-11.4]
λ_γ (nm)	319±339	465±270	210±140	-
λ_γ range (nm)	[47-1245]	[51-1259]	[35-471]	-
$\lambda_{\alpha 2}$ (nm)	287±133	286±288	160±160	-
$\lambda_{\alpha 2}$ range (nm)	[85-603]	[30-1259]	[13-578]	-

For comparison, Table 4.4 reviews the microstructural parameters for similar alloys and processing techniques.

.

Table 4.4 Review of microstructural parameters for γ-TiAl alloys (CR: cooling rate; Ag: Aging)

Alloy	Processing	Heat Treatment	Type	CS (μm)	λγ(nm)	λα(nm)	λ (nm)	Reference
Ti-45Al-2Nb-2Mn-0.8vol.%TiB_2	Cast+HIP	-	NL	<100	480	173	-	248
Ti-47Al-2Nb-2Mn-0.8vol.%TiB_2	Cast+HIP	-	NL	>100	420	176	-	248
Ti-46Al-2Cr-2Mo-0.25Si-0.3B	Cast	-	NL	120	-	-	150-250	250
Ti-45Al-2Nb-2Mn-0.8vol.%TiB_2	Cast+HIP	1010 °C,50h, AC	NL	20-100	-	-	400	134
Ti-45Al-2Nb-2Mn-0.8vol.%TiB_2	Cast+HIP	1350 °C, 2h, FC	FL	50-100	1011	357	-	248
Ti-45Al-2Nb-2Mn-0.8vol.%TiB_2	Cast+HIP	1350 °C, 2h, AC	FL	25-100	198	94	-	248
Ti-45Al-2Nb-2Mn-0.8vol.%TiB_2	Cast+HIP	1350 °C, 2h, OQ	FL	10-50	62	53	-	248
Ti-45Al-2Nb-2Mn-0.8vol.%TiB_2	Cast+HIP	1350 °C, 2h,OQ+Ag	FL	10-50	-	-	55	134
Ti-45Al-2Nb-2Mn-0.8vol.%TiB_2	Cast+HIP	1350 °C, 0.5h,AC+Ag	FL	20-100	-	-	100	134
Ti-45Al-2Nb-2Mn-0.8vol.%TiB_2	Cast+HIP	$T>T_\alpha$, FC	FL	65	-	-	800	254
Ti-46Al-1.9Cr-3Nb	Cast	$T>T_\alpha$, FC	FL	68±45	-	-	-	252
Ti-46Al-1.9Cr-3Nb	Cast	$T>T_\alpha$, CR=20 °C/min	FL	145±95	-	-	-	252
Ti-45.5Al-2Cr-1.5Nb-1V	Cast+HIP	$T>T_\alpha$, FC	FL	390	-	-	160	253
Ti-45.5Al-2Cr-1.5Nb-1V	Cast+HIP	$T>T_\alpha$, AC	FL	360	-	-	95	253
Ti-46Al-9Nb	PM-HIP	$T>T_\alpha$, CR=20 °C/min	FL	280-330	-	-	170	250

4.1.3.1 As-cast microstructures (CC-LPT and CC)

Table 4.4 shows that other research works also obtained nearly lamellar microstructures for the Ti4522XD or similar alloys processed by casting and followed by HIP [28, 248, 250, 251], as in CC-LPT and CC materials. It is important to mention that the CC-LPT was heat treated at temperatures below the eutectoid point ($T_{annealing}$=1080 °C, $T_{eutectoid}$=1150 °C) during 8 h following the HIP process. Zhu *et al*. [134] also annealed the same alloy under similar conditions and confirmed the development of a nearly lamellar microstructure. Both studies confirm that heat treating below the eutectoid point helps on the microstructural stabilization, although it does not lead to any significant microstructural change.

As-cast materials in the form of LPT blades had a coarser average CS (194 μm) than that observed for CC rectangular specimens (125 μm). The CC-LPT CS values were very dispersed, ranging from 52 μm to 636 μm. In contrast, CC samples showed a narrower CS distribution, ranging from 39 μm to 52 μm. The larger CS of the CC-LPT samples could be due to the colony growth during the post HIP annealing. The difference in CS distribution between the CC-LPT and CC specimens might be attributed to the presence of more pronounced temperature gradients in the complex shaped blades. As Table 4.4 shows, Seo *et al*.[248] measured lamellar CS averages higher than 100 μm for an as-cast Ti4522XD alloy, while Clemens *et al*.[250] obtained a value of 120 μm for an as-cast Ti-46Al-2Cr-2Mo-0.25Si-0.3B alloy. Therefore, the CC-LPT average CS is above the reported ones, while the CC average CS is comparable. Novoselova *et al*.[252] have reported a wide dispersion of the CS values (68±45 μm and 145±95 μm) for a heat treated as-cast Ti-46Al-1.9Cr-3Nb alloy. This is consistent with the wide dispersion observed in the present research work.

The average lamellar spacing of the as-cast intermetallic, CC-LPT (λ_γ=465 nm; $\lambda_{\alpha 2}$ =287 nm) and CC (λ_γ=319 nm; $\lambda_{\alpha 2}$ =287 nm), are of the order of those reported for cast Ti4522XD intermetallic (λ_γ=480nm; $\lambda_{\alpha 2}$ =173nm) studied by Seo *et al*. [248] It is also remarkably that in both phases the lamellar spacing distributions were very wide, with standard deviations close to the average values, as has been previously reported by Cao *et al*.[253] for fully lamellar TiAl alloys**.**

4.1.3.2 Cast and heat treated microstructures (CCFC)

The CCFC material of the present research, which was heat treated at 1300 °C during 2 hours and cooled in the furnace, exhibited a fully lamellar microstructure. This is consistent with previous studies, which confirm that. As-cast TiAl alloys are usually heat treated above

the α-solvus to generate fully lamellar microstructures [7, 26, 134, 248, 252-254]. Seo *et al*. [248] observed in the Ti4522XD alloy that decreasing cooling rates promoted the definition of interlocked boundaries.

The CCFC material has an average CS of 181 μm. Average CS values for Ti4522XD alloys heat treated above the α-solvus are reported to range from 50-100 μm [134, 248]. In non-reinforced alloys, such as Ti-45.5Al-2Cr-1.5Nb-1V, the average CS values are much higher, about 360-390 μm [253]. Therefore, the values measured in the CCFC material confirm the role of borides in colonies refinement.

The CCFC lamellae spacing values, λ_γ=210 nm; $\lambda_{\alpha 2}$ =160 nm, are finer than those reported by Seo *et al*. [248] for the same alloy that was investment cast, annealed and cooled in the furnace (λ_γ=1011 nm; $\lambda_{\alpha 2}$ =357 nm).

4.1.3.3 HIP and heat treated microstructures (PMFC)

Consistent with the current understanding of TiAl transformation mechanisms, the as-HIPed PM material developed a near gamma microstructure because consolidation started from the α metastable powder and was carried out by HIP at 1200 °C. The near gamma microstructure and the considerable refinement of the microstructure developed is consistent with previous works on similar alloys [67, 96, 97]. Following a heat treatment at 1300 °C during 2 hours and furnace cooling, a duplex microstructure is obtained in the PMFC material. The absence of a fully lamellar microstructure maybe attributed to the heterogeneous microstructure of the as-HIPed consolidated sample. The average CS (98 μm) of the PMFC material is comparable to that obtained by Yang *et al*. [67] (99 μm) for an as-HIP Ti4522XD alloy.

4.2 *In situ* analysis of the deformation and fracture mechanisms

4.2.1 Fracture following constant strain rate tensile straining

The fracture mechanisms at both room and high temperature during constant strain rate tests (10^{-3} s^{-1}) were characterized in as centrifugally cast (CC-LPT and CC) nearly lamellar microstructures. The preferential sites for crack nucleation and propagation were analyzed *in situ*. The main findings of this study are summarized below.

4.2.1.1 Room temperature

Analyzing the deformation and fracture mechanisms of γ-TiAl alloys at room temperature by *in situ* testing proved very difficult due to the inherent brittleness of these materials. Nevertheless, the CC-LPT samples were tested at RT and 10^{-3} s^{-1} and the observed behavior is briefly reported below. Figure 4.26 confirms that the material was brittle at this temperature and that the sample fractured at 480 MPa without any measurable plastic strain. No significant changes were observed in the local microstructural patch observed during the *in situ* tests, and fracture occurred suddenly in a location outside that observed during the *in situ* imaging. This behavior is consistent with previous *in situ* observations of a similar FL TiAl intermetallic where the primary crack grew too rapidly to be observed [232]. Thus, the nucleation and growth of damage during RT tensile deformation was not characterized in this study. The post-mortem fracture observations of representative RT tensile samples showed translamellar and interlamellar cracking (Figure 4.27(a, b)) and cleavage fracture (Figure 4.27(c)).

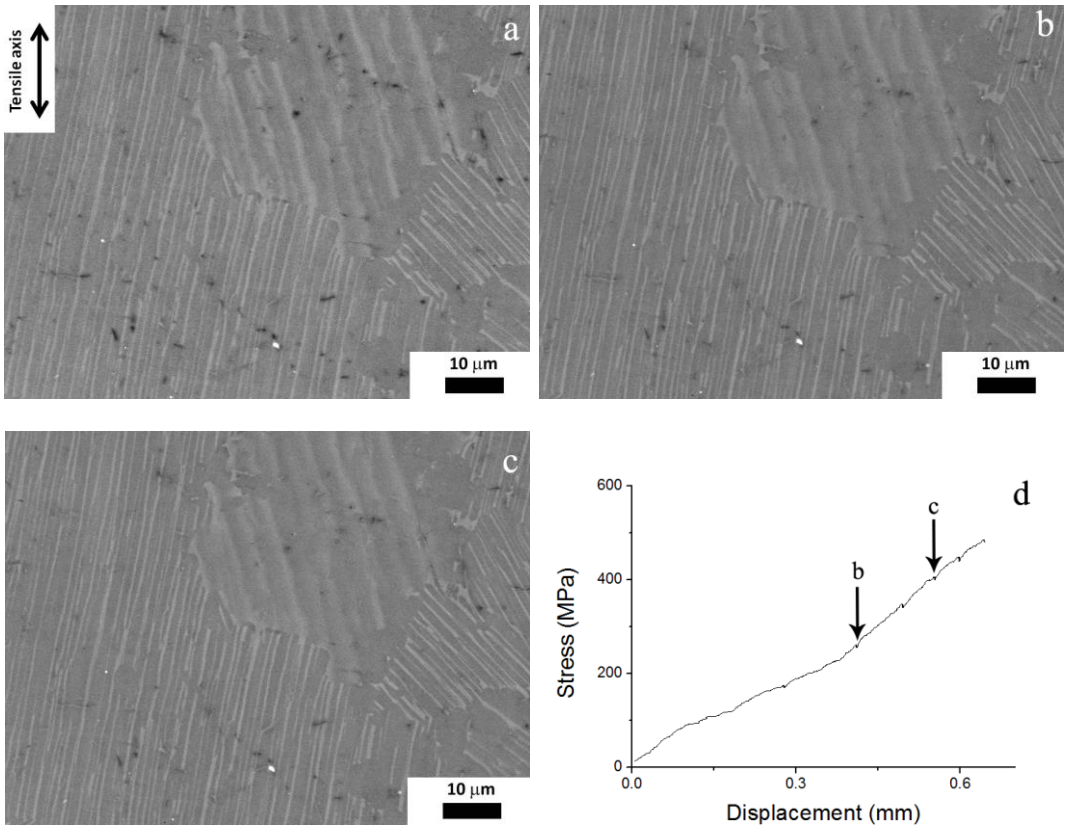

Fig. 4.26 Sequence of BSE SEM micrographs acquired in the same CC-LPT sample area during *in situ* tensile test at RT: (a) σ = 0MPa, (b) σ =260 MPa, Δl=0.4 mm and (c) σ =450 MPa, Δl=0.6mm showing no microstructural changes. (d) Stress-displacement curve of the CC-LPT material tested at RT under constant strain rate $\dot{\varepsilon}=10^{-3}s^{-1}$.

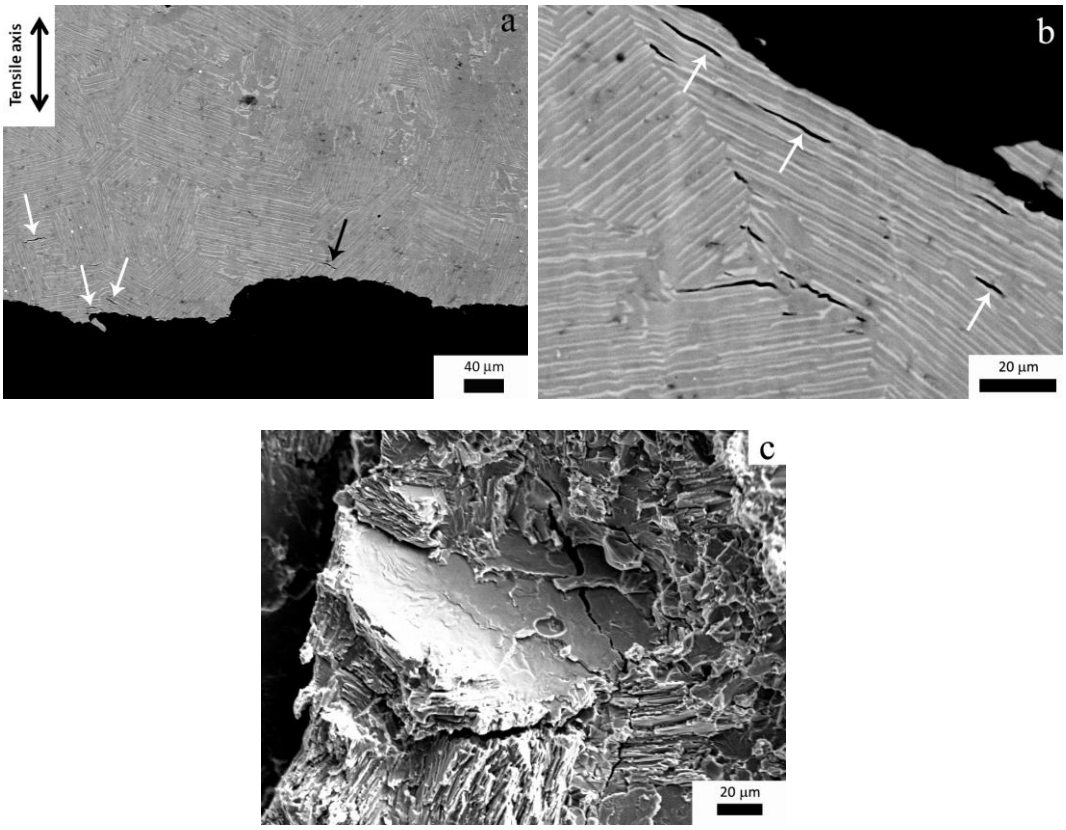

Fig. 4.27 (a, b) BSE SEM micrograph of the CC-LPT RT tensile deformed microstructure illustrating translamellar (black arrow) and interlamellar cracking (white arrows) below the fracture surface; (b) SE SEM micrograph of the fracture surface of a sample tested at RT illustrating brittle features including cleavage.

If each colony is assumed to behave as a monocrystal, such as PST materials, the deformation behavior would be dependent on the orientation of the lamellae with respect to the loading axis [43, 129, 148]. Brittle behavior is typical, along with high strength and low elongation-to-failure, for lamellar orientations of 0 ° or 90 ° with respect to the loading axis. Such conditions result in extremely low ε_f values due to atomic plane separation (perpendicular case) or translamellar fracture (parallel case). If the lamellae are oriented at 45 ° with respect to the loading direction, the strength is lower and the material presents a higher elongation-to-failure. For this so-called soft mode, the deformation will take place by dislocation slip due to the presence of a shear component of the applied stress along the interlamellar boundaries and the dominant fracture mode is interlamellar. Polycrystalline microstructures, containing randomly oriented lamellae, are expected to exhibit a mixed fracture mode composed of interlamellar and translamellar cracking together with decohesion at the colony boundaries [7, 256].

Lu *et al.* [152] used RT manual loading conditions to perform an *in situ* observation of a Ti-49Al FL polycrystalline microstructure. Their results indicated that when the lamellae within

a colony were oriented at a large angle (about 70 °) from the tensile axis, the main crack propagated through linking with interlamellar microcracks by shearing or tearing. When the lamella within a colony were nearly parallel to the loading direction, the main crack propagated in a translamellar fashion linking with the two types of microcracks, which were interlamellar and translamellar. When the main cracks propagated along the colony boundaries, the microcracks usually formed in interlamellar or translamellar directions in neighboring grains, depending on the orientation of the lamellae with respect to the main crack. When the main crack encountered a nearly transverse colony boundary, intercolony fracture occurred. Their results are similar to those observed in this study as interlamellar and translamellar cracking were found during the *in situ* RT tensile experiments.

4.2.1.2 High temperature

Analyzing fracture mechanisms during elevated-temperature *in situ* tensile tests was feasible, as the sample exhibited a greater elongation-to-failure (ε_f) than at RT. Figure 4.28 illustrates the microstructural evolution of the CC-LPT sample during *in situ* tensile testing at 700 °C and 10^{-3} s^{-1}. The maximum tensile strength (σ_{max}=520 MPa) was consistent with that reported by Mirshams *et al*. [257] and was greater than the RT strength, as a result of the higher ε_f and of the intermetallic's relative insensitivity to temperature up to T=700 °C. Two different types of cracks were observed depending on their location. Only interlamellar cracks were found at the center of the sample (Figure 4.28 and Figure 4.29(a)). They were developed at tensile stresses above 390 MPa and, thus, interlamellar cracking seems to be activated in this material above a threshold stress (>0.75$\sigma_{\max}$) at T=700 °C. This is an important observation as it suggests that the interface strength between the lamellae is greater than 390 MPa. It is expected that this value will be dependent on the microstructure, and the current value may be specific of this manufactured LPT blade's microstructure. The B-rich phase was also voids susceptible to cracking (Figure 4.29(b)). In addition to interlamellar cracks, cracks perpendicular to the tensile axis grew in the sample edges (Figure 4.29(c)). They were assisted by the stress concentrations at the edges and propagated through the lamella and colonies (Figure 4.29(d)). The fracture surfaces revealed ductile dimples and brittle cleavage (Figure 4.30).

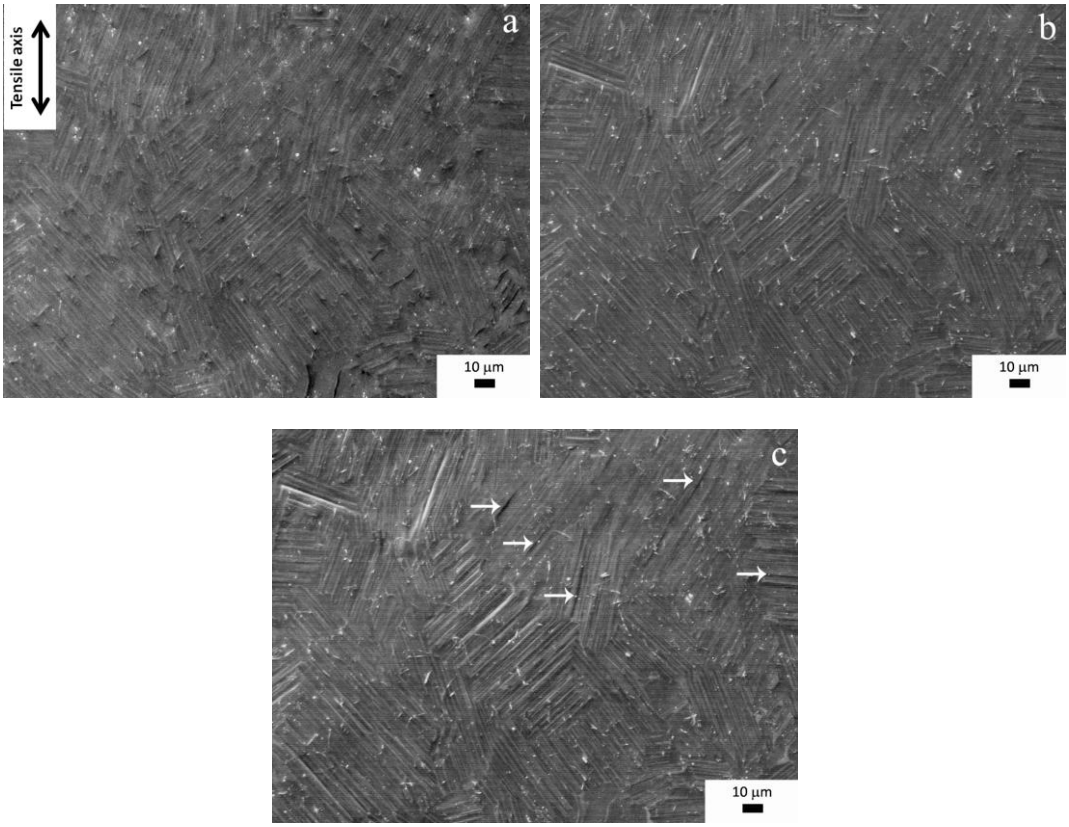

Fig. 4.28 Sequence of SE SEM micrographs acquired in the CC-LPT same sample area during *in situ* tensile test at 700 °C: (a) σ =0 MPa, (b) σ =413MPa, ε~0.2% and (c) σ =481MPa, ε~0.3%. The onset of interlamellar cracking is evident in (c).

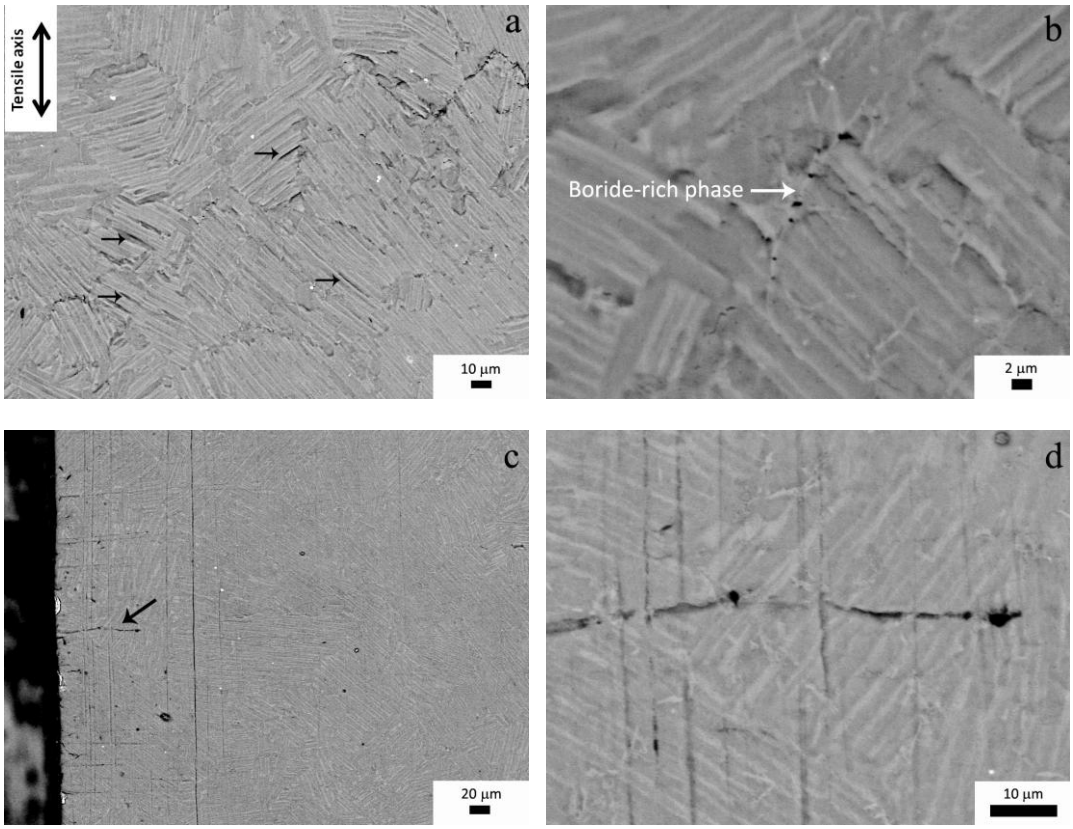

Fig. 4.29 SE SEM micrographs obtained during *in situ* tensile test at 700 °C at σ = 390 MPa and ε~0.2%. (a) Onset of interlamellar cracking in the center of the sample; (b) multiple fracture of boride-rich phase; (c, d) cracks perpendicular to the vertical loading axis emanating from the edge. (d) Higher magnification image of the area in (c) showing that the cracks propagated through the lamella and colonies. Note that the vertical lines in (c) and (d) were polishing artifacts present before loading.

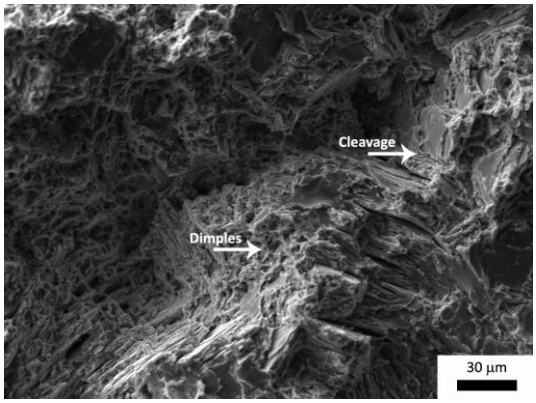

Fig 4.30 SE SEM micrograph of the CC-LPT fracture surface after tensile testing at 700 °C. Both ductile (dimples) and brittle (cleavage) features can be observed.

The as-centrifugally cast CC nearly lamellar microstructures exhibited a similar fracture behavior to that reported above for CC-LPT samples. Figure 4.31 depicts the SE SEM micrographs obtained at various stress levels during the constant strain rate test (10^{-3} s^{-1}) of CC samples at 700 °C. The maximum stress borne by the material, σ_{max}, was 460 MPa. Lacey borides were observed to crack at intermediate strains close to the yield stress (see black arrows in Figure 4.31(b)). Ledges at colony boundaries were detected at higher strains (dashed arrows in Figure 4.31(c, d)).The micrographs show that interlamellar ledges (highlighted in Figure 4.31 using white arrows) became more pronounced with deformation. Interlamellar ledges were first observed at a stress of 374 MPa (Figure 4.31(b)). Such ledges have not been reported before and their origin is still unknown.

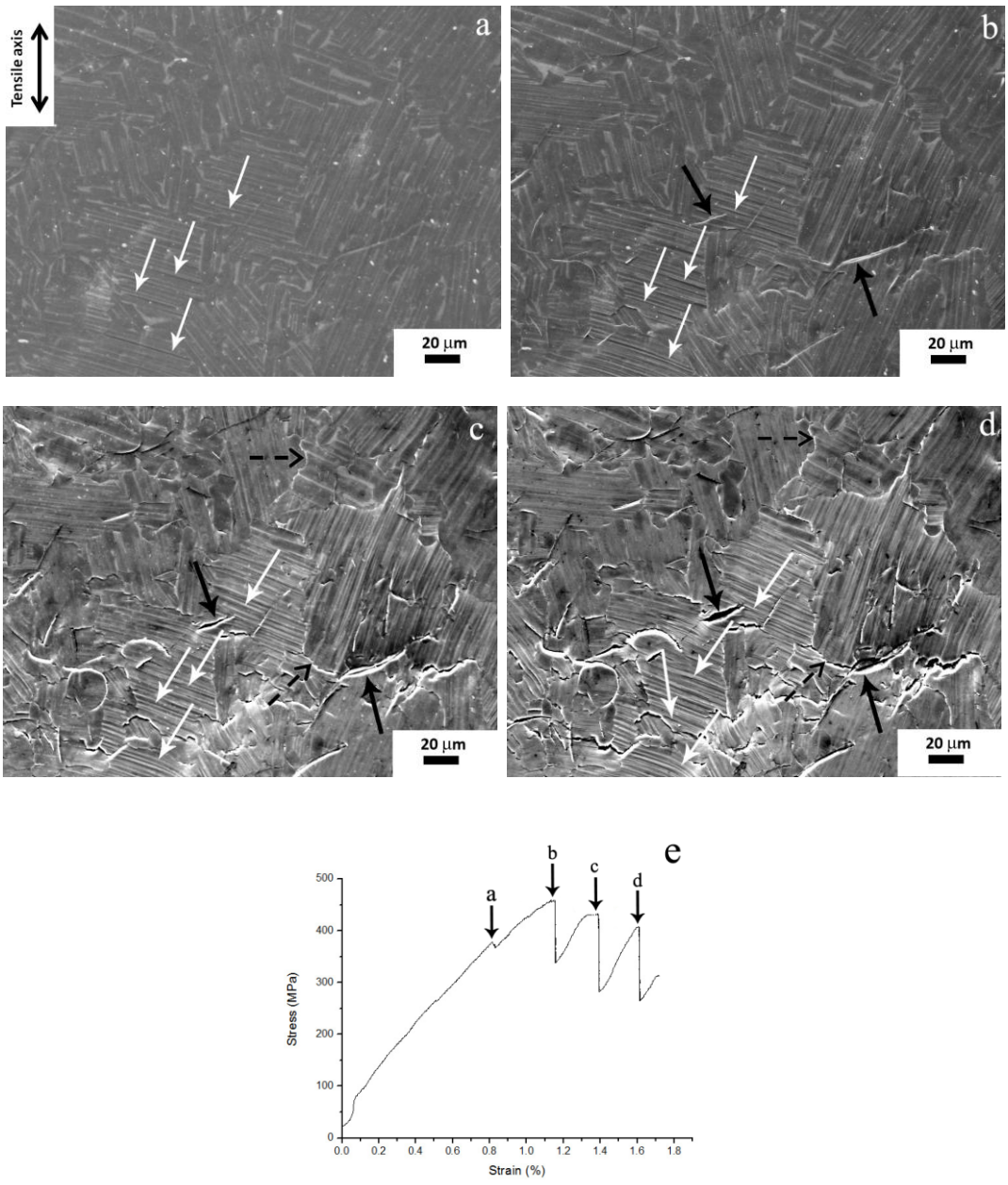

Fig. 4.31 Sequence of SE SEM micrographs obtained during *in situ* tensile test at 700 °C: (a) σ = 374 MPa, ε~0.8%; (b) σ = 459 MPa, ε~1.2%; (c) σ = 433 MPa, ε~1.4 %; (d) σ = 408 MPa, ε~1.6 %. White arrows point toward interlamellar relief, black arrows highlight reinforcement cracks and dashed arrows show the initiation of intercolony cracks. (e) Stress - strain curve corresponding to the tensile test with indications where micrographs (a-d) were taken.

4.2.2 Fracture following constant stress (creep) deformation

Creep tests were carried out in the CC-LPT samples at 250 MPa, which stands for $0.48\sigma_{max}$ at 700 °C. The creep behavior presented the three typical stages (Figure 4.32). However, the length of the secondary creep regime was not well defined as the creep rates increased slightly and continued to increase throughout the remainder of the experiment shortly after achieving the minimum creep rate. Low-magnification SEM micrographs obtained during each one of the three stages of creep are shown in Figure 4.33. Unlike the high temperature tensile tests at constant strain rate (section 4.2.1.2), colony boundaries were the primary sites for crack nucleation and propagation. During the secondary creep regime and continuing into the tertiary creep regime, surface relief was increasingly evident suggesting that the colony boundaries were deforming through boundary sliding leading to intercolony cracking. Cracking initiated at colony boundaries in the center of the gage section and propagated along the colony boundaries (Figure 4.34). Edge cracks were also observed during the experiment, and such cracks also propagated along colony boundaries (Figure 4.35). Ductile dimples were dominant in the fracture surface, although zones broken by cleavage were also found (Figure 4.36).

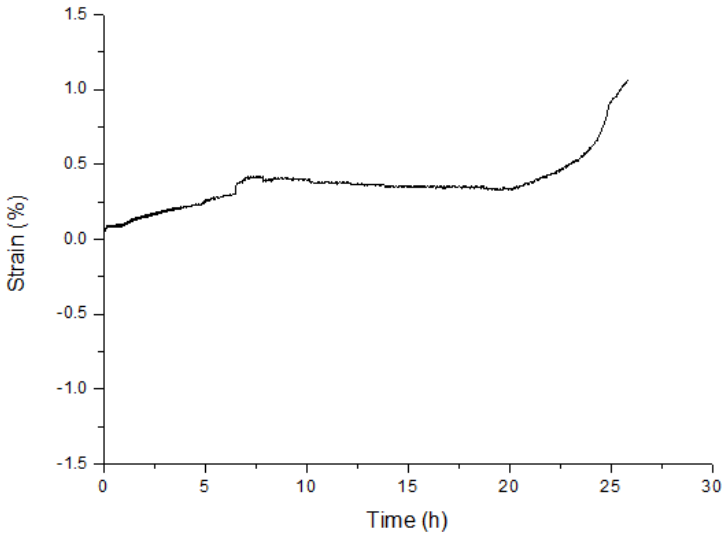

Fig. 4.32 CC-LPT strain versus time creep curve at 250 MPa and 700 °C

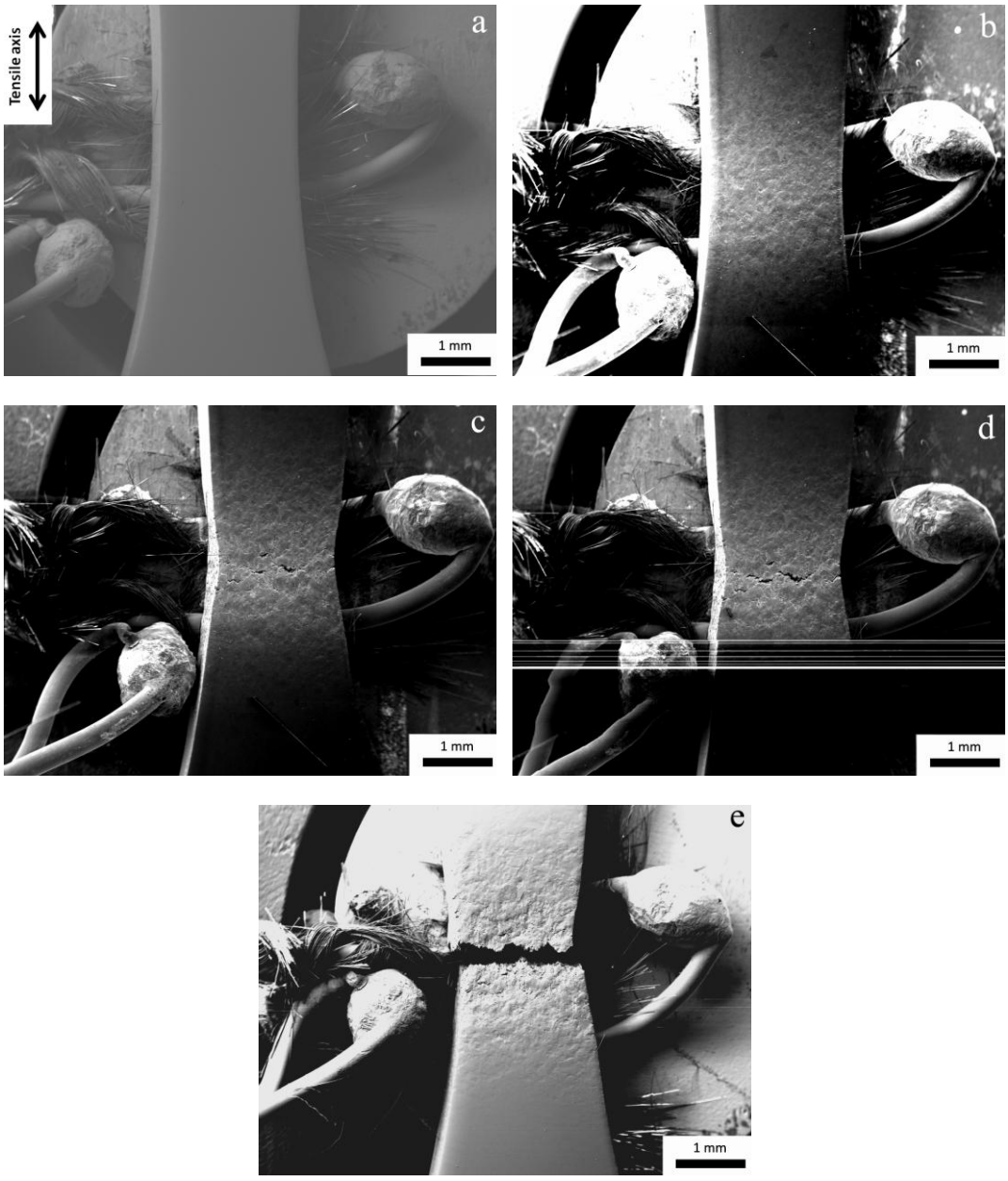

Fig. 4.33 Sequence of low magnification SE SEM micrographs obtained during the creep experiment. (a) 0 hours; (b) secondary creep stage, 18.8 hours, ε~0.3%; (c) tertiary creep stage, 23.8 hours, ε~0.6%; (d) tertiary creep stage just prior to fracture, 25.9 hours, ε~1.0%; (e) after fracture.

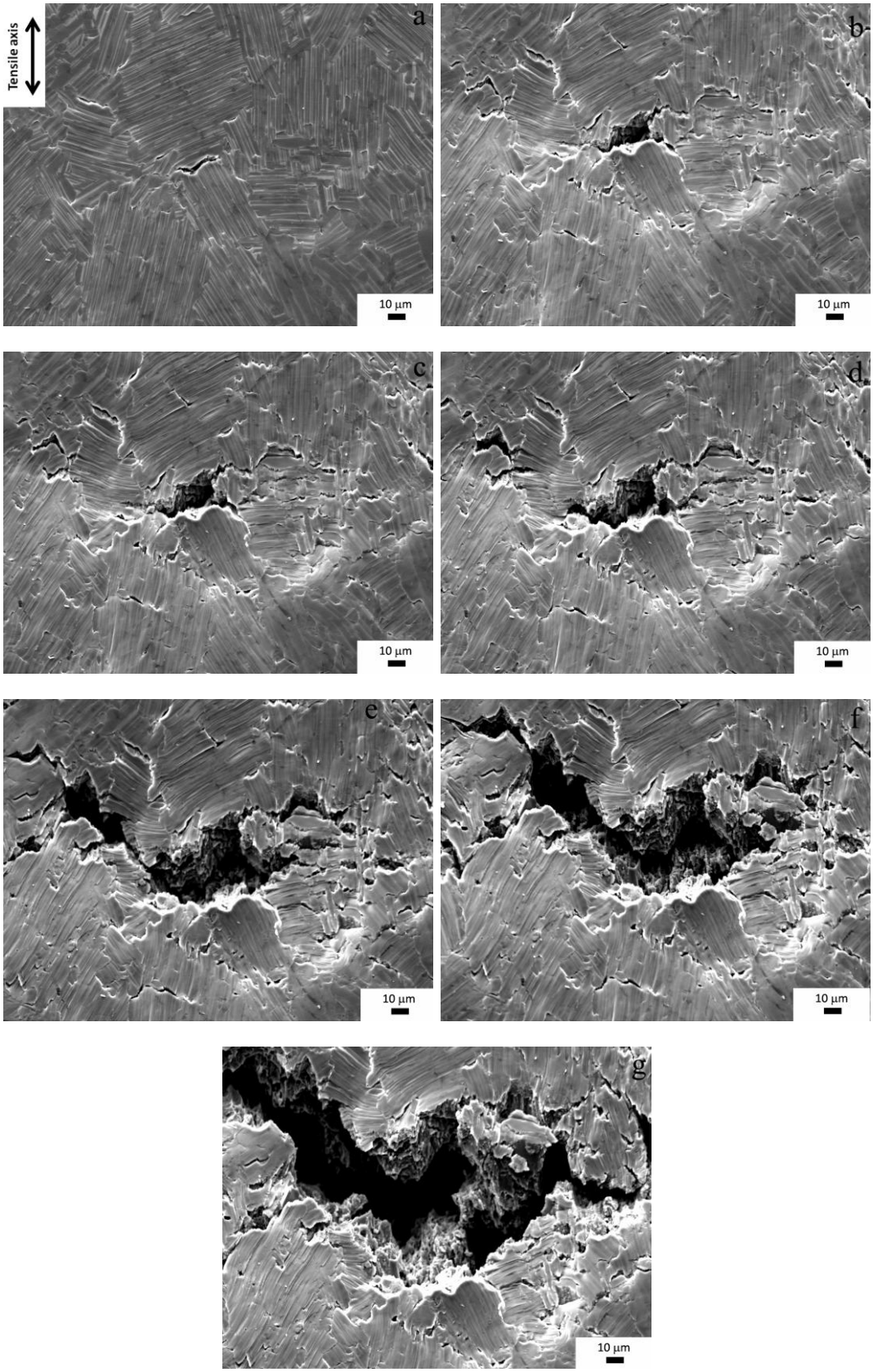

Fig. 4.34 Sequence of SE SEM micrographs illustrating the nucleation and growth of the primary crack which led to fracture in the creep test. (a) secondary creep stage, 7.63 hours, ε~ 0.2%; (b) secondary creep stage, 22.1 hours, ε~0.3%; (c) secondary creep stage, 22.4 hours ε~0.4%; (d) tertiary creep stage 22.8 hours ε~0.5%; (e) tertiary creep stage, 23.1 hours ε~0.6%; (f) tertiary creep stage, 23.4 hours ε~0.6%; (g) tertiary creep stage just prior to fracture, 25.9 hours, ε~1.0%. Note that the crack initiated and grew along colony boundaries.

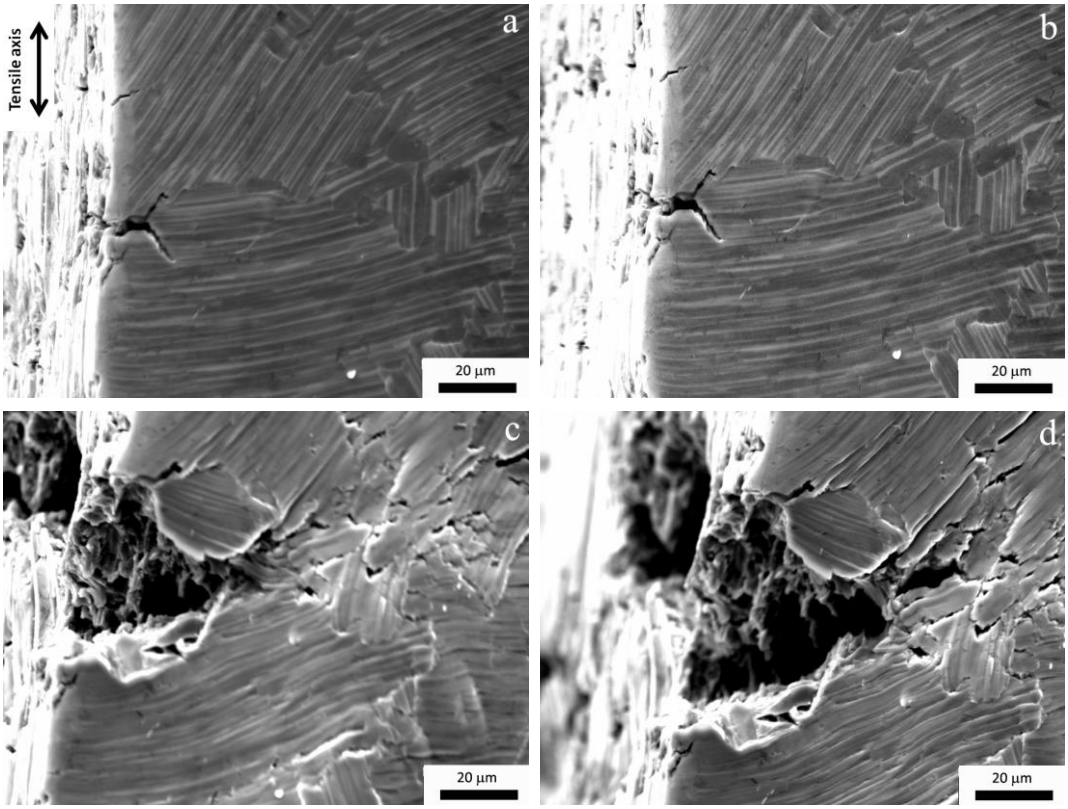

Fig. 4.35 Sequence of SE SEM micrographs illustrating the nucleation and growth of a secondary edge crack during creep. (a) secondary creep stage, 5.9 hours, ε~0.2%; (b) secondary creep stage, 6.6 hours, ε~ 0.4%; (c) secondary creep stage, 22.4 hours ε~0.4%; (d) tertiary creep stage, 22.7 hours ε~0.5%;. Note that the crack tended to propagate along a colony boundary.

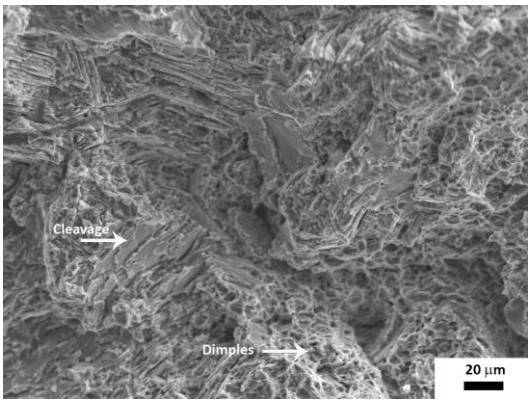

Fig. 4.36 SE SEM micrograph of the fracture surface after the creep test. Ductile dimples are dominant although brittle cleavage features are also present.

During the tensile creep experiments, no or limited interlamellar cracking was observed. This is consistent with the fact that the creep applied stress, σ =250 MPa, was significantly lower than 390 MPa, the stress at which interlamellar cracks were observed in these materials (section 4.2.1.2). Thus, interlamellar cracking appears to be the dominant cracking mechanism when the stresses are high (>0.75σ_{max}) (374 MPa and 390 MPa in CC-LPT and CC materials, respectively) while interlamellar cracking is inhibited during diffusion-assisted deformation at elevated temperature under relative low stresses (<0.50σ_{max}). Under these latter conditions, intercolony cracking controls the onset of damage as the diffusion rates across the colony boundaries are expected to assist the deformation at such locations. This can lead to local deformation at colony boundaries and thus explain the enhanced colony boundary deformation in the form of relief and sliding. It has been proposed that sliding occurs by the glide and climb of dislocations in grain boundary zones [258]. The stress concentration caused by grain-boundary dislocation pileup can be relieved by activating grain-boundary dislocation sources or by nucleating and propagating an intergranular crack. Thus, cracking can serve as an accommodation mechanism for grain boundary sliding. The *in situ* observations were useful in confirming both the crack propagation along the colony boundaries as well as the minimum stress level necessary to initiate interlamellar cracking.

In order to investigate further the effect of the applied stress on the incidence of colony boundary cracking, the CC samples were tested at constant stresses ranging from 300 MPa (0.65σ_{max}) to 450 MPa (0.98σ_{max}). The microstructural evolution during the creep tests at 300 MPa (0.65σmax) and 400 MPa (0.86σmax) was similar. The secondary creep stage strain rates at these conditions were approximately $5\cdot10^{-8}$ s^{-1} and $5\cdot10^{-7}$ s^{-1}, respectively. Figure 4.37 shows several SEM micrographs taken at various strain levels of the tensile-creep test performed at 300 MPa. During the secondary-creep regime, surface relief at the colony boundaries was increasingly evident, suggesting the presence of colony boundary sliding. Crack nucleation and propagation at the colony boundaries was observed during the secondary regime (Figure 4.38(a)) (at strains of above 0.5%) and continued into the tertiary creep regime (Fig. 4.37(b-d) and 4.38(b)). Lacey borides were susceptible to brittle fracture at even lower strains (Figure 4.38). The primary crack path followed colony boundaries, as shown in Figure 4.37 (c-e). For a specimen tested at 400 MPa, crack nucleation at the colony boundary was first detected at a strain of 0.6 %, and B-rich phase particles were observed to crack (Figure 4.39) after 0.2% strain. No interlamellar ledge formation was observed.

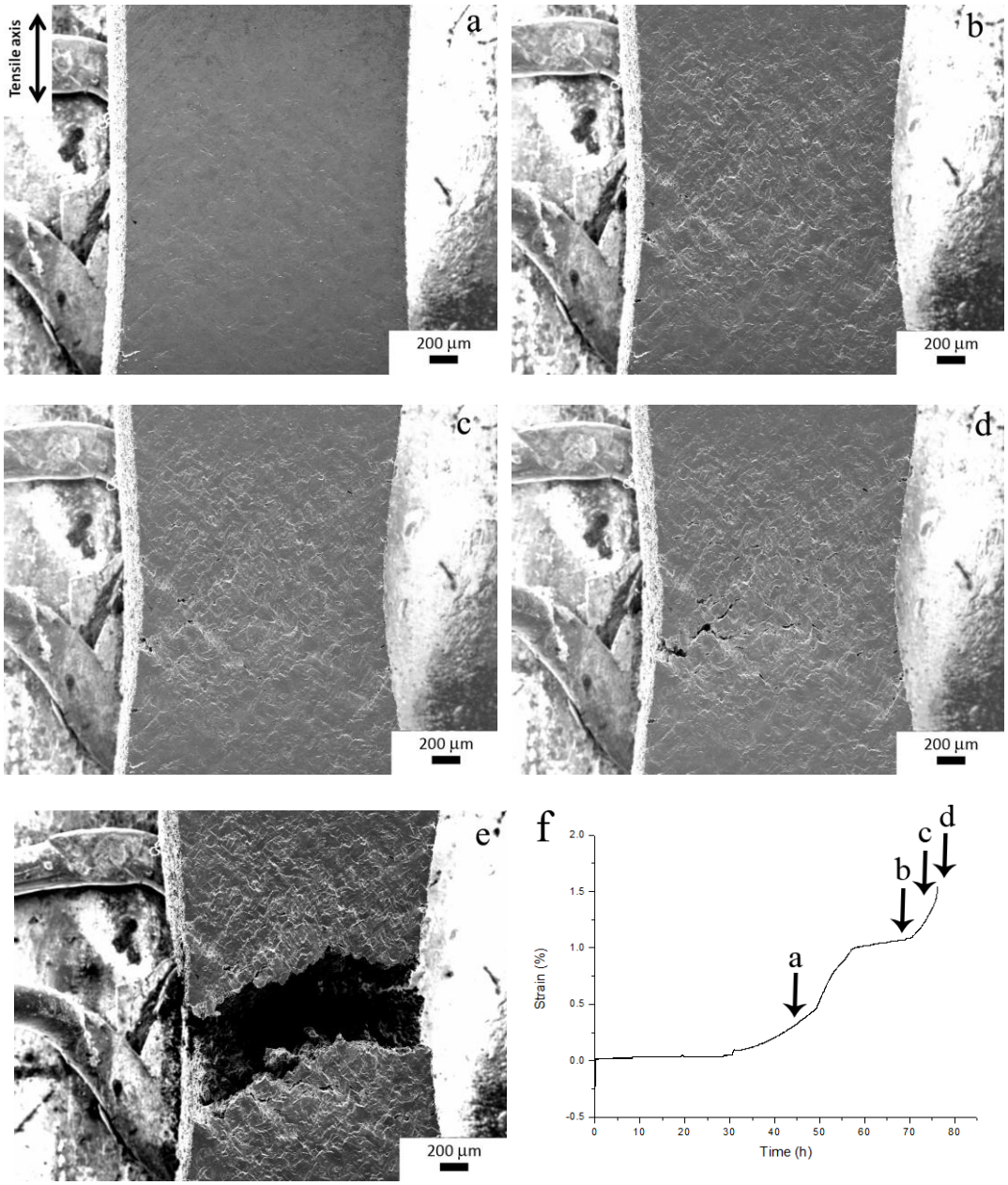

Fig. 4.37 Sequence of low-magnification SE SEM micrographs from a tensile-creep test performed at 300 MPa: (a) Secondary creep stage, 46 hours, ε~0.5%; (b) tertiary creep stage, 72 hours, ε~1.2%; (c) tertiary creep stage, 75 hours, ε~1.4%; (d) tertiary creep stage just prior to fracture, 76 hours, ε~1.5%; (e) after fracture, 76 hours, ε~1.6 %. (f) Corresponding strain versus time curve indicating the strain at which the (a-d) SEM images were taken.

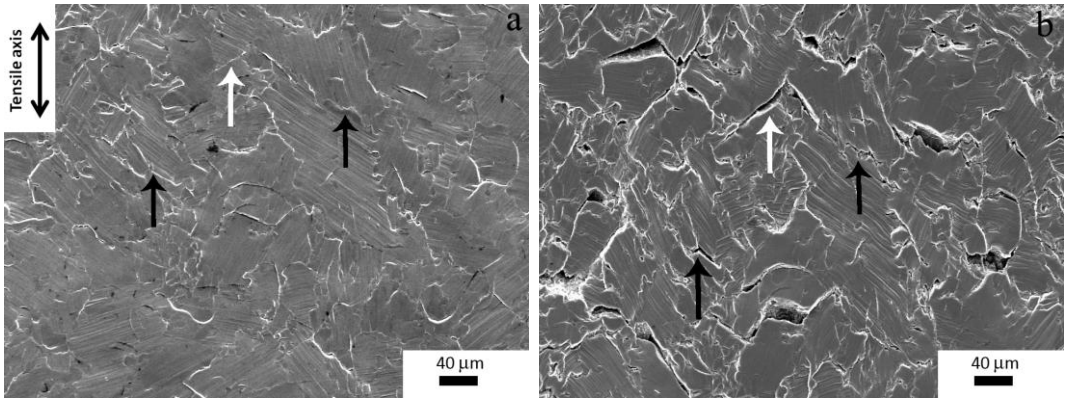

Fig. 4.38 SE SEM micrographs obtained during a tensile-creep test performed at 300 MPa: (a) secondary stage, 50h and ε~0.5 %; (b) tertiary stage, 76h and ε~1.5 %. (White arrow points B-rich phase cracking and black arrows point colony boundary cracks).

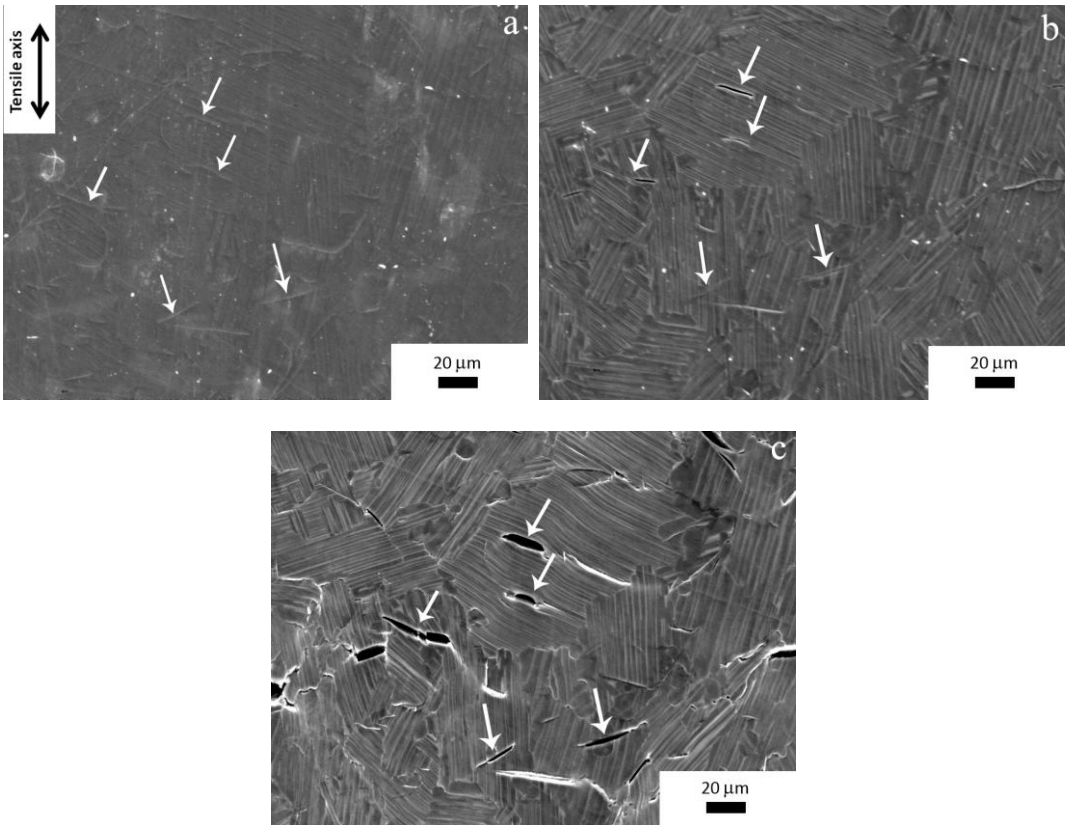

Fig. 4.39 SE SEM micrographs showing the evolution of B-rich phase cracks with increasing time for a tensile-creep test performed at 400 MPa: (a) initial microstructure; (b) secondary stage, 1 h and ε~0.2 %, (c) tertiary stage, 4 h and ε~0.6 %.

The deformation and fracture mechanisms at 425 MPa ($0.92\sigma_{max}$) and 450 MPa ($0.98\sigma_{max}$) were different from those observed at lower stresses. In these two cases, the strain rate of the secondary creep stage increased until $9{\cdot}10^{-7}$ s^{-1} and $2{\cdot}10^{-6}$ s^{-1}, respectively. Representative SEM images corresponding to the test performed at 425 MPa are shown in Figure 4.40. The most remarkable observation is that interlamellar ledges become apparent from the beginning of the secondary stage (Figure 4.40(a)). In particular, interlamellar ledges were first detected at a strain of 0.3 % and 0.1 % at 425 MPa and 450 MPa, respectively. They are shown in Figure 4.41 in the tensile-creep test at 450 MPa. This is similar to what was observed during the constant strain rate tensile tests (section 4.2.1.2). For these higher stress tensile-creep tests, colony boundary cracking was limited to the tertiary stage (Figure 4.40(b)). B-rich phase cracking was also observed under these testing conditions.

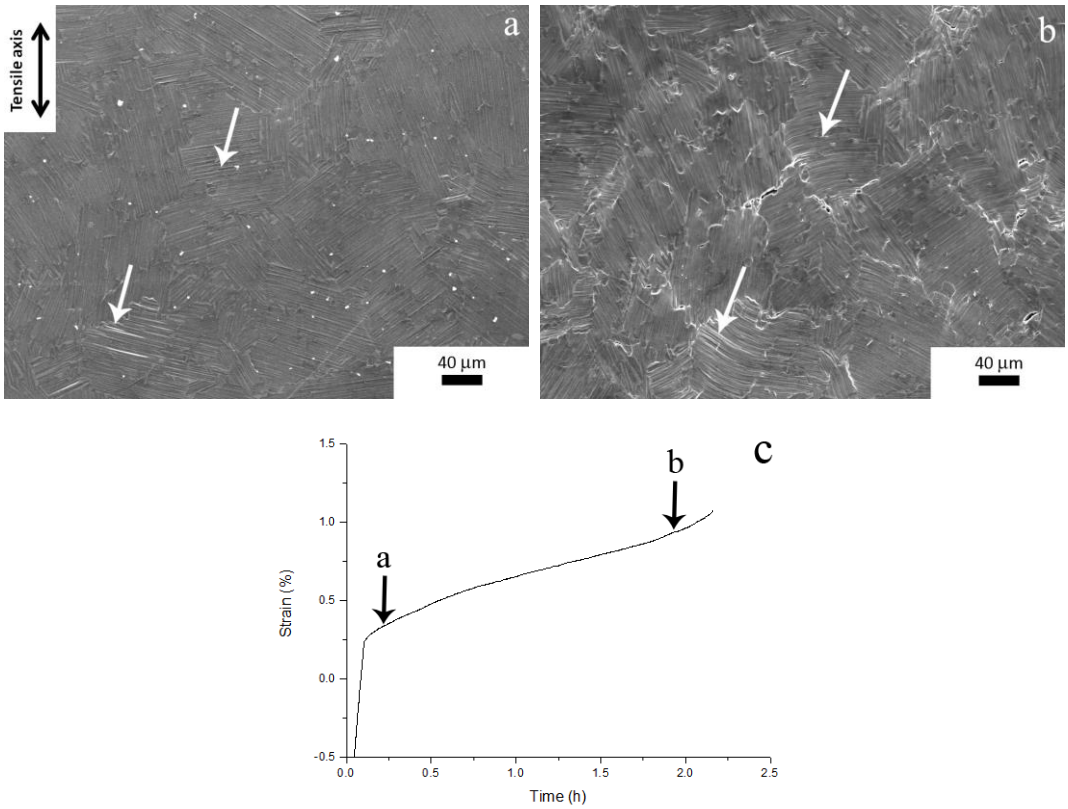

Fig. 4.40 SE SEM micrographs corresponding to a test at 425 MPa illustrating interlamellar ledges: (a) secondary creep stage, 0.2 hours, ε~0.3%; (b) tertiary creep stage, 2 hours, ε~1.0 %. A colony boundary crack was evident near the middle of the image in (b). (c) Corresponding strain versus time curve indicating the strain at which the (a) and (b) SEM images were taken.

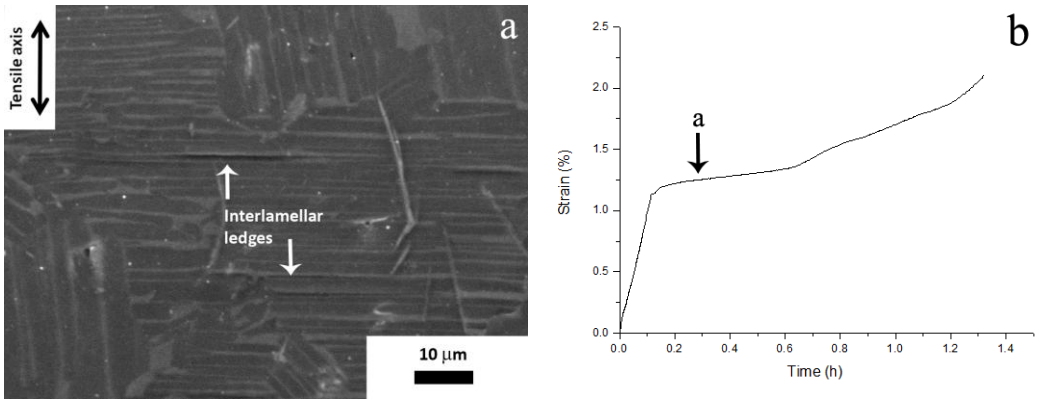

Fig. 4.41 (a) SE SEM micrograph corresponding to a test at 450 MPa illustrating interlamellar ledges during the secondary creep stage, 0.3 hours, ε~0.1%. (b) Corresponding strain versus time curve indicating the strain at which the (a) SEM image was taken.

In order to further understand the incidence of different crack propagation mechanisms in the catastrophic failure of these materials, the secondary cracks and the primary crack of the samples tested at 300 MPa and 450 MPa were analyzed *post-mortem*. The classification of the different secondary cracks (Figure 4.42(a)), along a 600 μm long section in the center of the sample, confirmed that the main fracture mechanism was intercolony cracking for all the tests conditions. This mechanism was more prevalent at the lowest stresses. Some interlamellar cracks were also detected but this mechanism was of less importance. Translamellar secondary cracks were rarely observed. The nature of crack propagation along the primary crack path was characterized across approximately 40 colonies and the results are plotted in Figure 4.42(b). They show that colony boundary and translamellar cracking were the main fracture mechanisms along the main crack. The former was particularly dominant in the creep test at 300 MPa.

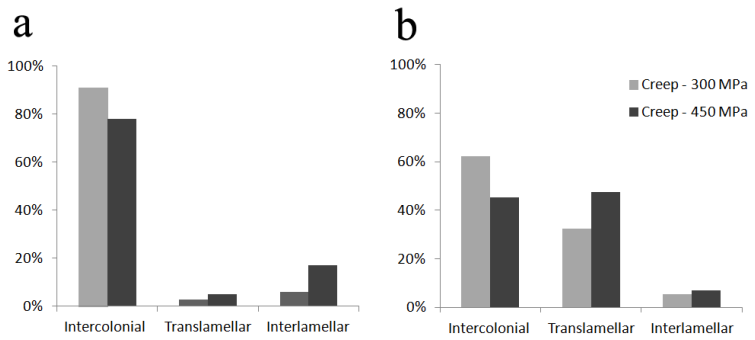

Fig. 4.42 Nature of the crack propagation paths in specimens deformed under tensile-creep at constant stresses of 300 MPa and 450 MPa: (a) Secondary cracks, (b) primary crack.

Understanding the high-temperature deformation and crack propagation mechanisms of lamellar γ-TiAl alloys is challenging for several reasons. First, attempts to rationalize the creep data in terms of conventional methods, such as the Dorn approach, are quite controversial [7, 128] as only a short secondary creep stage exists. Nevertheless, several studies have utilized this methodology [130-133, 143, 259-263] in an effort to determine the dominant deformation mechanisms. The large range of stress exponents and activation energies obtained points toward the simultaneous contribution of several deformation mechanisms, but the nature and incidence of each of them is unknown. Second, the wide array of microstructures and compositions available make it very difficult to devise general creep models for these alloys. The influence of microstructural parameters such as the colony size, the lamella size, the nature of the colony boundaries or the presence of second-phase particles is still unclear.

Most of the creep studies are performed under temperatures and stresses similar to those prevalent under service conditions, i.e., at temperatures ranging from 700-850 °C and within the stress range 80-500 MPa. These conditions are within the range utilized in the present study. It is generally believed that dislocation slip and mechanical twinning are active during the secondary creep stage of γ-TiAl alloys [7]. In particular, dislocation climb would be the rate controlling process at stresses below a certain threshold, depending on the colony size [133], and dislocation glide at higher stresses. Interface sliding has also been inferred from *ex situ* studies [145, 263, 264]. In particular, CBS was reported to occur in a 45XD alloy [134], with a colony size below 100 μm, subjected to tensile-creep test at 760 °C up to stresses of 200 MPa. The results shown in the current research work confirm the importance of CBS during the secondary creep stage of the Ti-45Al-2Mn-2Nb-0.8vol.%TiB_2. Furthermore, this mechanism appears to be active at relatively high stresses, up to about 400 MPa, even when the colony size (126 μm) is larger than the critical size proposed above (100 μm). This suggests that special care must be taken in reinforcing the CBS resistance if the creep resistance of γ-TiAl alloys under service conditions is to be improved. At stresses greater than 400 MPa, interlamellar ledges were observed during the early stages of the secondary creep regime. These were probably caused by the need to accommodate strain incompatibilities resulting from dislocation sliding between adjacent lamellae. CBS was limited to the tertiary stage. These observations are consistent with the prevalence of dislocation slip during the secondary stage at these very high creep stresses or, equivalently, during high constant strain rate tests at the quasi-static rates investigated.

Some authors have reported the occurrence of instabilities during creep of γ-TiAl alloys. For example, Wang *et al*. [264] reported that, together with dislocation activity and some

twinning, thinning and dissolution of α_2 lamellae and coarsening of γ-lamellae took place during creep of a fully lamellar Ti–47Al+2Cr+2Nb and Ti–47Al+2Cr+1Nb+1Ta at high stresses (e.g. > 200 MPa at 700 °C and > 400 MPa at 650 °C). Our *in situ* observations did not reveal any instabilities, even at 700 °C during the highest creep stresses investigated (450 MPa). A possible explanation for this discrepancy might be the presence of the significantly wider α_2 lamellae in the Ti-45Al-2Nb-2Mn-0.8vol.%TiB_2 alloy in the current study compared to that investigated by Wang *et al*. (α_2: 20-76 nm; γ:50-500 nm). In summary, the dissolution of α_2 lamellae, reported previously [264], was not observed. This suggests that there might be a critical α_2 spacing above which this type of instability is prevented.

Tertiary creep of γ-TiAl alloys has been attributed to the degradation of the fully lamellar structure due to phase transformations and dynamic recrystallization, to the formation of shear bands, to grain boundary sliding and to the formation of voids [7]. Other authors have also attributed the initiation of tertiary creep to strain incompatibilities between lamellar grains with soft and hard orientations leading to particularly elevated local stresses and, thus, to the formation of intergranular or interlamellar cracks [143]. Our *in situ* observations reveal that cracks formed preferentially at colony boundaries during the early stages of deformation in low-stress tensile-creep and during the later stages of deformation in high-stress tensile-creep.

4.2.3 Role of lamellae interfaces during high temperature constant strain rate straining

The mechanical response of the CC and the CCFC alloys tested *in situ* at 580 °C and 700 °C and at a strain rate of 10^{-3} s^{-1} and, in particular, the values of the maximum flow stresses and the elongations to failure obtained, are summarized in Table 4.5. Maximum flow stresses ranged from 440 MPa to 500 MPa and the elongation-to-failure varied between 1.3% and 1.9%.

Table 4.5 Maximum flow stress and the elongation-to-failure of tensile tested CC and CCFC material at 580 °C and 700 °C.

Sample	σ_{max} (MPa)	ε_{max} (%)
CC - 580 °C	458	1.3
CC - 700 °C	500	1.6
CCFC - 580 °C	437	1.8
CCFC - 700 °C	498	1.9

Figure 4.43 depicts representative EBSD inverse pole figure maps in the normal direction (ND) corresponding to selected areas of the CC samples before and after testing at a strain rate of 10^{-3} s^{-1} at 580 °C (Figures 4.43(a, b)) and 700 °C (Figures 4.43(d, e)). The SEM micrographs corresponding to the same areas in the post-test state (ε_{max}=1.3% at 580 °C and ε_{max}=1.6 % at 700 °C) are also added as they provide a complementary visualization of the changes in the specimens' surfaces (Figures 4.43(c, f)). Finally, Figures 4.43 (g, h) show the misorientation distribution histograms corresponding to the same areas before and after testing at both temperatures. Comparison of Figures 4.43 (a) and (b) reveals that changes in the orientation of some grains took place during the 580 °C deformation suggesting the occurrence of lattice rotations by crystallographic slip. Such grains have been highlighted using a rectangle in the map. Significant changes in the misorientation distribution histogram took place upon straining (Figure 4.43(g)). The pre-test histogram is formed mainly by three sharp peaks located at misorientation angles (θ) of 60 °, 70 °, and 90 °, which correspond to boundaries between the three main γ variants, namely, pseudotwins (60 ° around <111>$_\gamma$), order variants (120 ° around <111>$_\gamma$) and true twins (180 ° around <111>$_\gamma$) [7, 27, 28]. This histogram reveals that in the area of the microstructure tested at 580 °C that was mapped by EBSD before testing (Figure 4.43(a)), true twin interfaces were the most abundant, followed by order variants and pseudotwins (Figure 4.43(g)). This is consistent with previous investigations, which revealed that true twin γ/γ boundaries occur more frequently due, at least partly, to their lower interfacial energy [7, 27, 39 47]. After testing at 580 °C, the fraction of true twin boundaries decreased significantly. The fraction of pseudotwins and order variants decreased only slightly and the frequency of interfaces with all the other misorientation angles increased (Figure 4.43(g)). The dramatic decrease of the frequency of true twin boundaries upon deformation suggests a high incidence of crystallographic slip at true twin-related lamellae, leading to large lattice rotations on both sides of the boundary and, thus, to significant changes in the boundary misorientation angle. This is consistent with a lower resistance to slip transfer across true twin γ/γ interfaces. Although the barrier strength of the different γ/γ lamellae boundaries has not been measured previously, it has been speculated that true twin interfaces should be the softest because slip transfer could be accomplished by conjugate slip systems, which are in mirror symmetry [265].

In a representative area of the CC samples tested at 700 °C that was mapped by EBSD before and after testing (Figures 4.43(d, e)), however, no major variations in the orientation of the grains were detected. After deformation (ε=1.6 %) the corresponding misorientation distribution histogram (Figure 4.43(h)) reveals that, in this region, the fraction of true twin

boundaries was relatively low and, moreover, similar to that of order variants. In agreement with the above observations, no significant changes took place in the boundary misorientation histogram. This data suggests that slip does not take place homogeneously throughout the microstructure. Regardless the temperature, the incidence of crystallographic slip has been experimentally observed to be related to the fraction of true twin boundaries. SEM examinations (Figure 4.43(f)) revealed, additionally, the appearance of interlamellar ledges (white arrows) and incipient colony boundary relief (red arrows), that were identified *in situ* at strains of 1.1 % and 1.4 %, respectively. These SEM observations are consistent with a moderate enhancement of diffusion-based mechanisms at higher temperatures.

Figure 4.44 depicts the EBSD inverse pole figure maps in the ND corresponding to selected and representative areas of the CCFC samples before and after testing at a strain rate of 10^{-3} s^{-1} at 580 °C (Figs. 4.44(a, b)) and 700 °C (Figures 4.44(d, e)). The SEM micrographs of the same areas in the post-test state (ε_{max}=1.8% at 580 °C and ε_{max}=1.9 % at 700 °C) are also added as they provide a complementary visualization of changes in the deformed surface (Figure 4.44(c, f)). Finally, Figures 4.44(g, h) show the misorientation distribution histograms corresponding to the same areas before and after testing at both temperatures. Changes in the orientation of some grains (highlighted using rectangles) are clearly visible at both temperatures, suggesting the occurrence of crystallographic slip. The inverse pole figures showing the orientation on the tensile axis both before and after the tensile test at 580 °C confirmed the occurrence of lattice rotations. In particular, $\langle 110 \rangle$ directions tended to align with the loading axis. The misorientation distribution histograms (Figures 4.44(g, h)) revealed a predominance of true twin boundaries in the two areas examined. They also revealed a pronounced decrease in the frequency of such boundaries upon straining, giving rise to a higher background level. These observations are consistent with a prevalence of crystallographic slip at both temperatures and with enhanced slip transfer across true twin interfaces. The SEM micrographs (Figures 4.44(c, f)) reveal the appearance of interlamellar ledges (white arrows) at 580 °C and 700 °C. Interlamellar ledges first appeared at strains of 1.7 % and 1.5 % in the 580 °C and 700 °C tensile-tested samples, respectively. Moreover, at 700 °C colony boundary relief (red arrow) is also detected at a strain of 1.9 % (Figure 4.44(f)). This phenomenon is consistent with a higher contribution from diffusion-based mechanisms to the deformation at high temperatures.

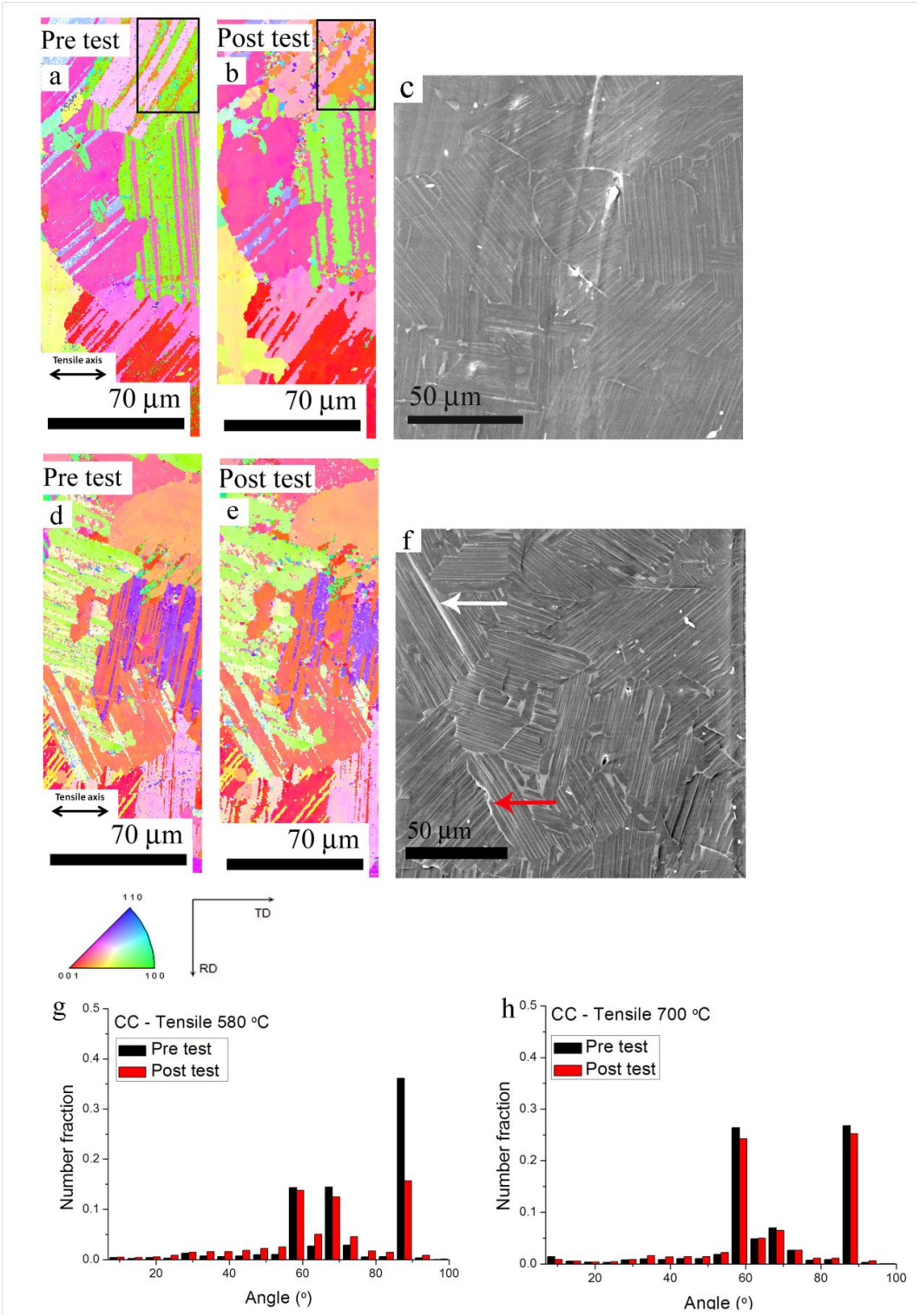

Fig. 4.43 EBSD inverse pole figure maps in the ND and BSE SEM micrographs corresponding to selected areas of the CC microstructure: (a) before and (b, c) after the tensile test at 580 °C, σ_{max}= 458 MPa, ε_{max}= 1.3 %; (d) before and (e, f) after the tensile test at 700 °C, σ_{max}= 500 MPa, ε_{max}= 1.6 %. (g,h) Comparison of the misorientation distribution histograms in those same areas before and after the tensile tests at 580 °C (g) and at 700 °C (h).

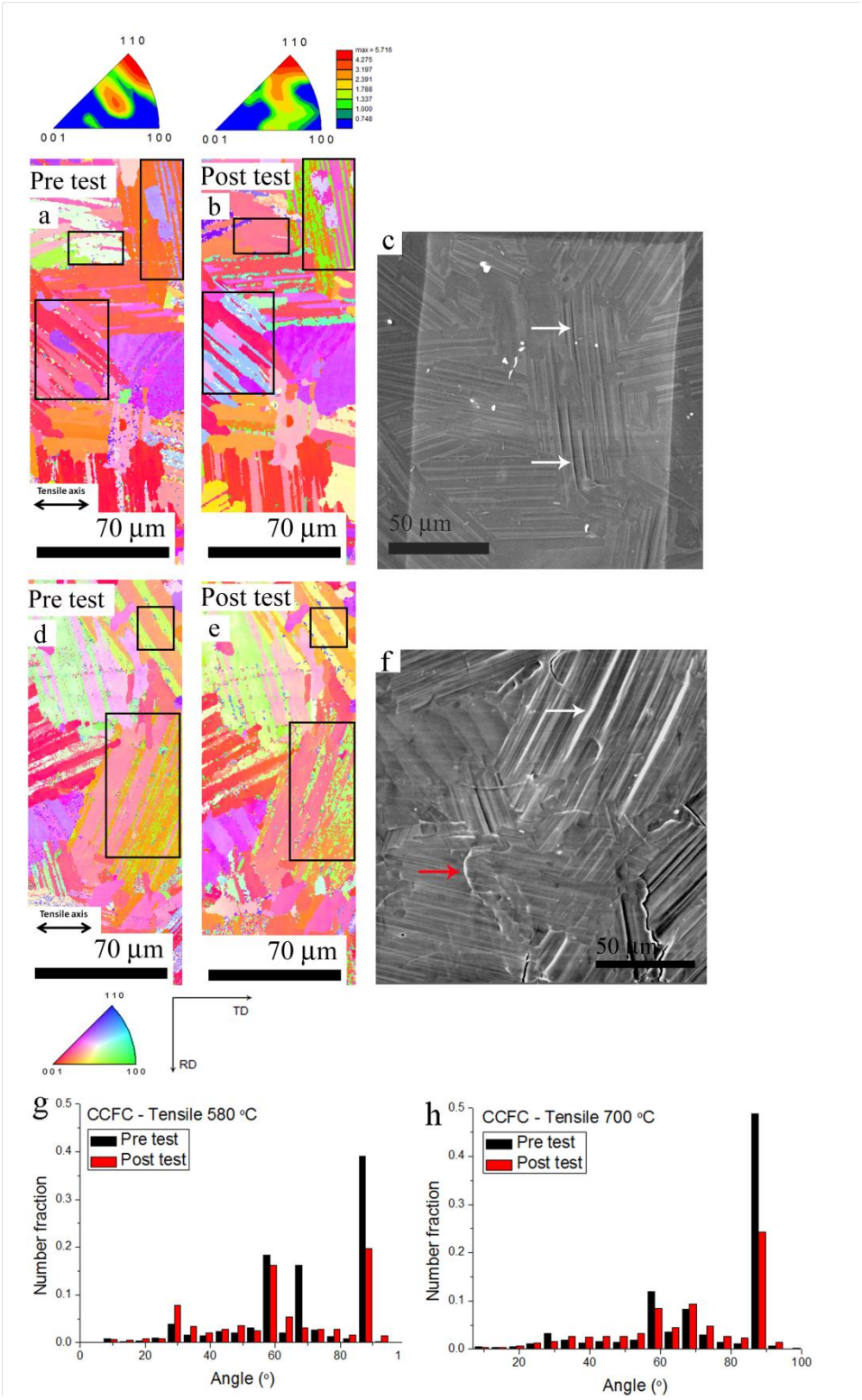

Fig. 4.44 EBSD inverse pole figure maps in the ND and BSE SEM micrographs corresponding to selected areas of the CCFC microstructure: (a) before and (b, c) after the tensile test at 580 °C, σ_{max}= 437 MPa, ε_{max}= 1.8 %, including the corresponding inverse pole figures showing the orientation of the tensile axis; (d) before and (e, f) after the tensile test at 700 °C, σ_{max}= 498 MPa, ε_{max}= 1.9 %. (g,h) Comparison of the misorientation distribution histograms in those same areas before and after the tensile tests at 580 °C (g) and at 700 °C (h).

As explained above in section 4.2.1.1, monocrystalline γ-TiAl lamellar structures exhibit high plastic anisotropy as their yield stress and elongation-to-fracture strongly depend on the lamellar orientation with respect to the loading axis (ϕ). Many authors have worked on this issue through the study of PST crystals [113-115]. When lamellae are perpendicular to the loading axis, shear is mostly transverse to different lamellae and dislocation pile ups occur at the lamellae interfaces (hard deformation mode). When ϕ is comprised between 30 ° and 60 ° shear occurs parallel to the lamellae interfaces and pile ups form preferentially at the domain boundaries (soft deformation mode). Due to the inherent complexity of polycrystalline γ-TiAl microstructures, it has proven difficult to relate the yield strength and a specific length scale (or a combination of them) using a Hall-Petch type law. A number of studies have attempted to carry out this task and a wealth of Hall-Petch constants (K_y) have been obtained [7]. Similarly, selection of the most critical length scale out of the many available (colony size, grain size, lamellar spacing, domain size) has proven challenging, as devising processing routes that allow controlling one microstructural feature while leaving all the others constant is difficult. Overall, it has become clear that different types of interfaces have to be taken into account to describe the strengthening of two phase γ-TiAl alloys, and the lamellar spacing seems to be the most influential of all [41].

Our results show that the frequency of true twin γ/γ lamella interfaces decreases dramatically with straining in both the CC and CCFC microstructures tested in tension at constant strain rate (10^{-3} s^{-1}) and at temperatures ranging from 580 °C to 700 °C, while those of other γ/γ interfaces remain basically constant, proving the relatively higher weakness of the former. Thus, at least in the alloy investigated, this study suggests that the relevant length scale might be strongly influenced by the distance between non-true twin boundaries and, thus, could be larger than the width of individual lamellae.

4.2.4 Analysis of slip activity during creep deformation of lamellar and duplex microstructures

The total strain versus time creep curves corresponding to the CCFC and PMFC microstructures deformed at 700 °C and $0.65\sigma_{max}$ (σ_{cr}(CCFC)=325 MPa, σ_{cr}(PMFC)=300 MPa) are plotted in Figure 4.45. Measured secondary creep strain rates were of $5\cdot10^{-7}$ s^{-1} and $2\cdot10^{-6}$ s^{-1}, respectively. The lamellar alloy (CCFC) was more creep resistant than that with a duplex microstructure (PMFC). In particular, the secondary strain rate was higher and the creep life was shorter for the latter.

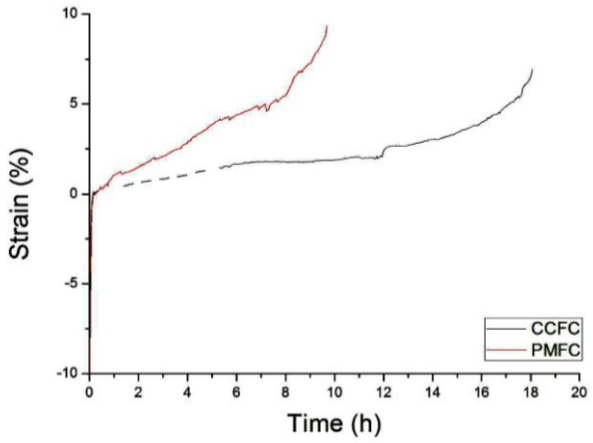

Fig. 4.45 Creep curves corresponding to the CCFC and the PMFC microstructures deformed in tension at 700 °C and at a constant stress of 65%σ_{max}

Figure 4.46 illustrates a sequence of SEM micrographs showing the microstructural evolution of an area in the PMFC sample with increasing creep strain. After a deformation of 0.3 %, some relief was apparent both at the colony boundaries (CS=98 μm) as well as at the boundaries of the equiaxed γ grains (GS=4 μm). With increasing strain, cracking of the boundaries became apparent. These observations suggest the operation of boundary sliding during deformation. This is consistent with previous reports [266, 267]. Due to the relatively small size of the γ grains, a large surface area of grain boundaries was present. Boundary cracking initiated at strains as small as 1%. This phenomenon was also visible in the higher-magnification micrographs of Figure 4.47 which reveal, additionally, crystallographic slip activity. The width of the slip traces and their number increased dramatically with deformation.

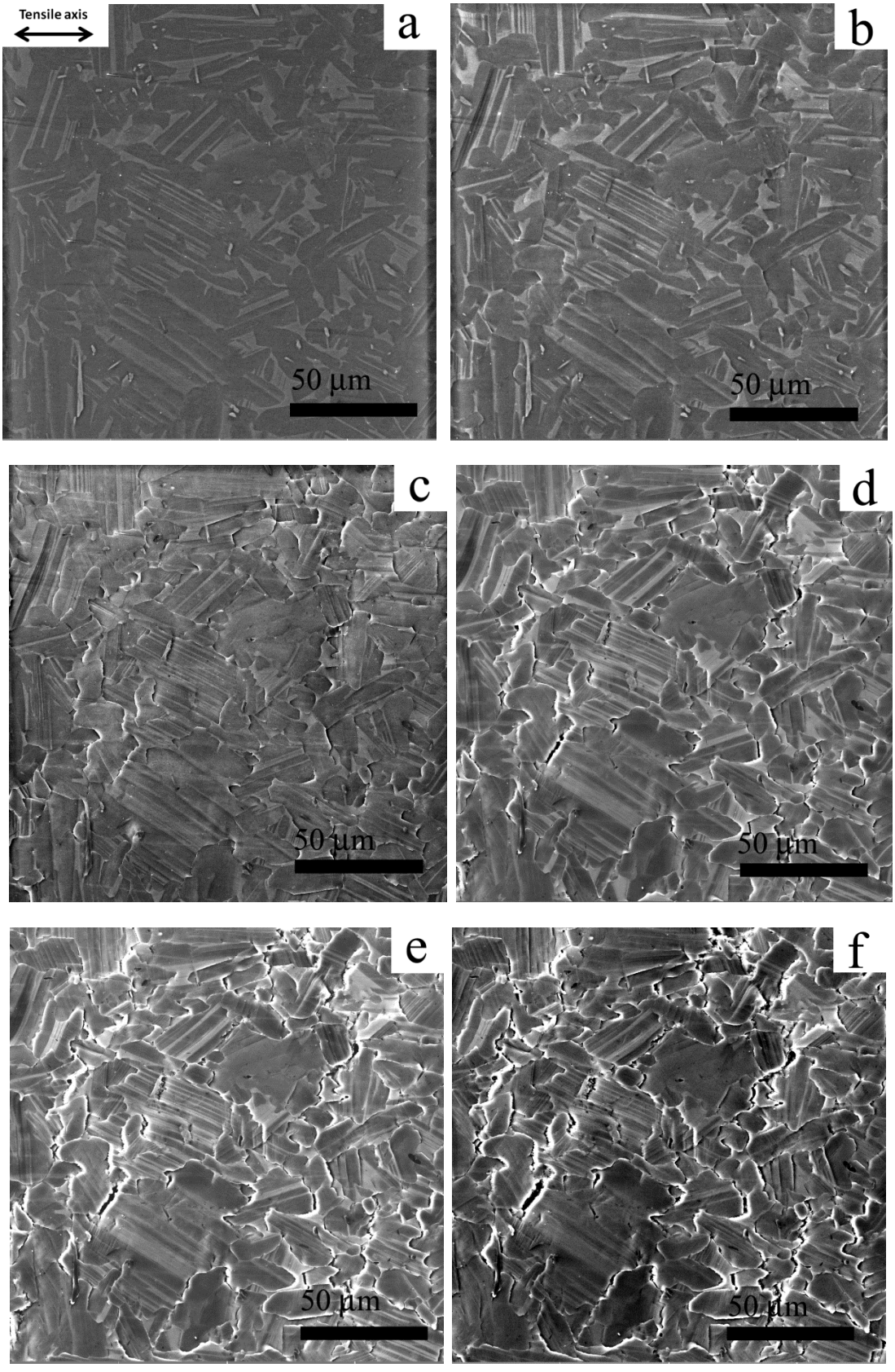
Tensile axis
a
50 µm
b
50 µm
c
50 µm
d
50 µm
e
50 µm
f
50 µm

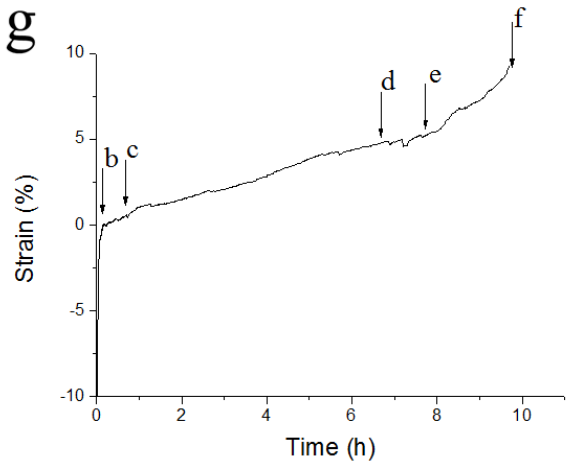

Fig. 4.46 Sequence of SE SEM micrographs showing the evolution of the PMFC microstructure during creep straining at 700 °C: (a) 0 h; (b) secondary creep stage, 0.3 h, ε ~0.1 %; (c) secondary creep stage, 1.0 h, ε ~1.0 %; (d) secondary creep stage, 7.0 h, ε~5.0 %; (e) tertiary creep stage, 8.3 h, ε~6.2 %; (f) after fracture, 9.7 h, ε_{max}~9.4 %; (g) Corresponding total strain versus time curve indicating the strains at which the (b)-(f) SEM images were taken.

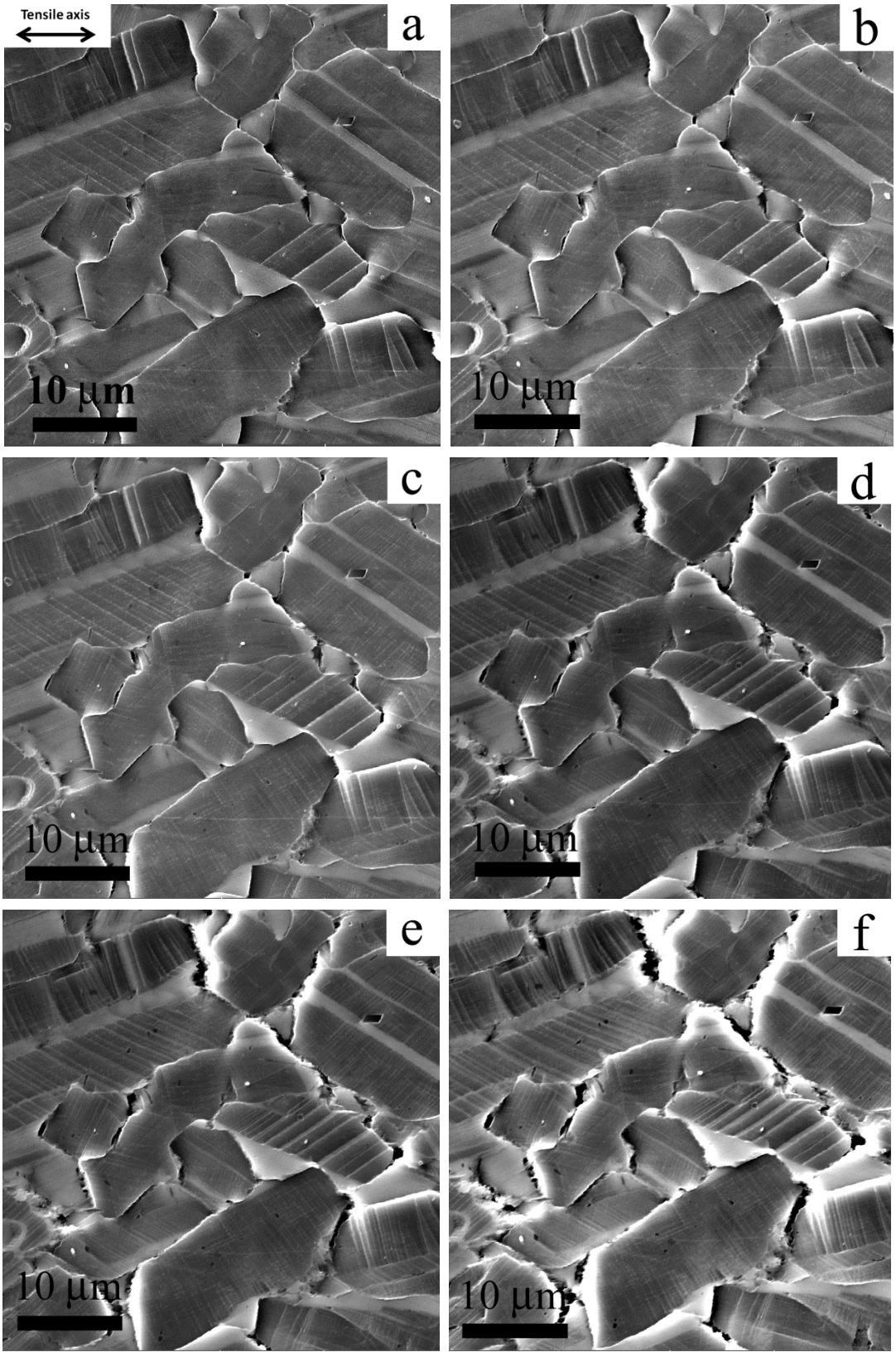
Tensile axis
a
10 µm
b
10 µm
c
10 µm
d
10 µm
e
10 µm
f
10 µm

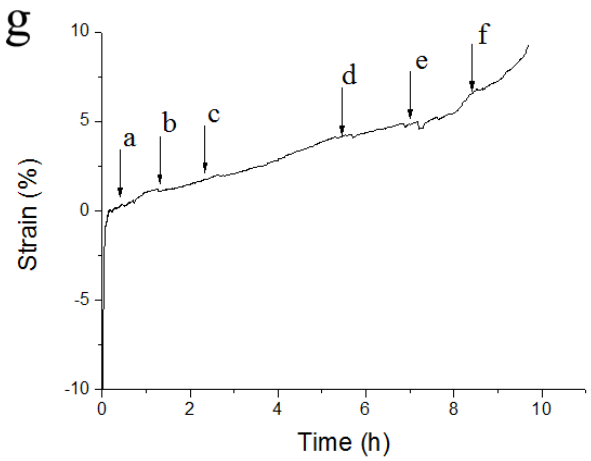

Fig. 4.47 Sequence of SE SEM micrographs at higher magnifications showing the evolution of the PMFC microstructure during creep straining at 700°C: (a) secondary creep stage, 0.8 h, ε~0.7 %; (b) secondary creep stage, 1.3 h, ε~1.1 %; (c) secondary creep stage, 2.7 h, ε~2.0 %; (d) secondary creep stage, 5.8 h, ε~4.2 %; (e) secondary creep stage, 7.3 h, ε~4.6 %; (f) tertiary creep stage, 8.6 h, ε~6.8 %; (g) Corresponding total strain versus time curve indicating the strains at which the (a)-(f) SEM images were taken.

The microstructural evolution of the CCFC sample (CS=181 μm) during creep under the same conditions is illustrated in Figure 4.48. Although colony boundary relief leading to colony boundary cracking was also present during deformation, its incidence was significantly lower than in the PMFC sample. In particular, these two phenomena were only noticeable after strains of 1 % and 1.8 %, respectively. These strains, and especially the strain associated to the initiation of boundary cracking, were higher than those observed in the PMFC alloy. These differences are consistent with an enhanced resistance to boundary sliding in the CCFC sample associated to the larger colony size. Indications of crystallographic slip activity (Figure 4.48(e)) were also evident in the lamellar microstructure of the CCFC sample.

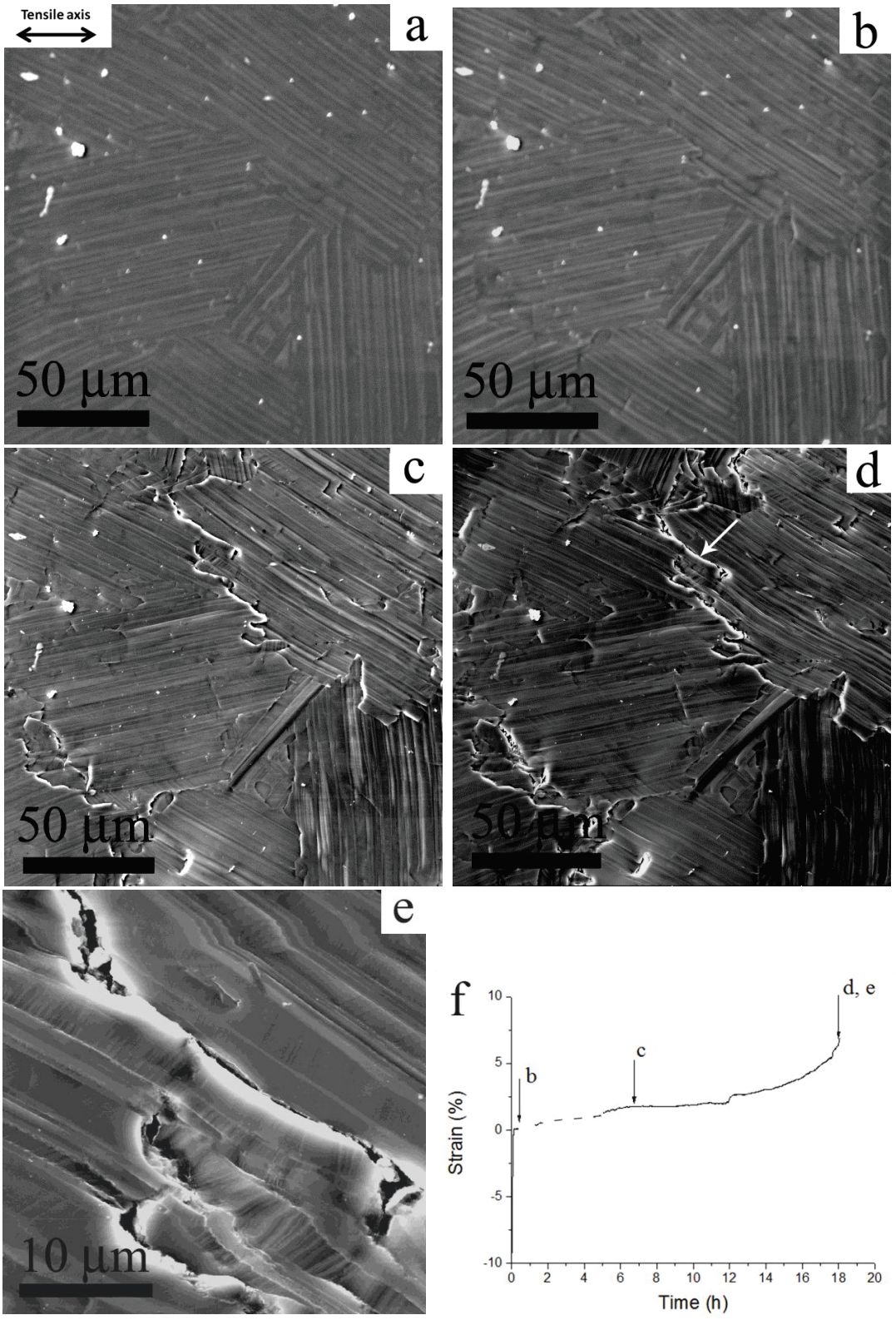

Fig. 4.48 Sequence of SE SEM micrographs showing the evolution of the CCFC microstructure during creep straining at 700 °C: (a) 0 h; (b) secondary creep stage, 0.5 h, ε~0.3 %; (c) secondary creep stage, 7.0 h, ε~1.8 %; (d) after fracture, 18.1 h, ε_{max}~ 7.0 %; (e) higher magnification SE SEM micrograph from the area pointed with the arrow in (d); (f) Corresponding total strain versus time curve indicating the strains at which the(b)-(e) SEM images were taken.

4.2.4.1 Methodology to estimate ordinary and superdislocation activity

Estimating the activity of ordinary and superdislocations in γ-TiAl from the analysis of the surface slip plane traces observed by SEM is not trivial because each {111} slip plane is shared by one ordinary system and two superdislocation systems (Table 1.2) and, furthermore, the CRSS values corresponding to both types of dislocations for the alloy under study are not known. In order to investigate further dislocation activity we have carried out the following trace analysis.

First, we identified 100 slip traces in the creep-tested PMFC material (75 in equiaxed grains and 25 in the lamellae regions) and 29 slip traces (16 in equiaxed grains and 13 in the lamellae regions) in the creep-tested CCFC material. Detecting slip traces in the CCFC material proved more challenging due to the finer size of the lamellae as well as to the lower strains attained. Then, we divided the measured traces in three groups. The first one corresponds to traces for which the Schmid factor of the associated ordinary system is higher than the Schmid factor of all other ordinary systems *and* at least one of the Schmid factors of the two associated superdislocation systems is higher than the Schmid factor of all other superdislocation systems. This group (Group 1) corresponds undoubtedly to dislocation events obeying the Schmid law with respect to the applied stress. A second group (Group 2) is formed by traces for which the opposite is true, i.e., the Schmid factors associated to those traces corresponding to the ordinary and superdislocation systems are both smaller than the Schmid factors of other available systems. These traces correspond to dislocation activity that does not obey the Schmid law with respect to the applied stress, i.e., such dislocations are activated as a consequence of the presence of local stresses. Finally, a third group (Group 3) is formed by traces for which there is uncertainty as to whether the Schmid law with respect to the applied stress is obeyed, as the Schmid factor of either the ordinary or the superdislocation systems associated to such traces are smaller than the factors corresponding to other systems of similar type.

The fraction of traces corresponding to each group for the CCFC and PMFC materials is summarized in Table 4.6. Similar proportions are observed for the two microstructures analyzed. In both materials, Group 1 is formed by 13 to 17 % of the traces, Group 2 is formed by 31 to 38 % and close to 50 % of the measured traces belong to Group 3.

Table 4.6 Fraction of traces corresponding to each group in CCFC and PMFC materials.

	CCFC	PMFC
Group 1	17 %	13 %
Group 2	31 %	38 %
Group 3	52 %	49 %

In the following we propose a methodology to evaluate the activity of ordinary and superdislocations associated to Group 1 traces. A trace will be assigned to an ordinary dislocation when the resolved shear stress on the ordinary system (RSS_o) is higher than the CRSS of that system ($CRSS_o$) and, simultaneously, the resolved shear stress on the superdislocation system (RSS_s) with the highest Schmid factor out of the two systems sharing the same slip plane is lower than the CRSS of that system ($CRSS_s$), i.e.:

$$RSS_o\ (MPa) = \sigma \cdot SF_o > CRSS_o = R \cdot CRSS_s \quad (4.1)$$

$$RSS_s\ (MPa) = \sigma \cdot SF_s < CRSS_s \quad (4.2)$$

where SF_o is the Schmid factor of the ordinary system with respect to the applied stress (σ(PMFC)= 300 MPa; σ(CCFC)= 325 MPa), SF_s is the Schmid factor of the superdislocation system, and R is the ratio between the critical resolved shear stress of ordinary and superdislocations ($R = CRSS_o / CRSS_s$). Conversely, a trace will be assigned to a superdislocation when inequalities 4.3 and 4.4 are true simultaneously:

$$RSS_o\ (MPa) = \sigma \cdot SF_o < CRSS_o = R \cdot CRSS_s \quad (4.3)$$

$$RSS_s\ (MPa) = \sigma \cdot SF_s > CRSS_s \quad (4.4)$$

It is implicit in this analysis that each observed plane trace corresponds to a single slip system. The two above systems of inequalities are solved graphically for a given trace t_i in Figure 4.49, which represents the variation of $CRSS_s$ with respect to R for that particular trace. The area shaded with squares corresponds to ($CRSS_s$, R) pairs for which the analyzed trace is assigned to ordinary dislocation slip, whereas the area filled with dots corresponds to ($CRSS_s$, R) pairs for which the trace is assigned to superdislocation activity. R_{ci} ($=SF_{oi}/SF_{si}$) is a critical R value that denotes the transition between ordinary and superdislocation slip, i.e., when $R < R_c$, t_i is assigned to ordinary dislocations and, conversely, when $R > R_c$, t_i is assigned to superdislocation slip.

The analysis described above was applied to Group 1 traces belonging to the gamma grains of the PMFC material, as the higher number of available traces allowed a better statistic study. The relative activity of ordinary and superdislocations is presented in Figure 4.50 for different R values. The figure reveals that superdislocation activity increases (and, in turn, ordinary slip activity decreases) linearly with respect to R with a slope equal to 0.14 %. Also, the activity of ordinary dislocations becomes negligible for R values higher than 1.5 and the activity of superdislocations is zero for R values lower than 1. The true R value corresponding to the Ti4522XD alloy under study is not known, as the critical resolved shear stresses of the different slip systems have never been measured for this alloy. In fact, a wide dispersion of CRSS values has been reported for single crystalline γ-TiAl alloys, as reflected in Table 4.7. In general, it is believed that the activity of superdislocations increases with increasing Al content and that it is dependent on orientation, although these aspects are still controversial [117, 268]. Also, an anomalous temperature dependence of the CRSS of ordinary and superdislocations has been reported [123-126, 268]. Both parameters exhibit a peak at temperatures between 700 °C and 1000 °C. Despite the little data available, Table 4.7. suggests that, in general, alloys with high Al content (54-58 at.%) exhibit very high R values (1.5-1.9) at temperatures ranging from 25 °C to 700 °C. When the Al content decreases to 50 at.%, the R values measured are significantly lower (0.8). Although the R value for our Ti4522XD alloy is not known at any temperature, the low Al content would be consistent with values that are lower than those observed for highly alloyed systems, i.e., it is likely that R<1.5 (Table 4.7).

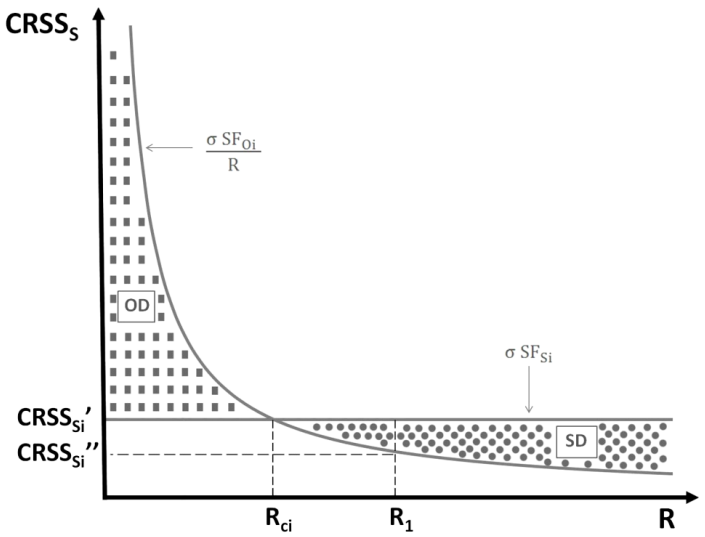

Fig. 4.49 Schematic drawing showing the variation of $CRSS_s$ with respect to R for a given trace t_i. The shaded areas correspond to ($CRSS_s$,R) pairs for which ordinary (OD) and superdislocations (SD) are active. R_{ci} is a critical R value which marks the transition from ordinary to superdislocation slip.

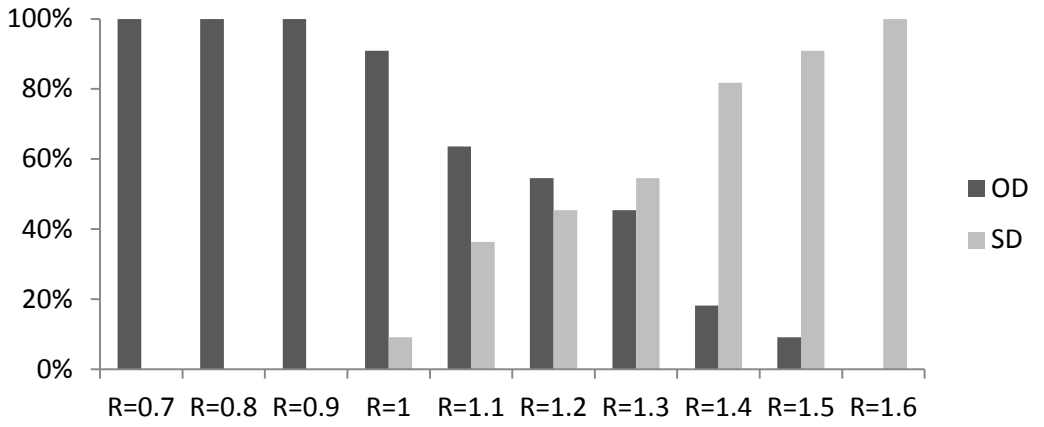

Fig. 4.50 Relative activity of OD and SD for different R values in the gamma grains of the duplex microstructure (PMFC) during creep at 700 °C and 300 MPa.

For a given R (for example, R_1 in Fig. 4.49) there is an interval of $CRSS_s$ values $[CRSS_s´-CRSS_s´´]_i$ for which trace t_i could be assigned to superdislocation slip. If $CRSS_s$ was unique for a given composition and microstructure, all $[CRSS_s´-CRSS_s´´]_i$ should intersect exactly at that $CRSS_s$ value. If several $CRSS_s$ values existed, which could be associated, for example, to different orientations, several clusters of $[CRSS_s´-CRSS_s´´]_i$ intervals intersecting at different $CRSS_s$ values would exist. It has been analyzed the intersections among the $[CRSS_s´-CRSS_s´´]_i$ intervals corresponding to all the Group 1 traces detected in the grains of the PMFC sample for R values of 0.7, 1, and 1.5. In all three cases, almost all $[CRSS_s´-CRSS_s´´]_i$ intervals intersected at one single $CRSS_s$ range, which was then taken as the best estimation of the $CRSS_s$ for the material under study. In particular, when R=0.7, $CRSS_s$=(126-177) MPa for 100% of the traces; when R=1, $CRSS_s$=(123-131) MPa for 91% of the traces; when R=1.5, $CRSS_s$=(97-98) MPa for 100% of the traces. The corresponding $CRSS_o$ values were, respectively, (88-124) MPa for R=0.7, (123-131) MPa for R=1, and (146-147) MPa for R=1.5.

Table 4.7 Reported CRSS values for γ-TiAl single crystal alloys.

Composition (at.%), [orientation of the tensile axis]	**T(°C)**	**$CRSS_o$ (MPa)**	**$CRSS_s$ (MPa)**	**$R=CRSS_o/CRSS_s$**	**Ref.**
Ti-56Al, [$\mathbf{021}$]	700	160			[268]
Ti-56Al, [$\mathbf{001}$]	700		180	0.9	[268]
Ti-56Al, [$\mathbf{251}$]	700		100	1.6	[268]
Ti-56Al, [$\mathbf{\bar{1}52}$]	700		90	1.8	[268]
Ti-55.5Al, [$\mathbf{001}$]	600-700		170		[123]
Ti-55.5Al, [$\mathbf{010}$]	600-700		120		[123]
Ti-55.5Al, [$\mathbf{\bar{1}10}$]	600-700		90		[123]
Ti-56Al, [$\mathbf{001}$]	600-700		160		[126]
Ti-56Al, [$\mathbf{010}$]	600-700		130		[126]
Ti-56Al, [$\mathbf{\bar{1}10}$]	600-700		120		[126]
Ti-56Al, [$\mathbf{\bar{3}\ 12\ 7}$]	900	110			[126]
Ti-56Al, [$\mathbf{\bar{1}\ 6\ 3}$]	900	120			[126]
Ti-56Al, [$\mathbf{\bar{1}\ 12\ 5}$]	900	130			[126]
Ti-56Al, [$\mathbf{\bar{2}\ 4\ 7}$]	900		150		[126]
Ti-56Al, [$\mathbf{\bar{1}\ 6\ 12}$]	900		185		[126]
Ti-58Al, [$\mathbf{021}$]	25	175			[268]
Ti-58Al, [$\mathbf{\bar{1}52}$]	25		90	1.9	[268]
Ti-56Al, [$\mathbf{021}$]	25	165			[268]
Ti-56Al, [$\mathbf{\bar{1}52}$]	25		85	1.9	[268]
Ti-54Al, [$\mathbf{021}$]	25	140			[268]
Ti-54Al, [$\mathbf{\bar{1}52}$]	25		75	1.9	[268]
Ti-50Al, [$\mathbf{021}$]	25	45			[268]
Ti-50Al, [$\mathbf{\bar{1}52}$]	25		60	0.8	[268]

4.2.4.2 "Non-Schmid" slip activity

Table 4.6. reveals that, in the two microstructures analyzed, a large amount of the slip traces analyzed corresponds to slip activity that does not comply with the Schmid law with respect to the applied stress. In particular, a minimum of 30 to 40% of the traces belongs to Group 2. Furthermore, Table 4.8. illustrates the fraction of Group 2 traces detected in the grains and the lamellae of the PMFC sample, evidencing that such events are frequent in both cases and suggesting that this type of slip activity should be taken into account in models aiming to provide a realistic description of the plasticity of these materials. Figure 4.51 shows that a 50 to 60% of Group 2 slip traces, in both the equiaxed grains and the lamellae, became apparent at ε=0-3%, while the rest were observed at higher strains.

Table 4.8. Fraction of traces corresponding to each group in PMFC grains and lamellae

	PMFC - Grains	PMFC - Lamellae
Group 1	15 %	8 %
Group 2	36 %	44 %
Group 3	49 %	48 %

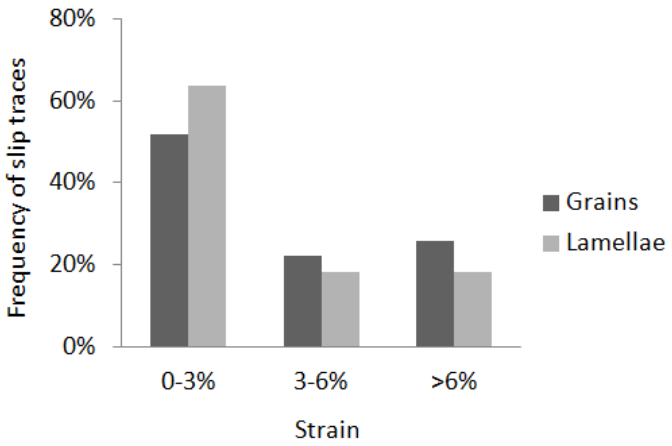

Fig. 4.51 Frequency of Group 2 slip traces with increasing strain in the PMFC samples tested at 700 °C under creep conditions (σ_{cr}(PMFC)=300 MPa). Traces belonging to grains and lamellae in the PMFC sample.

Non-Schmid behavior with respect to the applied stress in lamellar γ-TiAl structures has been reported earlier. Zupan and Hemker [123] observed it in a Ti-55.5 at.%Al intermetallic and Woodward and Rao [269] predicted its occurrence by ab-initio simulations as a consequence of the presence of small but significant edge atomic displacements near the core

of ordinary dislocations, which could interact with stresses other than the resolved stresses on the glide plane. Additionally, non-Schmid behavior in lamellae could be caused by high local stress concentrations at the interfaces leading to preferential slip transfer to conjugate systems (which may not have the highest Schmid factor) in true twin-related lamellae [265].

The origin of the relatively high non-Schmid slip activity with respect to the applied stress observed in the present study in the equiaxed γ-grains of the PMFC duplex microstructure is, however, still not known. This behavior could be partly related to the accommodation of the high local stress concentrations at triple points resulting from the operation of grain boundary sliding [270]. The accommodation mechanisms proposed in the literature are either based on diffusion transport [271, 272] or on the movement of dislocations along grain boundaries or through the interior of the grains [273, 274]. The predominance of one or the other is still controversial. Some studies based on the analysis of marker lines and on the observation of the grain geometry in (sub)surface regions have concluded that diffusion accommodation prevails [275, 276]. Other works, in which texture analysis was utilized as the main tool to investigate deformation mechanisms, report that dislocation slip acts primarily as an accommodation mechanism for grain boundary sliding in Mg and Al alloys [277, 278]. Analysis of slip traces during *in situ* testing could prove to be an excellent technique to contribute to this discussion since GBS accommodation by intragranular slip should give rise to non-Schmid slip behavior with respect to the applied stress, as dislocations would be activated in response to the high local stress concentrations at triple points. As revealed by Figures 4.46 and 4.47, boundary sliding takes place profusely in the PMFC microstructure deformed under creep conditions and the incidence of this mechanism is particularly high along the boundaries of the equiaxed gamma grains. The present results, thus, are consistent with the operation of intragranular slip as an accommodation mechanism for GBS in duplex microstructures.

5 Conclusions

5. Conclusions

In the present research work the high temperature deformation and fracture mechanisms of a Ti-45Al-2Nb-2Mn+0.8vol.%TiB_2 (Ti4522XD) intermetallic alloy have been analyzed for different representative microstructures with the aim of facilitating microstructural design for specific applications. The high temperature mechanical behavior has been successfully studied using the pioneer experimental technique of *in situ* mechanical testing inside a scanning electron microscope (SEM) aided by electron backscattered diffraction (EBSD) at temperatures as high as 700 °C. A careful analysis of the microstructure, the crack nucleation and propagation paths, the microtexture, the grain boundary misorientation distribution and the slip traces with straining under constant stress and constant strain rate conditions at high temperatures has led to the following conclusions:

- Crack nucleation take place mostly at colony and grain boundary triple points, under all the high temperature testing conditions investigated, in both, lamellar and duplex microstructures. Intercolony/intergranular cracking is observed to be the dominant failure micromechanism during creep at stresses ranging from 250 to 400 MPa ($0.48\sigma_{max}$-$0.86\sigma_{max}$). In tensile tests at constant strain rates of 10^{-3} s^{-1} and tensile-creep tests at stresses higher than 400 MPa ($0.86\sigma_{max}$) this phenomenon is delayed (i.e., it is evident at higher strains) but still present.

- Colony/grain boundary sliding is active during the secondary creep stage of the mentioned microstructures, leading to stress concentrations and subsequent crack nucleation at triple points and the occurrence of colony/grain boundary cracking. In particular, this mechanism is observed to operate at stresses as high as 400 MPa in lamellar microstructures with a relatively large colony size (CS: 125-194 μm). At stresses higher than 400 MPa colony boundary sliding is only observed during the tertiary stage. The incidence of sliding along the boundaries of equiaxed γ grains in duplex microstructures appears to be particularly high. This is consistent with the relatively small size of these grains (GS: 98 μm).

- The presence of interlamellar secondary cracks is also detected during high temperature deformation of lamellar microstructures, but the importance of this mechanism is lower comparing to colony boundary cracking. Translamellar secondary cracks are rarely observed. Translamellar crack path segments are observed only along the primary crack. It is suggested that they connected intercolonial crack segments upon catastrophic failure. Cracking of B-rich phase reinforcements is also observed at high temperatures. Interlamellar and translamellar cracking is observed during room temperature tensile tests in combination with brittle fracture.

- Interlamellar ledges are observed to appear during the early stages of the tensile test and the tensile-creep tests performed at the highest stresses (425 MPa and 450 MPa, $0.92\sigma_{max}$ and $0.98\sigma_{max}$, respectively), revealing that these areas become weaker with increasing stress. The elevated-temperature tensile experiments show that the minimum stress necessary for the formation of interlamellar ledges is around 370-390 MPa for this material.

- True twin γ/γ interfaces appear to be weaker obstacles to dislocation movement at high temperatures than other types of lamellar boundaries. This points toward the fact that the critical length scale of these materials might be influenced by the distance between non-true twin boundaries and, thus, be larger than the average lamella width.

- A methodology to estimate the relative activity of ordinary and superdislocations and the CRSS values of both slip modes in slip events obeying the Schmid law with respect to the applied stress is proposed.

- A high amount (a minimum of 30-40%) of slip traces corresponding to slip events that do not comply with the Schmid law with respect to the applied stress and which, therefore, are activated by local stresses, are detected in both lamellar and duplex microstructures.

- In duplex microstructures, the activity of slip systems that do not comply with the Schmid law with respect to the applied stress is equally frequent in lamellae and in equiaxed gamma grains. Its presence in the former is consistent with previous findings. In the latter, it may be associated to intragranular slip accommodation of local stresses related to grain boundary sliding.

6 Future work

6. Future work

The following areas of future work are envisioned:

- In order to improve the creep behavior of lamellar and duplex microstructures over a wide stress range, strengthening of both grain/colony boundaries (low stresses) and lamellae interfaces (high stresses) must be achieved by alloying and processing design.

- The origin of the interlamellar ledges observed during creep deformation of lamellar structures at very high stresses must be further understood.

- Isolating the effect of the different microstructural parameters as lamellae spacing, the colony size, the relative orientation of lamellae with respect to the loading axis and the lamellae boundary interfaces on the deformation and fracture mechanisms is timely. This could be achieved, for example, by using nanomechanical testing techniques such as the fabrication of micropillars with controlled microstructures.

- Processing of γ-TiAl alloys by near net shape techniques, such as additive manufacturing processes, should be attempted in order to avoid material losses and post processing machining.

- Further improvements of the *in situ* mechanical testing technique, such as an automatic registration of temperature-load-displacement values would certainly help to speed up data acquisition and processing.

- The combination of *in situ* SEM testing with EBSD with advanced microscopy and imaging techniques such as focused ion beam capabilities (FIB) and digital image correlation (DIC) would allow a more comprehensive analysis of the deformation mechanisms by facilitating 3D examination of selected regions and strain mapping analysis, respectively.

List of figures

Fig. 4.8 XRD pattern of the CCFC material.

Fig. 4.9 (a, b) BSE SEM micrographs at different magnifications showing the CCFC fully lamellar microstructure; (c) colony size distribution.

Fig. 4.10 TEM micrographs of the CCFC lamellae obtained by (a) bright field and (b) dark field imaging. In the latter, the bright areas correspond to the α_2 phase; lamellar spacing distribution corresponding to the (c) γ and (d) $\alpha_2$phase.

Fig. 4.11 BSE SEM micrographs showing the (a, b) CCFC, (c, d) CCAC (e, f) CCOQ and (g, h) CCWQ lamellar microstructures. White arrows point borides.

Fig. 4.12 BSE SEM micrographs showing the CCWQ+850 (a) 1h, (b) 8h; CCWQ+950 (c) 1h, (d) 8h; CCWQ+1150 (e) 1h, (f) 8h. White arrows point gamma grains along colony boundaries.

Fig. 4.13 XRD pattern of the as-atomized prealloyed Ti-45Al-2Nb-2Mn-0.8vol.%TiB_2 powder.

Fig. 4.14 BSE SEM micrographs showing the microstructure of the prealloyed powders: (a) 30 μm diameter particle and (b) 120 μm diameter particle; (c, d) single phase grain clusters present in particles of different sizes.

Fig. 4.15 (a) DTA analysis comparing the prealloyed powder and the CC materials showing different thermal behavior at 600 °C - 750 °C; (b) XRD patterns of prealloyed Ti4522XD powder at 25 °C, 600 °C, 800 °C and 1000 °C.

Fig. 4.16 XRD pattern of as-HIPed material.

Fig. 4.17 (a, b) BSE SEM micrographs of the as-HIPed PM material.

Fig. 4.18 XRD patterns corresponding to the (a) PMFC and (b) PMWQ-850-8h samples.

Fig. 4.19 (a, b) BSE SEM micrographs at different magnifications showing the PMFC fully lamellar microstructure; (c) colony size distribution.

Fig. 4.20 (a, b) BSE SEM micrographs of the refined fully lamellar PMWQ (PMWQ-850-8h) microstructure.

Fig. 4.21 XRD patterns corresponding to the FAHP1, FAHP2, FAHP3, FAHP4 and FAHP5 materials.

Fig. 4.22 BSE SEM micrographs showing the microstructure of the FAHP1 consolidated sample: (a, b) duplex microstructure in the center of the sample; (c) evidence of incomplete sintering at the edges of the sample; (d) Al_3Ti phase in boundary area between the powder particles (edge regions).

Fig. 4.23 BSE SEM micrographs showing the duplex microstructure of the FAHP2 consolidated sample. (a) Evidence of former powder particles; (b) a combination of lamellar colonies and equiaxed grains.

Fig. 4.24 BSE SEM micrographs showing the FAHP3 (a, b) nearly lamellar microstructure and (c) heterogeneous microstructure.

Fig. 4.25 BSE SEM micrographs showing the microstructure of the (a, b) FAHP4 nearly lamellar microstructure; (c, d) FAHP5 fully lamellar microstructure.

Fig. 4.26 Sequence of SE SEM micrographs acquired in the same sample area during RT tensile test at (a) σ = 0MPa, (b) σ =260 MPa, Δl=0.4 mm and (c) σ =450 MPa, Δl=0.6mm showing no

microstructural changes. (d) Stress-displacement curve of the CC-LPT material tested at RT under constant strain rate $\dot{\varepsilon}=10^{-3}s^{-1}$.

Fig. 4.27 (a, b) BSE SEM micrograph of the RT tensile deformed microstructure illustrating translamellar (black arrow) and interlamellar cracking (white arrows) below the fracture surface; (b) SE SEM micrographs of the fracture surface of a sample tested at RT illustrating brittle features including cleavage.

Fig. 4.28 SE SEM micrographs obtained during *in situ* tensile testing at 700 °C. The tensile stress was (a) σ =0 MPa, (b) σ =413MPa, ε~0.2% and (c) σ =481MPa, ε~0.3%. The onset of interlamellar cracking is evident in (c).

Fig. 4.29 SE SEM micrographs obtained during *in situ* tensile testing at 700 °C at σ = 396 MPa and ε~0.2%. (a) Onset of interlamellar cracking in the center of the sample; (b) multiple fracture of boride-rich phase; (c, d) Cracks perpendicular to the vertical loading axis emanating from the edge. (d) Higher magnification image of the area in (c) showing that the cracks propagated through the lamella and colonies. Note that the vertical lines in the (c) and (d) were polishing artifacts present before loading.

Fig 4.30 SE SEM micrograph of the fracture surface after tensile testing at 700 °C. Both ductile (dimples) and brittle (cleavage) features can be observed.

Fig. 4.31 Stress - strain curve corresponding to a tensile test at 700 °C at a constant strain rate of 10^{-3} s^{-1} with indications where micrographs (b-e) were taken. Sequence of SE SEM photomicrographs obtained with increasing time: (b) σ = 374 MPa, ε~0.8%; (c) σ = 459 MPa, ε~1.2%; (d) σ = 433 MPa, ε~1.4 %; (e) σ = 408 MPa, ε~1.6 %. White arrows point toward interlamellar relief, black arrows highlight reinforcement cracks and dashed arrows show the initiation of intercolony cracks.

Fig. 4.32 CC-LPT position versus time creep curve at 250 MPa and 700 °C

Fig. 4.33 Sequence of low magnification SE SEM micrographs obtained during the creep experiment. (a) 0 hours; (b) secondary creep stage, 18.8 hours, ε~2.3%; (c) tertiary creep stage, 23.8 hours, ε~2.6%; (d) tertiary creep stage just prior to fracture, 25.9 hours, ε~3.0%; (e) after fracture.

Fig. 4.34 SE SEM micrographs illustrating the nucleation and growth of the primary crack which led to fracture in the creep test. (a) secondary creep stage, 7.63 hours, ε~2.2%; (b) secondary creep stage, 22.1 hours, ε~2.1%; (c) secondary creep stage, 22.4 hours ε~2.4%; (d) tertiary creep stage 22.8 hours ε~2.5%; (e) tertiary creep stage, 23.1 hours ε~2.6%; (f) 23.4 hours ε~2.6%; (g) tertiary creep stage just prior to fracture, 25.9 hours, ε~3.0%. Note that the crack initiated and grew along colony boundaries.

Fig. 4.35 SE SEM micrographs illustrating the nucleation and growth of a secondary edge crack during creep. (a) secondary creep stage, 5.9 hours, ε~2.2%; (b) secondary creep stage, 6.6 hours, ε~2.4%; (c) secondary creep stage, 22.4 hours ε~2.4%; (d) tertiary creep stage, 22.7 hours ε~2.5%;. Note that the crack tended to propagate along a colony boundary.

Fig. 4.36 SE SEM micrograph of the fracture surface after the creep test. Ductile dimples are dominant although brittle cleavage features are also present.

Fig. 4.37 Sequence of low-magnification SE SEM photomicrographs from a tensile-creep test performed at 300 MPa: (a) Secondary creep stage, 46 hours, ε~0.5%; (b) tertiary creep stage, 72 hours, ε~1.2%; (c) tertiary creep stage, 75 hours, ε~1.4%; (d) tertiary creep stage just prior to fracture, 76 hours, ε~1.5%; (e) after fracture, 76 hours, ε~1.6 %. (f) Corresponding stress - strain curve with indications where micrographs (a-d) were taken.

Fig. 4.38 SE SEM photomicrographs obtained during a creep experiment at 300 MPa (a) Secondary stage, 50h and ε~0.5 % (b) Tertiary stage, 76h and ε~1.5 %. (White arrow points B-rich phase cracking and black arrows point colony boundary cracks).

Fig. 4.39 SE SEM photomicrographs showing the evolution of B-rich phase cracks with increasing time for a tensile-creep test performed at 400 MPa: (a) initial microstructure; (b) secondary stage, 1 h and ε~0.2 %, (c) tertiary stage, 4 h and ε~0.6 %.

Fig. 4.40 SE SEM photomicrographs corresponding to a test at 425 MPa illustrating interlamellar ledges: (a) secondary creep stage, 0.2 hours, ε~0.3%; (b) tertiary creep stage, 2 hours, ε~1.0 %. A colony boundary crack was evident near the middle of the image in (b). (c) Corresponding total strain versus time curve indicating the strains at which the (a) and (b) SEM images were taken.

Fig. 4.41 (a) SE SEM photomicrograph corresponding to a test at 450 MPa illustrating interlamellar ledges during the secondary creep stage (0.33 hours, ε~0.1%). (b) (c) Corresponding total strain versus time curve indicating the strains at which the (a) SEM image was taken.

Fig. 4.42 Nature of the crack propagation paths in specimens deformed under tensile-creep at constant stresses of 300 MPa and 450 MPa: (a) Secondary cracks. (b) Primary crack.

Fig. 4.43 EBSD inverse pole figure maps in the ND and BSE SEM micrographs corresponding to selected areas of the CC microstructure: (a) before and (b, c) after the tensile test at 580 °C, σ_{UTS}= 458 MPa, ε_{max}= 1.3 %; (d) before and (e, f) after the tensile test at 700 °C, σ_{UTS}= 500 MPa, ε_{max}= 1.6 %. (g,h) Comparison of the misorientation distribution histograms in those same areas before and after the tensile tests at 580 °C (g) and at 700 °C (h).

Fig. 4.44 EBSD inverse pole figure maps in the ND and BSE SEM micrographs corresponding to selected areas of the CCFC microstructure: (a) before and (b, c) after the tensile test at 580 °C, σ_{UTS}= 437 MPa, ε_{max}= 1.8 %, including the corresponding inverse pole figures showing the orientation of the tensile axis; (d) before and (e, f) after the tensile test at 700 °C, σ_{UTS}= 498 MPa, ε_{max}= 1.9 %. (g,h) Comparison of the misorientation distribution histograms in those same areas before and after the tensile tests at 580 °C (g) and at 700 °C (h).

Fig. 4.45 Creep curves corresponding to the CCFC and the PMFC microstructures deformed in tension at 700 °C and at a constant stress of 65%σ_{max}

Fig. 4.46 Sequence of SEM micrographs showing the evolution of the PMFC microstructure during creep straining at 700 °C. (a) 0 h; (b) secondary creep stage, 0.3 h, ε ~0.1 %; (c) secondary creep stage, 1.0 h, ε ~1.0 %; (d) secondary creep stage, 7.0 h, ε~5.0 %; (e) tertiary creep stage, 8.3 h, ε~6.2 %; (f) after fracture, 9.7 h, ε_{max}~9.4 %; (g) Corresponding total strain versus time curve indicating the strains at which the (b)-(f) SEM images were taken.

Fig. 4.47 Sequence of SEM micrographs showing the evolution of the surface of the PMFC sample during creep straining at 700°C. (a) secondary creep stage, 0.8 h, ε~0.7 %; (b) secondary creep stage, 1.3 h, ε~1.1 %; (c) secondary creep stage, 2.7 h, ε~2.0 %; (d) secondary creep stage, 5.8 h, ε~4.2 %; (e) secondary creep stage, 7.3 h, ε~4.6 %; (f) tertiary creep stage, 8.6 h, ε~6.8 %; (g) Corresponding total strain versus time curve indicating the strains at which the (a)-(f) SEM images were taken.

Fig. 4.48 Sequence of SEM micrographs showing the evolution of the surface of the CCFC sample during creep straining at 700 °C. (a) 0 h; (b) secondary creep stage, 0.5 h, ε~0.3 %; (c) secondary creep stage, 7.0 h, ε~1.8 %; (d, e) after fracture, 18.1 h, ε_{max}~ 7.0 %; (e) higher magnification SE SEM micrograph from the area pointed with the arrow in (d); (f) Corresponding total strain versus time curve indicating the strains at which the(b)-(e) SEM images were taken.

Fig. 4.49 Schematic drawing showing the variation of $CRSS_s$ with respect to R for a given trace t_i. The shaded areas correspond to ($CRSS_s$,R) pairs for which ordinary (OD) and superdislocations (SD) are active. R_{ci} is a critical R value which marks the transition from ordinary to superdislocation slip.

Fig. 4.50 Relative activity of OD and SD for different R values in the gamma grains of the duplex microstructure (PMFC) during creep at 700 °C and 300 MPa.

Fig. 4.51 Frequency of Group 2 slip traces with increasing strain in the PMFC samples creep tested at 700 °C. Traces belonging to grains and lamellae in the PMFC sample.

List of tables

References

1. M. Yamaguchi, H. Inui, H. Ito. High temperature structural intermetallics. Acta Mater 2000, vol. 48, pp. 307-322.

2. D. G. Morris, M. A. Muñoz-Morris. Intermetallics: past, present and future. Revista de metalurgia 2005, vol. extr., pp. 498-501.

3. D. M. Dimiduk. Gamma titanium aluminide alloys-an assessment within the competition of aerospace structural materials. Mater Sci Eng A 1999, vol. 263, pp. 281-288.

4. E. A. Loria. Gamma titanium aluminides as prospective structural materials. Intermetallics 2000, vol. 8, pp. 1339-1345.

5. G. Lütjering, J.C. Williams. Titanium. Engineering Materials and processes, 2nd edition, Springer -Verlag Berlin Heidelberg, 2007.

6. H. Clemens, S. Mayer. Design, processing, microstructure, properties, and applications of advanced intermetallic TiAl alloys. Adv Eng Mat 2013, vol. 15, n. 4, pp. 191-215.

7. F. Appel, J. D. H. Paul, M. Oehring. γ-Titanium Aluminides. John Wiley & Sons, 2011.

8. F. Appel, U. Brossmann, U. Christoph, S. Eggert, S. Janschek, U. Lorentz, J. Müllauer, M. Oehring, J. D. H. Paul. Recent progress in the development of gamma titanium aluminide alloys. Adv Eng Mat 2000, vol. 2, n. 11, pp. 699-720.

9. Y. W. Kim. Ordered intermetallic alloys, part III: gamma titanium aluminides. JOM 1994, vol. 46, issue 7, pp. 30-39.

10. H. Clemens, H. Kestler. Processing and applications of intermetallic γ-TiAl-based alloys. Adv Eng Mat 2000, vol. 2, pp. 551-570.

11. F. Appel, M. Oehring, R. Wagner. Novel design concepts for gamma-base titanium aluminide alloys. Intermetallics 2000, vol. 8, pp. 1283-1312.

12. K. Kothari, R. Radhakrishnan, N. M. Wereley. Advances in gamma titanium aluminides and their manufacturing techniques. Progress in Aerospace Sciences 2012, vol. 55, pp. 1-16.

13. W. J. Zhang, B. V. eddy, S. C. Deevi. Physical properties of TiAl base alloys. Scr Mat 2001, vol. 45, pp. 645-651.

14. B. P. Bewlay, Presentation at the European Symposium of superalloys and their applications, Wildbad Kreuth, Germany, 2010.

15. H. Clemens, W. Smarsly. Light-Weight Intermetallic titanium aluminides – Status of research and development. Adv Mater Res 2011, vol. 278, pp. 551-556.

16. H. R. Ogden, D. J. Maykuth, W. L. Finlay, R. I. Jaffee. Constitution of titanium-aluminum alloys. Transactions of the American Institute of Mining and and Metallurgical Engineers 1951, vol. 191, issue 12, pp. 1150–1155.

17. E. S. Bumps, H. D. Kessler, M. Hansen. Titanium-aluminum system. Transactions of the American Institute of Mining and Metallurgical Engineers 1952, vol. 194, issue 6, pp. 609-614.

18. J. L. Murray. Calculation of the titanium-aluminium phase diagram. Met Mat Trans A 1988, vol. 19, pp. 243-247.

19. J. C. Mishurda, J. C. Lin, A. Chang, J. H. Perepezko. Titanium aluminide alloys between the compositions Ti_3Al and TiAl. Mat Res Soc Symp Proc 1989, vol. 133, pp. 57-90.

20. J. C. Shuster, M. Palm. Reassessment of the binary aluminium-titanium phase diagram. Journal of phase equilibria and diffusion 2006, vol. 27, n. 3, pp.255-277.

21. U. Hecht, D. Daloz, J. Lapin, A. Drevermann, V. Y. Witusiewicz, J. Zollinger. Solidification of TiAl-based alloys. Mater Res Soc Symp Proc 2009, vol. 1128, pp. 79-90.

22. J. J. Valencia, C. McCullough, C. G. Levi, R. Mehrabian. Solidification microstructure of supercooled Ti-Al alloys containing intermetallic phases. Acta Metall 1989, vol. 37, n. 9, pp. 2517-2530.

23. R. Kainuma, Y. Fujita, H. Mitsui, I. Ohnuma, K. Ishida. Phase equilibria among α(hcp), β(bcc) and γ ($L1_0$) phases in Ti-Al base ternary alloys. Intermetallics 2000, vol. 8, pp. 855-867.

24. M. E. Hyman, C. McCullogh, J. J. Valencia, C. G. Levi, R. Mehrabian. Microstructure evolution in TiAl alloys with B additions: conventional solidification. Met Mat Trans A 1989, vol. 20, pp. 1847-1859.

25. Y. L. Hao, R. Yang, Y. Y. Cui, D. Li. The influence of alloying on the $\alpha_2/(\alpha_2+\gamma)/\gamma$ phase boundaries in TiAl based systems. Acta Mater 2000, vol. 48, pp. 1313-1324.

26. A. Denquin, S. Naka. Phase transformation mechanisms involved in two phase TiAl based alloys. I. Lamellar structure formation. Acta Mater 1996, vol. 44, n.1, pp. 343-352.

27. S. Zghal, S. Naka, A. Couret. A quantitative TEM analysis of the lamellar microstructure in TiAl based alloys. Acta Mater 1997, vol. 45, n. 7, pp. 3005-3015.

28. S. R. Dey, A. Hazotte, E. Bouzy. Crystallography and phase transformation mechanisms in TiAl-based alloys – A synthesis. Intermetallics 2009, vol. 17, pp. 1052-1064.

29. S. Zghal, M. Thomas, S. Naka, A. Finel, A. Couret. Phase transformations in TiAl based alloys. Acta Mater 2005, vol. 53, pp. 2653-2664.

30. A. Denquin, S. Naka. Phase transformation mechanisms involved in two phase TiAl based alloys. I. Discontinuous coarsening and massive-type transformation. Acta Mater 1996, vol. 44, pp. 353-365.

31. D. Veeraraghavan, P. Wang, V.K. Vasudevan. Nucleation kinetics of the $\alpha \rightarrow \gamma_M$ massive transformation in a Ti-47.5 at.% Al alloy. Acta Mater 2003, vol. 51, pp. 1721-1741.

32. G. W. Quin, K. Oikawa, Z. M. Sun, S. Sumi, T. Ikeshoji, J. J. Wang, S.W. Guo, S. M. Hao. Discontinuous coarsening of the lamellar structure of γ-TiAl based intermetallic alloys and its control. Met Mat Trans A 2001, vol. 32, pp. 1927-1938.

33. D. Hu, A.J. Huang, X. Wu. On the massive phase transformation regime in TiAl alloys: The alloying effect on massive/lamellar competition. Intermetallics 2007, vol. 15, pp. 327-332.

34. S.R. Dey, E. Bouzy, A. Hazotte. EBSD characterization of massive γ nucleation and growth in a TiAl-based alloy. Intermetallics 2006, vol. 14, pp. 444-449.

35. D. Hu, A.J. Huang, X. Wu. TEM characterisation of Widmanstätten microstructures in TiAl-based alloys. Intermetallics 2005, vol. 13, pp. 211-216.

36. S.R. Dey, A. Hazotte, E. Bouzy, S. Naka. Development of Widmanstätten laths in a near-γ TiAl alloy. Acta Mater 2005, vol. 53, pp. 3783-3794.

37. S.R. Dey, E. Bouzy, A. Hazotte. Features of feathery γ structure in a near-γ TiAl alloy. Acta Mater 2008, vol. 56, pp. 2051-2062.

38. T. T. Cheng, M. H. Loretto. The decomposition of the beta phase in Ti-44Al-8Nb and Ti-44Al-4Nb-4Zr-0.2Si alloys. Acta Mater 1998, vol. 46, pp. 4809-4819.

39. S. R. Dey. Crystallography and phase transformation mechanisms in TiAl-based intermetallic alloys. Ph.D. Thesis, University Paul-Verlaine Metz, 2006.

40. M. J. Blackburn, Technology and application of Titanium (Eds R. I. Jaffee and N. E. Promisel), Pergamon Press, Oxford, 1970.

41. C. Zambaldi. Micromechanical modeling of γ-TiAl based alloys. Ph.D. Thesis, RWTH Aachen University, 2010.

42. C. Zambaldi, S. Zaefferer, S. I. Wright. Characterization of order domains in γ-TiAl by orientation microscopy based on electron backscatter diffraction. J Appl Cryst 2009, vol. 42, pp. 1092-1101.

43. H. Inui, M. H. Oh, A. Nakamura, M. Yamaguchi. Room-temperature tensile deformation of polysinthecally twinned (PST) crystals of TiAl. Acta Metall Mater 1992, vol. 40, n. 11, pp. 3095-3104.

44. Y. Yamamoto, M. Takeyama. Physical metallurgy of single crystal gamma titanium aluminide alloys: orientation control and thermal stability of lamellar microstructure. Intermetallics 2005, vol. 13, pp. 965-970.

45. S. R. Dey, A. Morawiec, E. Bouzy, A. Hazotte, J. J. Fundenberger. A technique for determination of γ/γ interface relationships in a (α_2+γ) TiAl base alloy using TEM Kikuchi patterns. Materials Letters 2006, vol. 60, pp. 646-650.

46. S. R. Dey, A. Hazotte, E. Bouzy. Multiscale γ variant in a quaternary near-γ Ti-Al alloy. Phil Mag A 2006, vol. 86, pp. 3089-3112.

47. M. Kanani, R. Janisch, A. Hartmaier. In preparation.

48. Y.W. Kim. Intermetallic alloys based on gamma titanium aluminide. Journal of Metallurgy 1989, vol. 41, pp.24-30.

49. Y.W. Kim. Effects of microstructure on the deformation and fracture of γ-TiAl alloys. Mater Sci Eng A 1995, vol.192/193, pp. 519-533.

50. S. C. Huang, E. L. Hall. Plastic deformation and fracture of binary TiAl-base alloys. Metall Trans A 1991, vol.22, pp.427-439.

51. S.C. Huang, N.Y. Latham. United States Patent 4879092, 1989.

52. M. Takeyama, Y. Kato, M. Kikuchi, in Titanium 95 (Eds: P. A. Blekinsop, W. J. Evans, H. M. Flower), The Institute of Materials, London, England 1996, p. 294.

53. A. Suzuki, M. Takeyama, T. Matsuo. Transmission electron microscopy on the phase equilibria among β, α and α_2 phases in Ti–Al binary system. Intermetallics 2002, vol. 10, pp. 915-924.

54. R. Kainuma, Y. Fujita, H. Mitsui, I. Ohnuma, K. Ishida. Phase equilibria among α (hcp), β (bcc) and γ ($L1_0$) phases in Ti–Al base ternary alloys. Intermetallics 2000, vol. 8, pp. 855-867.

55. H. Nakamura, M. Takeyama, W. Kin, Y. Yamabe, M. Kikuchi, in SAMPE Symposium on Intermetallic Compounds for High-Temperature Structural Applications (Eds: M. Yamaguchi, H. Fukutomi), Society for the Advancement of Materials and Process Engineering, Chiba, Japan 1993, p. 997.

56. L. Christodoulou, J. M. Brupbacher. Metal matrix composites. Materials edge Nov-Dec, 1990, pp. 29-33.

57. K. S. Kumar, J. D. Whittenberger. Discontinuously reinforced intermetallic matrix composites via XD synthesis. Mat Sc Tech 1992, vol. 8, pp. 317-330.

58. K. S. Kumar, J. A. S. Green, D. E. Larsen, L. D. Kramer. XD Titanium aluminide composites. Adv Mat and Processes 1995, vol. 4, pp. 35-38.

59. Y.H. Wang, J.P. Lin, Y.H. He, Y.L. Wang, and G.L. Chen. Microstructural characteristics of Ti–45Al–8.5Nb/TiB_2 composites by powder metallurgy. Journal of Alloys and Compounds 2009, vol. 468, pp. 505-511.

60. D.E. Larsen, S. Kampe, L. Christodoulou. Effect of XD^{TM} TiB_2 volume fraction on the microstructure of a cast near-gamma titanium aluminide alloy. Mater Res Soc Symp Proc 1990, vol. 194, pp. 285-292.

61. C. Mercer, J. Lou, S.M. Allameh, and W.O. Soboyejo. Effects of temperature on the fatigue crack growth behavior of cast gamma-based titanium aluminides. Metall Mater Trans A 2001, vol. 32, pp. 2781-2794.

62. W. E. Voyce, M. Henderson, E.F.J. Shelton, X. Wu. Gamma Titanium Aluminide TNB. Intermetallics 2005, vol. 15, pp. 959-964.

63. H. Clemens, W. Wallgram, S. Kremmer, V. Güther, A. Otto, A. Bartels. Design of Novel β-Solidifying TiAl Alloys with Adjustable β/B2-Phase Fraction and Excellent Hot-Workability. Adv Eng Mater 2008, vol. 10, pp. 707-713.

64. E. A. Loria. Quo vadis gamma titanium aluminide. Intermetallics 2001, vol. 9, pp. 997-1001.

65. X. Wu. Review of alloy and process development of TiAl alloys. Intermetallics 2006, vol. 14, pp. 1114-1122.

66. R. Gerling, H. Clemens, F. P. Schimasky. Power metallurgical processing of intermetallic gamma titanium aluminides. Adv Eng Mat 2004, vol. 6, n. 1-2, pp. 23-37.

67. C. Yang, D. Hu, A. Huang, M. Dixon. Microstructures and tensile properties of hot isostatic pressed Ti4522XD powders. Intermetallics 2013, vol. 32, pp. 64-71.

68. K. Matsugi, N. Ishibashi, T. Hatayama, O. Yanagisawa. Microstructure of spark sintered titanium-aluminide compacts. Intermetallics 1996, vol. 4, pp. 457-467.

69. G. Molénat, M. Thomas, J. Galy, A. Couret. Application of spark plasma sintering to titanium aluminide alloys. Adv Eng Mater 2007, vol. 9, n. 8, pp. 667-669.

70. T. Voisin, L. Durand, N. Karnatak, S. Le Gallet, M. Thomas, Y. Le Berre, J. F. Castagné, A. Couret. Temperature control during spark plasma sintering and application to up-scaling and complex shaping. Journal of Materials Processing and Technology 2013, vol. 213, pp. 269-278.

71. L. E. Murr, S. M. Gaytan, D. A. Ramirez, E. Martinez, J. Hernandez, K. N. Amato, P. W. Shindo, F. R. Medina, R. B. Wicker. Metal Fabrication by Additive Manufacturing Using Laser and Electron Beam Melting Technologies, Journal of Materials Science & Technology 2012, vol. 28, issue 1, pp. 1-14.

72. L.E. Murr, S.M. Gaytan, A. Ceylan, E. Martinez, J.L. Martinez, D.H. Hernandez, B.I. Machado, D.A. Ramirez, F. Medina, S. Collins, R.B. Wicker. Characterization of titanium aluminide alloy components fabricated by additive manufacturing using electron beam melting. Acta Mater 2010, vol. 58, issue 5, pp. 1887-1894.

73. S. Biamino, A. Penna, U. Ackelid, S. Sabbadini, O. Tassa, P. Fino, M. Pavese, P. Gennaro, C. Badini. Electron beam melting of Ti–48Al–2Cr–2Nb alloy: Microstructure and mechanical properties investigation. Intermetallics 2011, vol. 19, issue 6, pp, 776-781.

74. L. Loeber, U. Kuehn, J. Risse, F. P. Schimansky, J. Eckert. Selective laser melting of titanium aluminide with different pre-heating techniques. Gamma TiAl Alloy Technology 2012 workshop, Beijing, China (June 5-9, 2012).

75. A. Royer, S. Vasseur. Casting, Metals Handbook, vol.15, 9th edn (ed chairman D.M. Stefanescu), ASM International, Metal Park, OH, pp. 296.

76. Y. Su, J. Guo, S. Wu,W. Sheng, H. Fu, H. Modeling generation mechanisms of defects during permanent mould centrifugal casting process of TiAl alloy exhaust valve. Mat Sc Tech 2011, vol. 27, n. 1, pp. 246-251.

77. S. Wen-bin. Filling and solidification of TiAl melt in centrifugal casting. Trans Nonferrous Met Soc China 2006, vol. 16, pp. 719-722.

78. J. Aguilar, A. Schievenbusch, O. Kättliz. Investment casting technology for production of TiAl low pressure turbine blades – process engineering and parameters analysis. Intermetallics 2011, vol. 19, pp. 757-761.

79. K. Liu, Y. C. Ma, M. Gao, G. B. Rao, Y. Y. Li, K. Wei, X. Wu, M. H. Loretto. Single step centrifugal casting TiAl automotive valves. Intermetallics 2005, vol. 13, pp. 925-928.

80. P. X. Fu, X. H. Kang, Y. C. Ma, K. Liu, D. Z. Li, Y. Y. Li. Centrifugal casting of TiAl exhaust valves. Intermetallics 2008, vol. 16, pp. 130-138.

81. L. M. Hsiung, T. G. Nieh. Microstructures and properties of powder metallurgy TiAl alloys. Mat Sc Eng A 2004, vol. 364, pp. 1-10.

82. Y. Liu, B. Huang, Y. He, K. Zhou. Processing TiAl based alloy by elemental powder metallurgy. Journal of Materials Science and Technology 2000, vol. 16, n. 6.

83. Y. H. Wang, J. P. Lin, Y. H. He, Y. L. Wang, G. L. Chen. Microstructural characteristics of Ti-45Al-8.5Nb/TiB_2 composites by powder metallurgy. Journal of alloys and compounds 2009, vol. 468, pp. 505-511.

84. F. Pyczak, F. Appel, W. Limberg, U. Lorenz, M. Oehring, J. Paul, F. P. Schimansky. Novel Processing Techniques for γ-TiAl Alloys. Mat Sc Forum 2011, vol. 690. pp. 145-148.

85. O. W. Stenzel, G. Sick, M. Hohmann, German Patent DE 4011 392A1, 1990.

86. M. Hohman, N. Ludwig, German Patent DE 4102 101 A1, 1991.

87. C. Yang, D. Hu, A. Huang, M. Dixon. Solidification and grain refinement in Ti45Al2Mn2Nb1B subjected to fast cooling. Intermetallics 2013, vol. 32, pp. 64-71.

88. C. Suryanarayana. Mechanical alloying and milling. Progress in material science 2001, vol. 46, pp. 1-184.

89. H. (Sam) Froes, C. Suryanarayana, K. Russell, C.-G. Li. Synthesis of intermetallics by mechanical alloying. Mat Sc Eng A 1995, vol. 192-193, pp.612-623.

90. C.C. Koch, J. D. Whittenberger. Mechanical milling/alloying of intermetallics. Intermetallics 1996, vol. 4, pp. 339-355.

91. L. Lu, M. O. Lai, F. H. Froes. The mechanical alloying of titanium aluminides. JOM 2002, vol. 4, issue 2, pp. 62-64.

92. P. G. Esteban, E. Gordo, E.M. Ruiz-Navas. Influence of high-energy milling and sintering cycle on obtaining TiAl from elemental Ti and Al powders. Mat Sc Forum 2007, vol. 534-536, pp.813-816.

93. J. Guyon, A. Hazotte, J.P. Monchoux, E. Bouzy. Effect of powder state on spark plasma sintering of TiAl alloys. Intermetallics 2013, vol. 34, pp. 94-100.

94. L. Zhao, J. Beddoes, P. Au, W. Wallace. Evaluations of P/M gamma titanium aluminides. Adv Perf Mat 1997, vol. 4, pp. 421-434.

95. J. Beddoes, W. Wallace, M. C. de Malherve. Densification of γ-TiAl powder by hot isostatic pressing. The international journal of powder metallurgy 1992, vol. 28, N. 3, pp. 313-325.

96. U. Habel, B. J. McTiernan. HIP temperature and properties of a gas-atomized γ-titanium aluminide alloy. Intermetallics 2004, vol. 12, pp.63-68.

97. L. Zhao, J. Beddoes, D. Morphy, W. Wallace. Microstructure and mechanical properties of a PM TiAl-W alloy processed by hot isostatic pressing. Mat Sc Eng A 1995, vol. 192/193, pp. 957-964.

98. J. Beddoes, L. Zhao, P. Au, W. Wallace: The brittle-ductile transition in HIP consolidated near γ-TiAl + W and TiAl+ Cr powder alloys. Mat Sc Eng A, 1995, vol. 192/193, pp. 324-332.

99. K. Kotheri, R. Radhakrishnan, N. M. Wereley, T. S. Sudarshan. Microstructure and mechanical properties of consolidated gamma titanium aluminides. Powder Metallurgy 2007, vol. 50, n. 1, pp.21-27.

100. B. Mei, Y. Miyamoto. Preparation of Ti-Al intermetallic compounds by spark plasma sintering. Metal Mater Trans A 2001, vol. 32, pp. 843-847.

101. A. Couret, G. Molénat, J. Galy, M. Thomas. Microstructures and mechanical properties of TiAl alloys consolidated by spark plasma sintering. Intermetallics 2008, vol. 16, pp. 1134-1141.

102. H. Jabbar, A. Couret, L. Durand, J. P. Monchoux. Identification of microstructural mechanisms during densification of a TiAl alloy by spark plasma sintering. Journal of alloys and compounds 2011, vol. 509, pp. 9826-9835.

103. H. Jabbar, J. P. Monchoux, M. Thomas, A. Couret. Microstructures and deformation mechanisms of a G4 TiAl alloy produced by spark plasma sintering. Acta Materialia 2011, vol. 59, pp. 7574-7585.

104. J. S. Luo, T. Voisin, J. P. Monchoux. Refinement of lamellar microstructures by boron incorporation in GE-TiAl alloys processed by spark plasma sintering. Intermetallics 2013, vol. 36, pp. 12-20.

105. H. Jabbar, J. P. Monchoux, F. Houdellier, M. Dollé, F. P. Schimansky, F. Pyczak, M. Thomas, A. Couret. Microstructure and mechanical properties of high Nb containing TiAl alloys elaborated by spark plasma sintering. Intermetallics 2010, vol. 18, pp. 2312-2321.

106. H. Jabbar, J. P. Monchoux, M. Thomas, F. Pyczak, A. Couret. Improvement of the creep properties of TiAl alloys densified by spark plasma sintering. Intermetallics 2014, vol. 46, pp. 1-3.

107. G. Molénat, L. Durand, J. Galy, A. Couret: Temperature control in spark plasma sintering: An FEM approach. Journal of Metallurgy 2010, vol. 2010, pp.1-9.

108. L. Bolzoni. Diseño y procesado de aleaciones de Titanio mediante técnicas pulvimetalúrgicas avanzadas. Ph.D. Thesis, Universidad Carlos III de Madrid, 2011.

109. I. Montealegre Meléndez. Development of Titanium based composites via powder metallurgy. Ph.D. Thesis, Tecnische Universität Wien, 2009.

110. Z. A. Munir, U. Anselmi-Tamburini, M. Ohyanagi. The effect of electric field and pressure on the synthesis and consolidation of materials: A review of the spark plasma sintering method. J Mater Sci 2006, vol. 41, pp. 763-777.

111. G. F. Taylor, US Patent No. 1,896,854, 1933.

112. C. S. Barrett, T. B. Massalski. Structure of metals, 3rd rev. edn. P. 406. Pergamon press, Oxford, 1980.

113. T. Fujiwara, A. Nakamura, M. Hosomi, S. R. Nishitani, Y. Shirai, M. Yamaguchi. Deformation of polysynthetically twinned crystals of TiAl with a nearly stoichiometric composition. Phil Mag A 1990, vol. 61, pp. 591-606.

114. H. Inui, M. H. Oh, A. Nakamura, M. Yamaguchi. Room temperature tensile deformation of polysynthecally twinned (PST) crystals of TiAl. Acta Metall Mater 1992, vol. 40, pp. 3095-3104.

115. M. Hazzledine, B. K. Kad. Yield and fracture of lamellar γ/α_2 TiAl alloys. Mater Sci Eng A 1995, vol. 192/193, pp. 340-346.

116. C. Zambaldi, F. Roters, D. Raabe. Analysis of the plastic anisotropy and pre-yielding of (γ/α_2)-phase titanium aluminide microstructures by crystal plasticity simulation. Intermetallics 2011, vol. 19, pp. 820-827.

117. H. Mecking, C. Hartig, U. F. Kocks. Deformation modes in γ-TiAl as derived from single crystal yield surface. Acta mater 1996, vol. 44, pp. 1309-1321.

118. R. Lebensohn, H. Uhlenhut, C. Hartig, H. Mecking. Plastic flow of γ-TiAl based polysynthecally twinned crystals: micromechanical modeling and experimental validation. Acta mater 1998, vol. 46, pp. 4701-4709.

119. H. Inui, M. Matsumuro, D. H. Wu, M. Yamaguchi. Temperature dependence of yield stress, deformation mode and deformation structure in single crystals of TiAl (Ti-56 at.% Al). Phil Mag A 1997, vol. 75, pp. 395-423.

120. M. Aindow, K. Chaudhuri, S. Das, H. L. Fraser. On the influence of stoichiometry and purity on the deformation mechanisms in the intermetallic compound TiAl. Scr Metall Mater 1990, vol. 24, pp. 1105-1108.

121. B. K. Kad, H. L. Fraser. Effects of oxygen on the deformation behaviour in single-phase γ-TiAl alloys. Phil Mag Lett 1994, vol. 70, pp. 211-220.

122. G. E. Dieter, Mechanical Metallurgy, McGraw Hill, UK, 1988.

123. M. Zupan, K. J. Hemker. Yielding behavior of aluminum-rich single crystalline γ-TiAl. Acta Mater 2003, vol. 51, pp. 6277-6290.

124. M. A. Stucke, V. K. Vasudevan, D. M. Dimiduk. Deformation behavior of [001] Ti-56Al single crystals. Mater Sci Eng A 1995, vol. 192/193, pp. 111-119.

125. T. Kawabata, T. Kanai, O. Izumi. Positive temperature dependence of the yield stress in TiAl $L1_0$ type superlattice intermetallic compound single crystals at 293–1273 K. Acta Metall 1985, vol. 33, pp. 1355-1366.

126. S. H. Whang, Q. Feng, Z. M. Wang. Deformation characteristics and dislocation structures in single phase gamma titanium aluminides. Intermetallics 2000, vol. 8, pp. 531-537.

127. L. W. Song, Y. Li, Y. Ma, S. K. Gong. High temperature creep behavior and mechanisms of TiAl-based intermetallics. Rare metals 2011, vol. 30, pp. 323-325.

128. M.E. Kassner, M.T. Pérez-Prado. Fundamentals of creep in metals and alloys. Elsevier Oxford (UK), 2004.

129. T. A. Parthasarathy, P. R. Subramanian, M. G. Mendiratta, D. M. Dimiduk. Phenomenological observations of lamellar orientations effects on the creep behavior of Ti-48at.%Al PST crystals. Acta Mater 2000, vol. 48, pp. 541-551.

130. W.J. Zhang, S.C. Deevi. Analysis of the minimum creep rates of TiAl alloys. Mater Sci Eng A 2003, vol. 362, pp. 280-291.

131. A. Gorzel, G. Sauthoff. Diffusion creep of intermetallic TiAl alloys. Intermetallics 1999, vol. 7, pp. 371-380.

132. W. J. Zhang, S. C. Deevi. The controlling creep processes in TiAl alloys at low and high stresses. Intermetallics, 2002, vol.10, pp. 603-611.

133. J. Beddoes, W. Wallace, L. Zhao. Current understanding of creep behavior of near gamma-titanium aluminides. Int Mater Reviews 1995, vol. 40, pp. 197-217

134. H. Zhu, D.Y. Seo, K. Mayurama, P. Au. Effect of lamellar spacing on Microstructural instability and creep behavior of a lamellar TiAl alloy. Scr Mater 2006, vol. 54, pp. 1979-1984.

135. H. Zhu, D.Y. Seo, K. Mayurama, P. Au. Effect of microstructure on creep deformation of 45XD TiAl alloy at low and high stresses. Mater Sc Eng A 2008 vol. 483-484, pp. 533-536.

136. H. Zhu, D.Y. Seo, K. Maruyama, P. Au. Effect of microstructural stability on creep behavior of 47XD TiAl alloys with fine-grained fully lamellar structure. Scr Mater 2005, vol. 52, pp.45-50.

137. D. Peter, G. B. Viswanathan, M. F. X. Wagner, G. Eggeler. Grain-boundary sliding in a TiAl alloy with fine-grained duplex microstructure during 750 °C creep. Mat Sci Eng A 2009, vol. 510-511, pp. 359-363.

138. D. Peter, G.B. Viswanathan, M.F.-X. Wagner, G. Eggeler. Grain-boundary sliding in a TiAl alloy with fine-grained duplex microstructure during 750 °C creep. Mater Sci Eng A 2009, vol. 510–511, pp. 359-363.

139. R.J. DiMelfi. Grain boundary sliding and its relation to ductility and fracture in fine-grained polycrystalline materials with a particular focus on γ-TiAl. Mater Sci Eng A 1997, vol. 237, issue 2, pp. 141-149.

140. F. Appel, J. D. H. Paul, M. Oehring. Phase transformations during creep of a multiphase TiAl-based alloy with a modulated microstructure. Mat Sci Eng A 2009, vol. 510-511, pp. 342-349

141. T.A. Parthasarathy, M.G. Mendiratta, D.M. Dimiduk. Observations on the creep behavior of fully lamellar polycrystalline TiAl: Identification of critical effects. Scr Mat 1997, vol. 37, pp. 315-321.

142. T.A. Parthasarathy, M. Keller, M.G. Mendiratta. The effect of lamellar lath spacing on the creep behavior of Ti-47at.%Al. Scr Met 1998, vol. 38, pp. 1025-1031.

143. J. Beddoes, L. Zhao, P. Au, D. Dudzinski, J. Triantafillou. Structural Intermetallics. Warrendale, PA. The Minerals Metals and Materials Society 1997. pp. 109-18.

144. W.R. Chen, J. Triantafillou, J. Beddoes, L. Zhao. Effect of fully lamellar morphology on creep of a near –TiAl intermetallic. Intermetallics 1999, vol. 7, pp. 171–178.

145. K. Maruyama, R. Yamamoto, H. Nakakuki, N. Fujitsuna. Effects of lamellar spacing, volume fraction and grain size on creep strength of fully lamellar TiAl alloys. Mat Sc Eng A 1997, vol. 239/240, pp. 419–428.

146. C.E. Wen, K. Yasue, J.G. Lin, Y.G. Zhang, C.Q. Chen. The effect of lamellar spacing on the creep behavior of a fully lamellar TiAl alloy. Intermetallics 2000, vol. 8, pp. 525–529.

147. C.J. Boehlert, D.M. Dimiduk, K.J. Hemker. The phase evolution, mechanical behavior, and microstructural instability of a fully-lamellar Ti–46Al(at.%) alloy. Scr Mater 2002, vol. 46, pp. 259-267.

148. P.M. Hazzledine, D.M. Dimiduk: Structural Intermetallics. Warrendale, PA. The Minerals, Metals, and Materials Society 1997, pp. 481–487.

149. J.N. Wang, K. Xie. Refining of coarse lamellar microstructure of TiAl alloys by rapid heat treatment. Intermetallics 2000, vol. 8, pp. 545–548.

150. F. Appel, U. Christoph, M. Oehring. Creep deformation in two-phase titanium aluminide alloys. Mat Sc Eng A, 2002, vol. 329-331, pp.780-787.

151. K. S. Chan and Y. W. Kim. Effects of lamellae spacing and colony size on the fracture resistance of a fully-lamellar TiAl alloy. Acta Metal Mater 1995, vol. 43, pp. 439-451.

152. Y.H. Lu, Y.G. Zhang, L.J. Qiao, Y.B. Wang, C.Q. Chen, W.Y. Chu. The fracture mechanism of a fully lamellar γ-TiAl alloy through in-situ SEM observation. Intermetallics, 2000, vol. 8, pp. 1443-1445.

153. D. Hongsheng, N. Ge, C. Ruirun, G. Jingjie, F. Hengzhi. High temperature deformation behaviors of polysynthetically twinned (PST) Ti–47Al–2Cr–2Nb alloy. Mat Sc Eng A 2012, vol. 558, pp. 747-754.

154. H. Zhu, D. Y. Seo, K. Maruyama, P. Au. Effect of initial microstructure on microstructural instability and creep resistance of XD TiAl alloys. Metall Mater Trans A, vol. 37, pp. 2006-3149.

155. R. Cao, Y. Z. Lin, D. Hu, J. H. Chen. Fracture behavior of a TiAl alloy under various loading modes. Eng Fract Mech 2008, vol. 75, pp. 4343-4362.

156. http://www.geaviation.com

157. http://www.rolls-royce.com

158. W. Voice. The future use of gamma titanium aluminides by Rolls-Royce. Aircraft Engineering and Aerospace Technology 1999, vol. 71, issue 4, pp. 337-340.

159. T. Tetsui. Gamma titanium aluminides for non-aerospace applications. Current opinion in solid state and materials science 1999, vol. 4, pp. 243-248.

160. T. Tetsui, S Ono. Endurance and composition and microstructure effects on endurance of TiAl used in turbochargers. Intermetallics 1999, vol. 7, issue 6, pp. 689-697.

161. V. Güther, M. Achtermann, J. Klose. Progress in the Industrialization of titanium aluminides. Intermetallics 2013 conference, Educational center Kloster Banz, Germany.

162. H. Zhu, T. Wei, D. Carr, R. Harrison, L. Edwards, W. Hofferlner, D. Seo, K. Maruyama. Assesment of titanium aluminides alloys for high temperature nuclear structural applications. JOM 2012, vol. 64, pp. 1418-1424.

163. G. Dehm, J.M. Howe and J. Zweck. Front Matter, *in situ* Electron Microscopy: Applications in Physics, Chemistry and Materials Science, Wiley-VCH Verlag GmbH & Co. KGaA, Weinheim, Germany, 2012.

164. F. Banhart. *In situ* electron microscopy at high resolution, Singapore, World Scientific Publishing Company, 2008.

165. E. P. Butler, K. F. Hale. Dynamic Experiments in the Electron Microscope, in Practical Methods in Electron Microscopy. Vol. 9, ed. A. M. Glauert. Elsevier, Amsterdam, 1981.

166. D.E. Newbury, D.B. Williams. The electron microscope: the materials characterization tool of the millennium, Acta Mater 2000, vol. 48, issue 1, pp. 323-346.

167. E. A. Stach, Real-time observations with electron microscopy, Materials Today 2008, vol. 11, Supplement, pp. 50-58.

168. D. Caillard and A. Couret. *In situ* deformation experiments: technical aspects. In Encyclopedia of Materials: Science and Technology (Second Edition), edited by K.H. Jürgen

Buschow, Robert W. Cahn, Merton C. Flemings, Bernhard Ilschner, Edward J. Kramer, Subhash Mahajan and Patrick Veyssière, Elsevier, Oxford, 2006.

169. A. Couret and D. Caillard. *In situ* straining experiments: Examples of Results, In Encyclopedia of Materials: Science and Technology (Second Edition), edited by K.H. Jürgen Buschow, Robert W. Cahn, Merton C. Flemings, Bernhard Ilschner, Edward J. Kramer, Subhash Mahajan and Patrick Veyssière, Elsevier, Oxford, 2006.

170. J. Ye, R. K. Mishra, A. K. Sachdev, A. M. Minor. *In situ* TEM compression testing of Mg and Mg–0.2wt.% Ce single crystals. Scripta Mater 2011, vol. 64, issue 3, pp. 292-295.

171. A. M. Beese, D. Papkov, S. Li, Y. Dzenis, H. D. Espinosa. *In situ* transmission electron microscope tensile testing reveals structure–property relationships in carbon nanofibers, 2013. Carbon, vol. 60, pp. 246-253.

172. D. Kiener, P. Hosemann, S. A. Maloy, A. M. Minor. *In situ* nano-compression testing of irradiated copper. Nature Materials 2012, vol. 10, pp. 608-613.

173. W. Roberts, B. Lehtinen, K. E. Easterling. An *in situ* sem study of void development around inclusions in steel during plastic deformation, Acta Metall 1976, vol. 24, issue 8, pp. 745-758.

174. E. A. Torres, A. J. Ramirez. *In situ* scanning electron microscopy. Science and Technology of Welding and Joining 2011, vol.16, n.1, pp. 68-78.

175. R. Podor, J. Ravaux, H. P. Brau. *In Situ* Experiments in the Scanning Electron Microscope Chamber, Scanning Electron Microscopy, Dr. Viacheslav Kazmiruk (Ed.), 2012.

176. E. A. Torres. Development of SEM *in situ* high temperature deformation test and its application to the study of ductility dip cracking phenomenon on Ni-base alloys. MSc dissertation, Campinas State University, Campinas, Brazil, 2008.

177. A.J. Schwartz, M. Kumar, B.L. Adams, D.P. Field. Eds. Electron Backscatter Diffraction in Materials Science 2, Springer, New York, 2009.

178. P. Chen, S.C. Mao, Y. Liu, F. Wang, Y.F. Zhang, Z. Zhang, X.D. Han. *In situ* EBSD study of the active slip systems and lattice rotation behavior of surface grains in aluminum alloy during tensile deformation. Mater Sci Eng A 2013, vol.580, pp. 114-124.

179. G. G. E. Seward, S. Celotto, D. J. Prior, J. Wheeler, R. C. Pond RC. *In situ* SEM-EBSD observations of the hcp to bcc phase transformation in commercially pure titanium. Acta Mater 2004, vol. 52, pp. 821-832.

180. N. Bozzolo, S. Jacomet, R.E. Logé. Fast *in situ* annealing stage coupled with EBSD: A suitable tool to observe quick recrystallization mechanisms. Materials Characterization 2012, vol. 70, pp. 28-32.

181. L. Muscariello, F. Rosso, G. Marino, A. Giordano, M. Barbarisi, G. Cafiero, A. Barbarisi. A Critical Overview of ESEM Applications in the Biological Field. Journal of Cellular Physiology 2005, vol. 205, pp. 328–334.

182. R. Leary, R. Brydson. Characterisation of ESEM conditions for specimen hydration control. Journal of Physics 2010, c*onference Series* 241, 012024.

183. C. J. Boehlert. *In situ* scanning electron microscopy for understanding the deformation behaviour of structural materials. Seminarios Internacionales de Fronteras de la Ciencia de Materiales. April 11th, 2011 (http://www.youtube.com/watch?v=wH3EYxT_ysM)

184. J. D. Nowak, K. A. Rzepiejewska-Malyska, R. C. Major, O. L. Warren, J. Michler. *In-situ* nanoindentation in the SEM. Materials today 2009, Electron microscopy special issue, vol. 12, pp. 44-45.

185. M. A. Haque, M. T. A. Saif. *In situ* tensile testing of nano-scale specimens in SEM and TEM. Experimental Mechanics 2002, vol.42, issue 1, pp. 123-128.

186. C.J. Boehlert, C.J. Cowen, S. Tamirisakandala, D.J. McEldowney and D.B. Miracle. *In situ* scanning electron microscopy observations of tensile deformation in a boron-modified Ti–6Al–4V alloy. Scr Mater 2006, vol.55, pp.465-468.

187. T. Gorkaya, T. Burlet, D. A. Molodov, G. Gottstein. Experimental method for true *in situ* measurements of shear-coupled grain boundary migration. Scr Mater 2010, vol. 63, pp. 633–636.

188. P. Poelt, A. Zankel, M. Gahleitner, E. Ingolic, C. Grein. Tensile tests in the environmental scanning electron microscope (ESEM) - Part I: Polypropylene homopolymers. Polymer 2010, vol. 51, pp. 3203-3212.

189. L. P. Canal, C. González, J. Segurado, J. LLorca. Intraply fracture of fiber-reinforced composites: Microscopic mechanisms and modeling. Composites science and technology 2012, vol. 72, issue 11, pp. 1223-1232.

190. M.F. Arif, F. Meraghni, Y. Chemisky, N. Despringre, G. Robert. *In situ* damage mechanisms investigation of PA66/GF30 composite: Effect of relative humidity, Composites Part B: Engineering 2014, vol. 58, pp. 487-495.

191. T. Lin, D. Jia, M. Wang. *In situ* crack growth observation and fracture behavior of short carbon fiber reinforced geopolymer matrix composites. Mater Sci Eng A 2010, vol. 527, pp. 2404–2407.

192. M. Schoßig, A. Zankel, C. Bieröge, P. Pölt, W. Grellmann. ESEM investigations for assessment of damage kinetics of short glass fibre reinforced thermoplastics –Results of *in situ* tensile tests coupled with acoustic emission analysis. Composites Science and Technology2011, vol.71, pp. 257-265.

193. D.J. O'Dwyer, N.P. O'Dowd, C.T. McCarthy. *In situ* SEM mechanical testing of miniature bonded joints. International Journal of Adhesion and Adhesives, 2013.

194. M. Zupan, M. J. Hayden, C. J. Boehlert and K. J. Hemker. Development of High-temperature Microsample Testing. Exp Mech 2001, vol. 41, issue 3, pp. 242–247.

195. M. Frotscher, K. Neuking, R. Böckmann, K. D. Wolff, G. Eggeler. In situ scanning electron microscopic study of structural fatigue of struts, the characteristic elementary building units of medical stents. Mater Sci Eng A, 2008, vol. 481–A482, pp. 160–165.

196. C. Blochwitz, W. Tirschler. *In situ* scanning electron microscope observations of the deformation behaviour of short cracks. Mater Sci Eng A 2000, vol. 276, pp. 273–276.

197. J. H. Han, M. T. A. Saif. *In situ* microtensile stage for electromechanical characterization of nanoscale freestanding films. Rev Sci Instrum 2006, vol. 77, 045102.

198. M.A. Haque, M.T.A. Saif. Application of MEMS force sensors for in situ mechanical characterization of nano-scale thin films in SEM and TEM, Sensors and Actuators-A Physical 2002, vol. 97–98, pp. 239-245.

199. L.P. Canal, C. González, J.M. Molina-Aldareguía, J. Segurado, J. LLorca. Application of digital image correlation at the microscale in fiber-reinforced composites, Composites Part A: Applied Science and Manufacturing 2012, vol. 43, issue 10, pp. 1630-1638.

200. I. de Diego Calderón. Materials Science and Engineering MSc Thesis, Universidad Carlos III de Madrid, June 2013. Deformation behavior of a high strength multiphase steel created via the quenching and partitioning process, at macro- and microscales.

201. C.J. Boehlert, Z. Chen, I. Gutiérrez-Urrutia, J. Llorca, M.T. Pérez-Prado. *In situ* analysis of the tensile and tensile-creep deformation mechanisms in rolled AZ31, Acta Mater 2012, vol. 60, issue 4, pp. 1889-1904.

202. N.V. Dudamell, P. Hidalgo-Manrique, A. Chakkedath, Z. Chen, C.J. Boehlert, F. Gálvez, S. Yi, J. Bohlen, D. Letzig, M.T. Pérez-Prado. Influence of strain rate on the twin and slip activity of a magnesium alloy containing neodymium. Mater Sci Eng A 2013, vol. 583, pp. 220-231.

203. C.J. Boehlert, Z. Chen, A. Chakkedath, I. Gutiérrez-Urrutia, J. Llorca, J. Bohlen, S. Yi, D. Letzig, M.T. Pérez-Prado. *In situ* analysis of the tensile deformation mechanisms in extruded Mg–1Mn–1Nd (wt%). Phil Mag 2013, vol. 93,issue 6, pp. 598-617.

204. C.J. Cowen, C.J. Boehlert. Microstructure, creep, and tensile behaviour of a Ti–15Al–33Nb (at.%) beta+orthorhombic alloy. Phil Mag 2006, vol. 86, issue 1, pp 99-124.

205. C.J. Boehlert, C.J. Chen. The Elevated-Temperature Creep Behavior of Boron-Modified Ti-6Al-4V Alloys. Mater Trans 2009, vol. 50, n. 7, pp. 1690-1703.

206. C.J. Boehlert, S. Tamirisakandala, W.A. Curtin, D.B. Miracle, Assessment of in situ TiB whisker tensile strength and optimization of TiB-reinforced titanium alloy design. Scr Mater 2009, vol.61, issue 3, pp. 245-248.

207. C.J. Cowen and C.J. Boehlert. The Microstructure, Creep, and Tensile Behavior for Ti-5Al-45Nb (Atomic Percent) Fully-β Alloy. Metall Mater Trans A 2007, vol.38, pp.26-34.

208. C. J. Boehlert, S.C. Loganbach, T.R. Bieler. The effect of thermomechanical processing on the creep behavior of Udimet Alloy 188. Phil Mag 2008, vol. 88, pp. 641.

209. S. Kahl, R. L. Peng, M. Calmunger, B. Olsson, S. Johansson. *In situ* EBSD during tensile test of aluminum AA3003 sheet. Micron 2013, ISSN 0968-4328.

210. P. Chen, S.C. Mao, Y. Liu, F. Wang, Y.F. Zhang, Z. Zhang, X.D. Han. *In situ* EBSD study of the active slip systems and lattice rotation behavior of surface grains in aluminum alloy during tensile deformation. Mater Sci Eng A 2013, vol. 580, pp. 114-124.

211. Y. Zhang, H. J. Shi, J. Gu, C. Li, K. Kadau, O. Luesebrink. Crystallographic analysis for fatigue small crack growth behaviors of a nickel-based single crystal by *in situ* SEM observation. Theoretical and Applied Fracture Mechanics 2013,

212. C.J. Szczepanski, S.K. Jha, P.A. Shade, R. Wheeler, J.M. Larsen, Demonstration of an *in situ* microscale fatigue testing technique on a titanium alloy. International Journal of Fatigue 2013, vol. 57, pp. 131-139.

213. W. Chen, C. J. Boehlert. The 455 °C tensile and fatigue behavior of boron-modified Ti–6Al–2Sn–4Zr–2Mo–0.1Si(wt.%). International Journal of Fatigue 2010, vol. 32, n. 5, pp. 799-807.

214. H. Li, D.E. Mason, T.R. Bieler, C.J. Boehlert, M.A. Crimp. Methodology for estimating the critical resolved shear stress ratios of α-phase Ti using EBSD-based trace analysis. Acta Mater 2013, vol. 61, issue 20, pp. 7555-7567.

215. P. Chen, S. C. Mao, Y. Liu, F. Wang, Y. F. Zhang, Z. Zhang, X. D. Han. In-situ EBSD study of the active slip systems and lattice rotation behavior of surface grains in aluminum alloy during tensile deformation. Mater Sci Eng A 2013, vol. 580, pp. 114-124.

216. Q. K. Zhang, Z. F. Zhang. In situ tensile creep behaviors of Sn–4Ag/Cu solder joints revealed by electron backscatter diffraction. Scr Mater 2012, vol. 67, pp. 289-292.

217. M. Ojima, Y. Adachi, S. Suzuki, Y. Tomota. Stress partitioning behavior in an fcc alloy evaluated by the in situ/ex situ EBSD-Wilkinson method. Acta Mater 2011, vol. 59, pp. 4177-4185.

218. L. Wang, Y. Yang, P. Eisenlohr, T. R. Bieler, M. A. Crimp, D. E. Mason. Twin Nucleation by Slip Transfer across Grain Boundaries in Commercial Purity Titaniu. Metall Mater Trans A 2010, vol. 41, pp. 421-430.

219. W. Chen, C. J. Boehlert. Effect of Boron on the Elevated-Temperature Tensile and Creep Behavior of Cast Ti6Al2Sn4Zr2Mo0.1Si. Metall Mater Trans A 2009, vol. 40, pp. 1568.

220. W. Zhang, Y. Liu. *In situ* SEM testing for crack closure investigation and virtual crack annealing model development. International Journal of Fatigue 2012, vol. 43, pp. 188-196.

221. W. Zhang, Y. Liu. Investigation of incremental fatigue crack growth mechanisms using *in situ* SEM testing. International Journal of Fatigue 2012, vol. 42, pp. 14-23.

222. H. Andersson, C. Persson. *In situ* SEM study of fatigue crack growth behavior in IN718. International Journal of Fatigue 2004, vol. 26, n. 3, pp. 211–219.

223. M.D. Halliday, P. Poole, P. Bowen. *In situ* SEM measurements of crack closure for small fatigue cracks in aluminum 2024-T351. Fatigue Fract Eng Mater Struct 1995, vol. 18, n. 6, pp. 717–729.

224. X. Ma, H. J. Shi. *In situ* SEM studies of the low cycle fatigue behavior of DZ4 superalloy at elevated temperature: Effect of partial recrystallization. International Journal of Fatigue 2013.

225. H.-W. Song, Q.-J. He, J.-J. Xie, A. Tobota. Fracture mechanisms and size effects of brittle metallic foams: *In situ* compression tests inside SEM. Composites Science and Technology 2008, vol. 68, issue 12, pp. 2441-2450.

226. P.Q. Dai, Z.R. He, C.M. Zheng, Z.Y. Mao. *In situ* SEM observation on the fracture of austempered ductile iron. Mater Sci Eng A 2001, vol. 319–321, pp. 531-534.

227. Y.-F. Chen, S.-Q. Zheng, J.-P. Tu, S.-L. Xiao, J. Tian, L.-J. Xu, Y.-Y. Chen. Fracture characteristics of notched investment cast TiAl alloy through *in situ* SEM observation. Transactions of Nonferrous Metals Society of China 2012, vol. 22, issue 10, pp. 2389-2394.

228. X. Ma, H.-J. Shi. *In situ* SEM studies of the low cycle fatigue behavior of DZ4 superalloy at elevated temperature: Effect of partial recrystallization. International Journal of Fatigue 2013, vol. 61, pp. 255-263.

229. Y. Zhang, H.-J. Shi, J. Gu, C. Li, K. Kadau, O. Luesebrink. Crystallographic analysis for fatigue small crack growth behaviors of a nickel-based single crystal by *in situ* SEM observation. Theoretical and Applied Fracture Mechanics 2013, vol- 67-68, pp. 29-37.

230. E. A. Torres, F. E. Montoro, A. J. Ramirez. *In situ* high temperature deformation experiments at the SEM. LNLS Activity report 2009.

231. SBIR/STTR, USA Government website. High temperature microsample testing system. https://www.sbir.gov/sbirsearch/detail/409921

232. J. Cheng, W. Jianguo, C. Wenjue. Scr Metall Mater 1995, vol. 32, issue 10, pp. 1579-1584.

233. Y.H. Lu, Y.G. Zhang, L.J. Qiao, Y.B. Wang, C.Q. Chen, W.Y. Chu. The fracture mechanism of a fully lamellar γ-TiAl alloy through *in situ* SEM observation. Intermetallics 2000, vol. 8, issue 12, pp. 1443-1445.

234. R. Cao, H.J. Yao, J.H. Chen, J. Zhang. On the mechanism of crack propagation resistance of fully lamellar TiAl alloy. Mater Sci Eng A 2006, vol. 420, issues 1–2, pp. 122-134.

235. Z.P. Sun, R. T. Zheng, Y. G. Zhang, C. Q. Chen. Effect of microstructure on fracture behavior in fully lamellar gamma TiAl alloy. Rare metals materials and engineering 2004, vol.33, pp. 196-200.

236. R. T. Zheng, G. A. Cheng, X. J. Li, G. X. CAO, L. F. Fu, Y. G. Zhang, C. Q. Chen. The relationship between fracture toughness and microstructure of fully lamellar TiAl alloy. J Mater Sci 2007, vol. 42, pp. 1251–1260.

237. M. Rester, F.D. Fischer, C. Kirchlechner, T. Schmoelzer, H. Clemens, G. Dehm, Deformation mechanisms in micron-sized PST TiAl compression samples. Experiment and model. Acta Mater 2011, vol. 59, issue 9, pp. 3410-3421.

238. N. Biery, M. Graef, T. M. Pollok. A Method for Measuring Microstructural-Scale Strains Using a Scanning Electron Microscope: Applications to -Titanium Aluminides. Metall Mater Trans A 2002, vol. 34, pp. 2003-2301.

239. M. Zhang, X. P. Song, L. Yu, H. L. Li, Z. H. Jiao, H. C. Yu. Fatigue small crack growth threshold determination of a high-Nb TiAl alloy at different temperatures by in situ observation. International journal of minerals metallurgy and materials 2013, vol. 20, pp. 1192-1197.

240. D. B. Williams, C. B. Carter. Transmission Electron Microscopy. Plenum Press, 1996.

241. Q. K. Zhang, Z. F. Zhang. *In situ* tensile creep behaviors of Sn–4Ag/Cu solder joints revealed by electron backscatter diffraction. Scr Mater 2012, vol. 67, pp. 289-292.

242. M. Ojima, Y. Adachi, S. Suzuki, Y. Tomota. Stress partitioning behavior in an fcc alloy evaluated by the *in situ/ex situ* EBSD-Wilkinson method. Acta mater 2011, vol. 59, pp. 4177-4185.

243. Standard Test Methods for Determining Average Grain Size, ASTM Designation E112-96e3, ASTM, West Conshohocken, PA, 1996.

244. H. Li, D. E. Mason, Y. Yang, T. R. Bieler, M. A. Crimp, C. J. Boehlert. Analysis of slip activity and heterogeneous deformation in tensionand tension-creep of Ti–5Al–2.5Sn (wt. %) using *in situ* SEM experiments. Phil Mag 2013, vol. 93, pp. 2875-2946.

245. C. J. Boehlert, H. Li, L. Wang , B. Bartha. Slip System Characterization of Inconel 718 using *in situ* Scanning Electron Microscopy. Adv Mater Process 2010, vol.168, pp. 41-45.

246. L. Wang, Y. Yang, P. Eisenlohr, T. R. Bieler, M. A. Crimp, D. E. Mason. Twin Nucleation by Slip Transfer across Grain Boundaries in Commercial Purity Titanium. Metall Mater Trans A 2010, vol. 41:421-430.

247. T. Mishin, C. Herzig. Diffusion in the Ti–Al system. Acta Mater 2000, vol. 48, pp. 589-623.

248. D.Y. Seo, L. Zhao, J. Beddoes. Microstructural evolution during heat treatments in Ti-45Al and 47Al-2Nb-2Mn+0.8vol.%TiB_2 XD^{TM} alloys. Mater Sci Eng A 2002, vol. 329-331, pp. 130-140.

249. Y. Chen, H. Niu, F. Kong, S. Xiao. Microstructure and fracture toughness of a β phase containing TiAl alloy. Intermetallics 2011, vol. 19, pp. 1405-1410.

250. H. Clemens, A. Bartels, S. Bystrzanowsky, H. Chladil, H. Leitner, G. Dehm, R. Gerling, F. P. Shimansky. Grain refinement in g-TiAl-based alloys by solid state phase transformations. Intermetallics 2006, vol. 14, pp. 1380-1385.

251. W. Voice, M. Henderson, E. F. J. Shelton, X. Wu. Gamma titanium aluminide, TNB. Intermetallics 2005, vol. 13 pp. 959-964.

252. T. Novoselova, S. Malinov, W. Sha. Experimetnal study of the effects of heat treatment on microstructure and grain size of a gamma TiAl alloy. Intermetallics 2003, vol. 11, pp. 491-499.

253. G. Cao, L. Fu, J. Lin, Y. Zhang, C. Chen. The relationships of microstructure and properties of a fully lamellar TiAl alloy. Intermetallics 2000, vol. 8, pp. 647-653.

254. F. Diologent, T. Krumi. Measurement of the effective activation volume in 45XD titanium aluminides by repeated transient tests. Mat Sci Eng A 2008, vol. 487, pp. 377-382.

255. C. Yang, D. Hu, A. Huang, M. Dixon. Microstructures and tensile properties of hot isostatic pressed Ti4522XD powders. Mater Sci Eng A 2012, vol. 534, pp. 268– 276.

256. F. Appel. Mechanistic understanding of creep in gamma-base titanium aluminide alloys. Intermetallics 2001, vol. 9, pp. 907–14.

257. R.A. Mirshams, Z.X. Li, and H.P. Mohamadian. J Mater Sci Lett 1997, vol. 16, pp. 715–18.

258. T.G. Langdon. Grain boundary sliding as a deformation mechanism during creep. Phil Mag 1970, vol. 22, pp. 689–700.

259. D.Y. Seo, H. Saari, J. Beddoes, and L. Zhao: in International Conference on Structural Intermetallics, K.J. Hemker, D.M. Dimiduk, H. Clemens, R. Darolia, H. Inui, J.M. Larsen, V.K. Sikka, M. Thomas, and J.D. Whittenberger, eds., The Minerals, Metals and Materials Society, PA, Warrendale, 2001, pp. 653–62.

260. M. Es-Souni, A. Bartels, R. Wagner. Creep behaviour of near γ-TiAl base alloys: Effects of microstructure and alloy composition. Mater Sci Eng A 1995, vols. 192–193, pp. 698–706.

261. W.J. Zhang, S.C. Deevi. International Conference on Structural Intermetallics (eds. K.J. Hemker, D.M. Dimiduk, H. Clemens, R. Darolia, H. Inui, J.M. Larsen, V.K. Sikka, M. Thomas, and J.D. Whittenberger). The Minerals, Metals and Materials Society, PA, Warrendale.

262. D. B. Worth, J.W. Jones, J.E. Allison. Metall Mater Trans A 1995, vol. 26A, pp. 2947–59.

263. L.M. Hsiung, T.G. Nieh. Creep deformation of fully lamellar TiAl controlled by the viscous glide of interfacial dislocations. Intermetallics 1999, vol. 7, pp. 821–27.

264. J.N. Wang and T.G. Nieh. The role of ledges in creep of TiAl alloys with fine lamellar structures. Acta Mater 1998, vol. 46, pp. 1887– 1901.

265. J. B. Singh, G. Molénat, M. Sundararaman, S. Banerjee, G. Saada, P. Veyssière, A. Couret. *In situ* straining investigation of slip transfer across α_2 lamellae at room temperature in a lamellar TiAl alloy. Phil. Mag 2006, vol.86, pp. 2429-2450.

266. R. Muñoz-Moreno,C. J. Boehlert, M. T. Pérez-Prado, E. M. Ruiz-Navas, J. Llorca. *In situ* observations of the deformation behavior and fracture mechanisms of Ti-45Al-2Nb-2Mn+0.8v%TiB_2 . Met Mat Trans A 2012, vol. 43, pp. 1198-1208.

267. R. Muñoz-Moreno, M. T. Pérez-Prado, J. Llorca, E. M. Ruiz-Navas, C. J. Boehlert. Effect of stress level on the high temperature deformation and fracture mechanisms of Ti-45Al-2Nb-2Mn-0.8v.%TiB_2: an *in situ* experimental study. Met Mat Trans A 2013, vol. 44, pp. 1887-1896.

268. H. Inui, M. Matsumuro, D. H. Wu, M. Yamaguchi. Temperature dependence of yield stress, deformation mode and deformation structure in single crystals of TiAl (Ti−56 at.% Al). Phil Mag A 1997, vol. 75, pp. 395-423.

269. C. Woodward, S. I. Rao. *Ab-initio* simulation of (a/2) $\langle 110]$ screw dislocations in γ-TiAl. Phil Mag 2004, vol. 84, pp. 401-413.

270. T. G. Nieh, M. Wadsworth, O. D. Sherby. Superplasticity in metals and ceramics. Cambridge University Press, Cambridge, UK, 1997.

271. M. F. Ashby, M. A. Verral. Diffusion accommodated flow and superplasticity. Acta Metal 1973, vol. 21, pp. 149-163.

272. J. R. Spingarn, W. D. Nix. Diffusional creep and diffusionally accommodated grain rearrangement. Acta Metal 1978, vol. 26, pp. 1389-1398.

273. O. D. Sherby, J. Wadsworth. Superplasticity-Recent advances and future directions. Prog Mater Sci 1989, vol. 33, pp. 169-221.

274. A. Ball, M. M. Hutchison. Superplasticity in the aluminum-zinc eutectoid. Met Sci J 1969, vol. 3, pp. 1-6.

275. K. Sotoudeh, P. S. Bate. Diffusion creep and superplasticity in aluminium alloys. Acta Mater 2010, vol. 58, pp. 1909-1920.

276. M. A. Rust, R. I. Todd. Surface studies of Region II superplasticity of AA5083 in shear: Confirmation of diffusion creep, grain neighbour switching and absence of dislocation activity. Acta Mater 2011, vol. 59, pp. 5159-5170.

277. H. Watanabe, K. Kurimoto, T. Uesugi, Y. Takigawa, K. Higashi. Accommodation mechanisms for grain boundary sliding as inferred from texture evolution during superplastic deformation. Phil Mag 2013, vol. 93, pp. 2913-2931.

278. M.T. Pérez-Prado, G. González-Doncel, O.A. Ruano, T.R. McNelley. Texture analysis of the transition from slip to grain boundary sliding in a discontinuously recrystallized superplastic aluminum alloy. Acta Mater 2001, vol. 49, issue 12, pp. 2259-2268.

Publications

Scientific articles published in peer-reviewed journals

- R. Muñoz-Moreno, E. M. Ruiz-Navas, C. J. Boehlert, J. Llorca, J. M. Torralba, M. T. Pérez-Prado: *Analysis of crystallographic slip and grain boundary sliding in a Ti-45Al-2Nb-2Mn(at.%)-0.8v.%TiB_2 alloy by high temperature in situ mechanical testing*. **Materials Science and Engineering A** 2014. http://dx.doi.org/10.1016/j.msea.2014.03.078.

- R. Muñoz-Moreno, E. M. Ruiz-Navas, B. Srinivasarao, J. M. Torralba: *Microstructural development and mechanical properties of PM Ti-45Al-2Nb-2Mn-0.8vol.%TiB_2 processed by Field Assisted Hot Pressing.* **Journal of Materials Science and Technology** 2014, *submitted.*

- R. Muñoz-Moreno, M. T. Pérez-Prado, J. Llorca, E. M. Ruiz-Navas, C. J. Boehlert: *Effect of stress level on the high temperature deformation and fracture mechanisms of Ti-45Al-2Nb-2Mn-0.8vol%TiB_2: an in situ experimental study.* **Metallurgical and Materials Transactions A** 2013; 44: 1887-1896. DOI: 10.1007/s11661-012-1515-8

- B. Srinivasarao, A. P. Zhilyaev, R. Muñoz-Moreno, M. T. Pérez-Prado: *Effect of high pressure torsion on the microstructure evolution of a gamma Ti-45Al-2Nb-2Mn-0.8vol%TiB_2 alloy.* **Journal of Materials Science** 2013; 48: 4599-4605. DOI: 10.1007/s10853-013-7201-4

- R. Muñoz-Moreno, C. J. Boehlert, M. T. Pérez-Prado, E. M. Ruiz-Navas, J. LLorca: *In situ observations of the deformation behavior and fracture mechanisms of Ti-45Al-2Nb-2Mn+0.8 vol%TiB_2.* **Metallurgical and Materials Transactions A** 2012; 43: 1198-1208. DOI:10.1007/s11661-011-1022-3

Conference contributions

- R. Muñoz-Moreno, E. M. Ruiz-Navas, M. T. Pérez-Prado, C. J. Boehlert, J. M. Torralba. *Microstructural development of a HIP'ed γ-TiAl intermetallic alloy and in situ analysis of the deformation mechanisms*. **Intermetallics 2013. Bad Staffelstein, Germany, Oct. 2013. Oral**.

- R. Muñoz-Moreno, E. M. Ruiz-Navas, J. M. Torralba, J. Llorca, C. J. Boehlert, M. T. Pérez-Prado. *High temperature deformation mechanisms in Ti4522XD microstructures: An in situ EBSD experimental study*. Intermetallics 2013. Bad Staffelstein, Germany, Oct. 2013. Oral.

- R. Muñoz-Moreno, E. M. Ruiz-Navas, M. T. Pérez-Prado, C. J. Boehlert, J. M. Torralba. *Microstructural development of a HIP'ed γ-TiAl intermetallic alloy and in situ analysis of the deformation mechanisms.* EuroPM - Special seminar of interest on new and innovative applications of PM HIP. **Euro PM2013 congress and exhibition. Gothenburg, Sweden, Sept. 2013. Proceeding-Oral.**

- R. Muñoz-Moreno, E. M. Ruiz-Navas, C. J. Boehlert, M. T. Pérez-Prado. *In situ EBSD analysis of the high temperature deformation and fracture mechanisms of a γ-TiAl intermetallic alloy.* **Euromat 2013. Seville, Spain, Sept. 2013. Oral.**

- R. Muñoz-Moreno, E. M. Ruiz-Navas, M. T. Pérez-Prado, J. M. Torralba. *Modification of a powder metallurgy γ TiAl alloy microstructure by heat treatments*. **Euromat 2013. Seville, Spain, Sept. 2013. Oral-Poster.**

- R. Muñoz-Moreno, M.T. Pérez-Prado, J. Llorca, E.M. Ruiz-Navas, C.J. Boehlert. *Effect of the stress level on the high temperature deformation and fracture mechanisms of a γ-TiAl intermetallic alloy*. **Engineering Graduate Research Symposium. Michigan State University, U.S., Nov. 2012. Poster**.

- R. Muñoz-Moreno, M. T. Pérez-Prado, E. M. Ruiz-Navas, C. J. Boehlert, J. Llorca. *In situ SEM observations of the tensile-Creep deformation behaviour and fracture mechanisms of a γ-TiAl intermetallic alloy at low and high stresses.* **MRS Fall Meeting. Boston, U.S., Nov. 2012. Proceeding-Oral**.

- R. Muñoz-Moreno, B. Srinivasarao, I. Sabirov, E. M. Ruiz-Navas, J. M. Torralba. *Analysis of the temperature effect on the lamellar microstructure transformation of γ-TiAl intermetallics processed by field assisted hot pressing*. EuroPM - non ferrous. Proceedings edited by Prof. T. Ebel. **Euro PM2012 congress and exhibition. Basel, Switzerland, Sept. 2012. Proceeding-Oral**.

- R. Muñoz-Moreno, B. Srinivasarao, I. Sabirov, E. M. Ruiz-Navas, J. M. Torralba. *Microstructural development of γ-TiAl intermetallics processed by field assisted hot pressing*. **IV Powder Metallurgy National Conference. Seville, Spain, Jun. 2012. Oral**.

- R. Muñoz-Moreno, E. M. Ruiz-Navas, J. LLorca, M. T. Pérez-Prado, C. J. Boehlert. *An in-situ SEM evaluation of the elevated-temperature tensile and creep deformation behavior of Ti-45Al-2Mn-2Nb-XD*. **4th International Workshop on Titanium Aluminides. Nuremberg. Germany, Sept. 2011**.**Oral**.

- R. Muñoz-Moreno, E. M. Ruiz-Navas, M. T. Pérez-Prado, C. Boehlert. *An in-situ SEM evaluation of the creep deformation behavior of a γ-TiAl alloy*. **6th Aerodays conference. Madrid, Spain, Mar. 2011**. **Oral-Poster (2nd Prize)**.